

POLITECNICO DI TORINO

DIPARTIMENTO DI INGEGNERIA STRUTTURALE, EDILE E GEOTECNICA

Corso di Laurea Magistrale in Ingegneria Civile



Tesi di Laurea Magistrale

**SEISMIC PERFORMANCE OF
DETERIORATING CONCRETE BRIDGES**

Relatore:

Prof. Marco Domaneschi

Correlatore:

Prof. Joan Ramon Casas

Candidato:

Antonino De Gaetano

Dicembre 2019

*A mio nonno,
maestro di vita e di saggezza.*

*Nonno mi hai lasciato dentro ad un mondo a pile
Centri commerciali al posto del cortile
Una generazione con nuovi discorsi
Si parla più l'inglese che i dialetti nostri.
(Enrico Nigiotti, "Nonno Hollywood")*

Contents

1	Introduction	1
2	Deteriorating existing bridges and viaducts	5
2.1	Bridges	5
2.2	Viaducts	8
2.3	Deteriorating bridges and viaducts	8
2.4	Support devices	12
2.5	Neoprene bridge bearings	12
2.6	Seismic activity on bridges	13
2.7	Seismic hazard of the Messina area	14
3	Deterioration models	17
3.1	Corrosion	17
3.2	Marine chloride-induced corrosion	21
3.3	Bonding	22
3.4	Validity of corrosion models	25
3.4.1	Corrosion rate model	27
3.4.2	General corrosion model	32
3.4.3	Pitting corrosion model	33
4	Bridge case study	37
4.1	Typology	37
4.2	Longitudinal profile	39
4.2.1	Convex profile	39
4.2.2	Variable depth definition	39
4.3	Cross-section	40
4.4	Edge details	41
4.5	Abutments	42
4.6	Pier	42
4.6.1	Geometry	42
4.6.2	Preliminary design	43

4.7	Bridge modelling on SAP2000	46
4.8	Loads definition	50
4.9	Seismic analysis	51
4.9.1	Earthquake application in the software	57
4.9.2	Loads combination	58
4.10	SAP2000 outcomes	59
4.10.1	Applied actions	61
4.11	Modal analysis	64
4.12	Computation of the longitudinal steel reinforcement area	73
4.13	Computation of the transverse steel reinforcement area	78
4.13.1	General requirements of the concrete pier confinement in Section A	79
4.13.2	Resisting shear and failure assessment	80
4.13.3	General requirements of the concrete pier confinement in Section B	81
4.13.4	Resisting shear and failure assessment	82
4.13.5	Computation of reinforcements to prevent instability of compressed vertical bars	83
4.14	Support devices	85
4.14.1	Neoprene bridge bearings	85
4.14.2	Design of the support devices	86
5	Application of the corrosion model to the case study	89
5.1	Deterioration input parameters	89
5.2	Corrosion rate model	91
5.3	General corrosion analysis	92
5.4	Pitting corrosion analysis	93
5.5	Combination of general and pitting corrosion analysis	96
5.6	Yield strength analysis	97
6	Interaction domains and ductility performance	101
6.1	Ductility performance	101
6.2	Interaction domain	103
6.3	Combination of general and pitting corrosion analysis	116
6.4	Bresler's domain	120
6.5	Limitations of the presented approach	127
7	Retrofitting	129
7.1	Overview of seismic retrofit approaches	130
7.2	Retrofit of concrete columns	132
7.3	Cost analysis overview	135
	Conclusions	139

A Matlab script	141
Acknowledgements	149
Bibliography	159

Abstract

This study examines the effect of corrosion on reinforced concrete structural elements of a bridge overpass in seismic affected areas. Starting from a literature review to identify the existing deteriorating models, a case study is selected to perform seismic analyses. It allows assessing the structural response at different levels of reinforced concrete degradation due to corrosion.

The selected case study is a frequently used structural system with several existing examples in critical infrastructures all around the world. Consequently, an in-depth analysis of the degradation of this type of system, with the identification of the most appropriate time for restoration and the possible retrofitting strategies may be of interest.

The bridge is assumed to be located in Sicily, the largest island in Southern Italy. In particular, a site close to the Strait of Messina has been selected with a high seismic hazard. Accordingly, with the current Italian standard for constructions, it belongs to the first seismic category among four. Indeed, a strong earthquake destroyed all the city in 1908.

A finite element model of the bridge overpass is prepared to perform the seismic analyses. Different levels of degradation have been simulated by using a deterministic approach. They include reduction of the steel reinforcement areas and the steel strength losses due to corrosion. The position of the bridge concerning the sea is also considered because it can also affect the steel reinforcement degradation due to pitting corrosion.

Finally, retrofitting strategies to improve the seismic performance of the bridge are evaluated to preserve it from demolishing and rebuilding.

Chapter 1

Introduction

Nowadays, seismic performance of deteriorating RC bridges is a matter of increasing concern. There is no possibility of changing nature, and that is a fact. People have to adapt themselves to it, respecting it, loving it and adapting themselves to their needs. It is not possible to control or eliminate earthquakes, which have always been and will always be there, and then it is necessary to learn to live with them. The first step in this direction is to build in an intelligent way, starting from the infrastructure. The development of new public works determines and improves the well-being of a society.

Moreover, Italy is one of the European countries where the seismic hazard is highest. This is evident in many earthquakes that over the years have destroyed cities, villages with their structures, infrastructures and more. Preventing an earthquake means knowing it well, i.e. how it behaves, develops and affects structures. The challenge is more interesting when the structures are bridges, as in this study. During an earthquake, bridges should not collapse because they ensure the link between two points of the city and this should allow the passageway of emergency vehicles to rescue human lives.

The 1908 Messina earthquake can be mentioned as an example of a strong Italian earthquake. It happened on 28 December in Sicily and Calabria (Southern Italy), with a moment magnitude of 7.1 and a maximum Mercalli intensity of XI (Extreme). The cities of Messina and Reggio Calabria were almost completely destroyed and between 75,000 and 82,000 lives were lost. This kind of event shows that earthquake analysis becomes essential in the new structures design.

Moreover, the position near the sea must be considered, because oxygen, moisture and chloride ions affect the durability of the bridge. Corrosion can occur in two forms: general

and pitting. Both are harmful to the structural performance of the RC pier of the bridge. For this reason, a number of methods are mentioned in the present thesis to prevent corrosion of the steel reinforcement.

The topic of this thesis is a new bridge, located in the area of Messina and designed to deal with seismic action. The study analyses the performance of the bridge that decreases over the years due to the effects of corrosion. This aspect is of interest because most existing bridges in Southern Italy are in a deteriorating state. This appears very clearly in the spalling on the concrete cover. Thus, there is major and increasing demand for reliable methods to assess the capacity and remaining service life of existing infrastructure. For this reason, designing a bridge by taking into account corrosion and performance losses is fundamental to prevent abrupt collapse and the lower durability. So, this thesis aims to contribute to the improvement of bridge engineering. Sometimes, the structure must be demolished because the service life of the bridge ends. By contrast, a retrofitting strategy may be applied in situations in which the structure can survive from a structural and economic point of view. For this reason, this investigation also deals with this issue by suggesting new further developments for the maintenance of the structures in the future. The thesis is structured as follows:

Chapter 2 provides a brief overview of bridges and viaducts, in particular the effect of seismic action on this kind of structures. The typology and function of the support devices are also briefly reviewed. Additionally, the existing heritage, ageing and reduction of bridge performance are also discussed.

Chapter 3 regards the deterioration models, starting from a literature review. Furthermore, it focuses on the most accurate existing model (Cui et al.) that is applied to the bridge case study in this thesis. An applied model validation and the comparison graphs complete the chapter.

Chapter 4 presents the bridge case study, and the design of the geometry of the structure. Static linear and modal analyses are described. In addition, computations regarding all the checks of the support devices are shown according to the European standard.

The application of the corrosion model to the case study is discussed in Chapter 5. The input parameters change with respect to Chapter 3, because here the structure is different. The decrease of the steel reinforcement area and the steel yielding strength due to the corrosion effects is shown as well.

Chapter 6 presents how the findings obtained in the previous section determine the struc-

tural capacity of the bridge. Especially, it analyses how long the service life of the bridge lasts using interaction and Bresler's domains. Additionally, the reduction of the ductility performance is considered and computed, as an important requirement of the structure. Finally, retrofitting strategies to improve the seismic performance of the bridge are discussed in Chapter 7, and Conclusions and suggestions for future developments are made in Chapter 8.

Chapter 2

Deteriorating existing bridges and viaducts

2.1 Bridges

A bridge is a structure built to span a physical obstacle, represented by a water stream, a valley or a road, without closing the way underneath. It is a great solution which plays an important role in economy, politics, culture, as well as national defence.

Since Neolithic, this kind of structure has been used, the earliest and simplest typology being a stepping stone, as shown in Figure 2.1.



Figure 2.1: Stepping stone bridge

One of the earliest types of a spanning structure is the timber bridge, such as the **Holzbrücke Rapperswil-Hurden**, discovered in the west of the Seedamm, dating back to 1523 BC. Successively, during the ancient Roman Age, a lot of arch bridges were built. This is evident in the case of the **Alcantara Bridge**, built over the river Tagus, in Spain (Figure 2.2).



Figure 2.2: Roman Alcantara Bridge

Subsequently, after the Industrial Revolution in the 19th century, truss systems of wrought iron were developed for larger bridges. As shown in Figure 2.3, the evidence of iron bridges can be clearly seen in the case of **Dom Luís I Bridge**, designed in 1886 by Theophile Seyrig, a disciple of Gustave Eiffel. It is a double-deck metal arch bridge that spans the River Douro between the cities of Porto and Vila Nova de Gaia in Portugal. During its construction, the 172 metres span was the longest of its type in the world.

On the other hand, iron does not have the tensile strength to support large loads. So, using the ideas of Gustave Eiffel, many larger bridges were built with the advent of steel, which has a high tensile strength.

Century after century, bridge engineering developed and new solutions and types were found, which allowed longer and longer spans. A remarkable example is the cable-stayed bridge, that is held up by cables. The **Rusky Bridge** in Russia is the longest cable-stayed bridge; it was built in 2012 and highlights the longest span of 1,104 m (Figure 2.4).

Currently, the longest span has been achieved only in the case of the suspension bridge. It represents the most innovative and brilliant solution regarding bridge engineering. The main advantages are the possibility to withstand earthquake movements and the use of a reduced quantity of material, which leads to a reduced construction cost if compared to



Figure 2.3: Dom Luis I Bridge, Portugal



Figure 2.4: Russky Bridge, Russia

other bridges. **Akashi Kaikyō Bridge** in Japan is the longest suspension bridge in the world (3,909 meters) boasting the longest span record of 1,991 m. Figure 2.5 presents its impressive features.



Figure 2.5: Akashi Kaikyō Bridge, Japan

2.2 Viaducts

A viaduct is a characteristic type of bridge, composed of several small spans in order to cross a valley, dry or wetland or to form an overpass. Viaducts are commonly used in many cities that are railroad centres, such as Chicago, Atlanta, Birmingham and London. Basically, these structures carry railroads over large valleys or over cities with many cross-streets and avenues.

Most times, viaducts are made in order to have a motorway that overcomes obstacles, such as rivers, valleys, woods, urban centres. A great example is the **Millau Viaduct**, a cable-stayed road-bridge that spans the valley of the river Tarn near Millau in Southern France. It is the tallest bridge in the world with a pier summit at 343 metres, as shown in Figure 2.6.

2.3 Deteriorating bridges and viaducts

During the 70s and 80s, most Italian bridges and viaducts were built, as a consequence of the new structural and infrastructural development. For this reason, people mobility has been improved by motorways network and bridge engineering has found many applications. Currently, the heritage of existing bridges can be seen in the whole Country, even in



Figure 2.6: Millau Viaduct, France

Southern Italy. A consequence of that is the necessity to protect structures from aging and corrosion. Deteriorating viaducts are a phenomenon that must be solved, owing to a high damage hazard. Therefore, a design preventing corrosion and bonding failure is required. Sicily is mainly a hilly region, but also mountainous for a quarter of its extension. This determines the demand of connection infrastructures, such as bridges, viaducts and tunnels. Thereby, most part of the infrastructures were built in the 1970s and so, they have already achieved almost half a century of service period.

The main arteries of Sicily are the highways A20 Messina-Palermo, A19 Catania-Palermo, A18 Messina-Catania. Moreover, they are located near the sea for the majority of their route, thus this can be an issue that affects these structures due to marine chloride-induced corrosion effects.

The 1970s viaducts were mainly made of prestressed reinforced concrete. Consequently, degradation phenomena due to chemical and physical causes have limited the structures strength and stability.

This is certainly true in the case of chlorides, sulphides, sulphates and carbon dioxide. This gas in the air causes concrete carbonation and depassivation of the reinforcement bars what may originate a corrosion process. In particular, corrosion occurs due to the decrease of the environment basicity in which the bars are embedded.

Additionally, the effect is dangerous also in the case of prestressed reinforcements. Here, the stress rates applied on them are higher, due to stress corrosion. So, a serious monitoring and seismic upgrading is required to preserve the Sicilian infrastructural heritage.

The **Morandi Viaduct** in Agrigento illustrates this point clearly. It was designed in 1970 and closed in 2015 due to structural damage in the pillars and for further maintenance and

safety work. Figure 2.7 shows as corrosion is located in the columns.



Figure 2.7: Pillar detail of the Morandi Viaduct, Sicily

This case study confirms the importance of preserving structures and preventing them from corrosion.

An example of this is the work carried out by an Italian company for the **Ritiro Viaduct** located in Messina. Here, the seismic prevention has been considered as well. Figure 2.8 illustrates a top view photo of this Sicilian infrastructure.



Figure 2.8: Top view photo of the Ritiro Viaduct, Messina

During these years, a retrofitting strategy is going on aimed to the maintenance of the structure. The viaduct work is expected to be completed in 2020. The strategy wants to

improve the structural and infrastructural aspects, especially the seismic ones. Figure 2.9 presents the Ritiro Viaduct intersection above the city of Messina.



Figure 2.9: Ritiro Viaduct intersection, Messina

Therefore, the deck has been demolished and, by contrast, the piers have been left. The first operation has been to increase the structural stability of the spread footings of the pillars with metallic micropiles inside the ground. In addition, the steel reinforcement of the spread footing has been increased. Regarding the abutments, the most relevant intervention has been performed in the Palermo side. Indeed, a group of cables in the retaining wall have been located and a steel reinforcement has been added in the wall. The most interesting aspect is related to the pillars of the bridge. Indeed, these elements receive the vertical and horizontal (static and dynamic) loads of the total structure. The piers have been reinforced with additional steel reinforcement around. Consequently, a steel formwork filled with concrete cast in situ has been placed above the columns in order to satisfy seismic requirements. At the top of the formwork, a couple of seismic isolators has been installed to ensure a higher stability and smaller maintenance. Specifically, they are elastomeric bearing pads and have been designed to withstand high vertical loads and allow large horizontal displacements. By contrast, the new deck has been replaced by a steel one, in order to have a mixed structure. Above, a concrete slab has been casted in situ and finally, the bitumen pavement has been placed.

2.4 Support devices

Support devices are fundamental components in the bridge, thereby having the purpose to withstand vertical loads and allow horizontal imposed displacements. In particular, displacements are due to linear and imposed deformations, represented by prestressing force, temperature, creep and shrinkage. Moreover, they depend on wind, braking force and especially seismic activity as well.

A bridge bearing is a component of a bridge which typically provides a resting surface between the piers and the deck of a bridge. There are several different types of bridge bearings which are used depending on a number of different factors including the bridge span. A common form of modern bridge bearing is the elastomeric bearing pad, made of reinforced neoprene. They are designed and manufactured based on standards and specifications of organizations such as British Standard, AASHTO, and European Standard EN1337.

2.5 Neoprene bridge bearings

Neoprene bearing pads are moulded or cut from a moulded sheet of high-grade, new neoprene synthetic rubber compounds. Neoprene pads permit a smooth and uniform transfer of load from the deck to the substructure and allow beam rotation at the bearing due to deflection of the beam under load. This kind of supports have no movable parts and thermal expansion and contraction are absorbed by the pad ability to give and take in shear. There is no sliding motion between pad and pier or between pad and abutment. Bearings have steel plates separating the elastomeric layers, as shown in Figure 2.10.

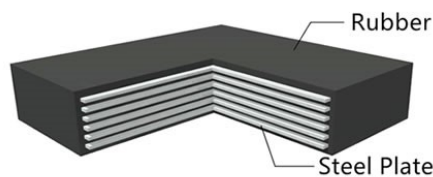


Figure 2.10: Detail of the neoprene bridge bearing

Additionally, they are placed at the top of the piers and a Y-shaped column has usually a couple of them, as it can be seen in the case study of this thesis. Figure 2.11 presents a similar case.



Figure 2.11: Detail of the application of neoprene bearings

2.6 Seismic activity on bridges

The bridges purpose is to minimize distance and help humans win over natural obstructions, rivers in particular, or overpass obstacles. Building earthquake resistant buildings is fundamental for human safety. By contrast, in the case of a destroyed bridge, connected places can be completely isolated from each other.

This is evident in the case of the **1989 San Francisco Bay Area earthquake** that suspended traffic for more than twenty hours because of the damage done to a bridge deck. In 2011, Japan suffered a major earthquake resulting in many bridge collapses, but the losses were minimized because the Japanese implemented earthquake resistant design practices. In the seismic design of a bridge, many factors must be taken into account. For instance, earthquake history of the region is one of the major aspects that need attention from engineers and researchers. Historical facts are useful to predict the most probable times of the year when an earthquake can happen. For this reason, bridge design for earthquake areas needs extensive study of the earthquake history. In case a region has no earthquake history, a minimum load is considered in design, which varies from zone to zone.

Therefore, humans are improving technology, but the bottom line is that it is not possible to beat nature. By contrast, trying to minimize the risk is mandatory. Nowadays, the best solution is to implement earthquake resistant design and to make the best use of seismic retrofitting technology. An optimistic approach regarding seismic design and an accurate investigation with information related to seismic zones contribute to build better and more stable bridges.

2.7 Seismic hazard of the Messina area

The Messina Strait, that separates peninsular Italy from Sicily, is one of the most seismically active areas in the Mediterranean. Specifically, it is responsible for the **Mw 7.1 December 28th 1908 earthquake**, with a related tsunami (run-up height up to 10 m), which caused more than 80,000 casualties. The structure and seismotectonic setting of the region are poorly understood, although the area is highly populated and important infrastructures are planned there. For example, the longest single span ever built bridge has been planned to cross the Messina Strait (Figure 2.13) [1].

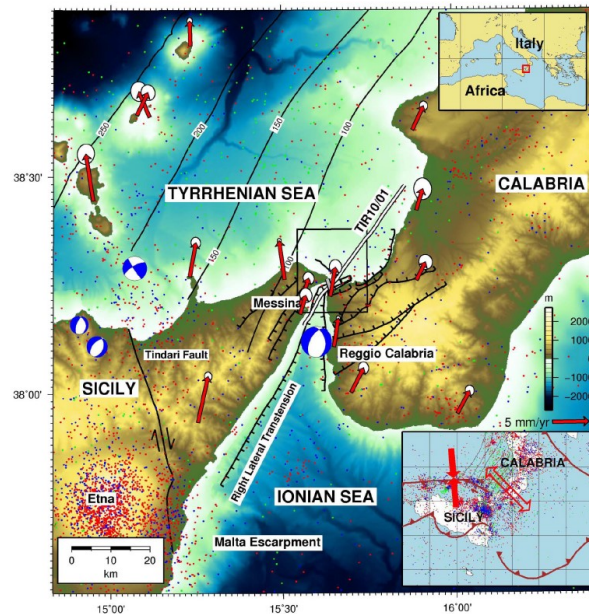


Figure 2.12: Geological setting of the Messina Strait, with location of the planned bridge

The Strait of Messina Bridge is a long-planned suspension bridge across the Strait of Messina, a narrow section of water between the eastern tip of Sicily and the southern tip of mainland Italy. The bridge would be the longest suspension bridge in the world (3,666 m), almost doubling the main span of the Akashi-Kaikyō in Japan. Indeed, the longest span would measure 3,300 m with the height of the towers of 399 m. Figure 13 shows a bridge photomontage.



Figure 2.13: Photomontage of the Strait of Messina Bridge

Additionally, the city of Messina is located within an important tectonic structure, the Messina Strait, which divides the Southern Apennines from the Sicilian-Maghrebian Chain. This area is characterized by a significant and recent uplift, as well as by the frequent strong seismicity occurring in historical times [2].

Chapter 3

Deterioration models

3.1 Corrosion

Corrosion of embedded reinforcing steel is a dangerous phenomenon that affects reinforced concrete (RC) structures. Corrosion is considered to initiate when the chloride concentration around the reinforcement reaches a threshold to cause the dissolution of the protective film. When the corrosion of steel bars develops significantly, it affects the structural serviceability, even spalling of the concrete cover and also the structural safety of reinforced concrete members [3]. Corrosion of reinforcing steel may occur if the pH of the concrete is decreased, either from chemical attack or from the reaction of the concrete with CO₂ in the atmosphere. It may also occur if sufficient chloride ions reach the bar. These are typically introduced into the concrete from sea water.

Usually, corrosion can be distinguished into two types: general and pitting corrosion. General concerns a substantial area of reinforcement with more or less uniform metal loss over the perimeter of the reinforcing bar. It produces rust staining on the concrete cover, that can be identified quite easily during an inspection of a structural element. On the other hand, pitting corrosion is localized in small areas of reinforcement but the steel area loss quantity is bigger. Especially, in chloride environments, several investigations have found that it is more dangerous than the general one, owing to the major form of corrosion in RC structures. However, pitting is more difficult to be noticed during the inspection because produces little rust staining on the concrete surface [4].

When corrosion of the reinforcement bars occurs and moves on, the cover concrete fails and this induces tensile stresses, consequently, longitudinal splitting cracks originate. Furthermore, corrosion of reinforcement reduces the cross-sectional area of reinforcing bars, the resistance capacity and the ductility performance [5, 6]. From a structural point of view, corrosion affects shear and moment capacity, tension stiffening and, consequently, deflection. Plastic rotation capacity is influenced as well and this can determine seismic resistance, considering a corroded structure can collapse abruptly [7]. Thus, after corrosion

occurs, reliable assessment of structural capacity is important to check every kind of failure mode [3].

To quantify corrosion there are many formulas, some of them are mentioned below. Usually, the most important parameter is the corrosion rate, which is defined as the loss of metal per unit of surface area per unit of time. According to the paper by Dimitri V. Val [4], assuming a constant corrosion rate, the reduction in the diameter of a corroding reinforcing bar ΔD after t years since corrosion initiation can be estimated (in millimetres) as:

$$\Delta D(t) = 0.0232 i_{corr} t \quad (3.1)$$

$$A_s(t) = n \frac{\pi [D_0 - \Delta D(t)]^2}{4} \geq 0 \quad (3.2)$$

Assuming that the corrosion current density, defined by i_{corr} , is the same for a group of n reinforcing bars having the same diameter D_0 , so their cross-sectional area after t years of general corrosion is computed through Eq. (3.2) [4].

By contrast, regarding pitting corrosion it is possible to compute after t years since corrosion starting as follows:

$$p(t) = 0.0116 i_{corr} t R \quad (3.3)$$

Successively, as suggested by Val and Melchers [8], a hemispherical model of a pit is used as it is shown in Figure 3.1.

Therefore, based on this information, the net cross-sectional area of reinforcement bars, $A(t)$, in a reinforcing bar with a diameter d_0 can be computed as follows:

$$A(t) = \begin{cases} \frac{\pi d_0}{4} - A_1 - A_2 & p(t) \leq \frac{\sqrt{2}}{2} d_0 \\ A_1 - A_2 & \frac{\sqrt{2}}{2} d_0 < p(t) \leq d_0 \\ 0 & p(t) > d_0 \end{cases} \quad (3.4)$$

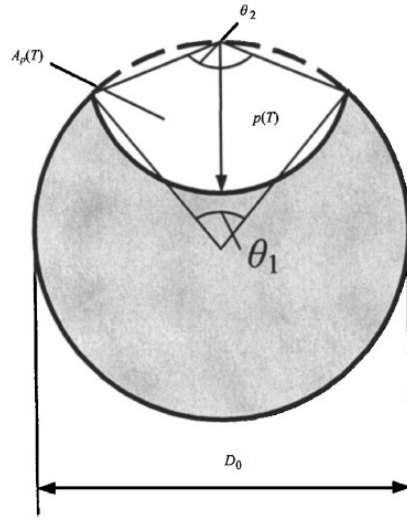


Figure 3.1: Pitting configuration of RC structures by Val and Melchers

The parameters used above can be represented as:

$$A_1 = \frac{1}{2} \left(\theta_1 \left(\frac{d_0}{2} \right)^2 - a \left| \frac{d_0}{2} - \frac{p(t)^2}{d_0} \right| \right) \quad (3.5)$$

$$A_2 = \frac{1}{2} \left(\theta_2 p(t)^2 - a \frac{p(t)^2}{d_0} \right) \quad (3.6)$$

$$a = 2p(t) \sqrt{1 - \left(\frac{p(t)}{d_0} \right)^2} \quad (3.7)$$

$$\theta_1 = 2 \arcsin \left(\frac{a}{d_0} \right), \theta_2 = 2 \arcsin \left(\frac{a}{2p(t)} \right) \quad (3.8)$$

Due to corrosion, the following effects must be taken into account:

- Steel area reduction, in the main longitudinal bars and the stirrups
- Changes in the ductility of carbon-steel bars owing to pitting corrosion
- Concrete area reduction because of cover cracking and spalling

- Changes in the strength and ductility of the concrete in compression, due to bar expansion
- Change in tension stiffening because of cover cracking and bond deterioration
- Bond dependence on the corrosion level in the bars

When corrosion begins, a volume expansion of the corrosion products compared with virgin steel occurs. As a consequence, corrosion causes cracks through the concrete cover by determining its spalling. In this way, the strength, ductility and flexural capacity reduction of the RC members are expected. For this reason, these aspects must be considered in the numerical analysis.

Figure 3.2 shows the corrosion-product accumulation around a bar (a) and the total corrosion crack width w_{cr} (b) [9].

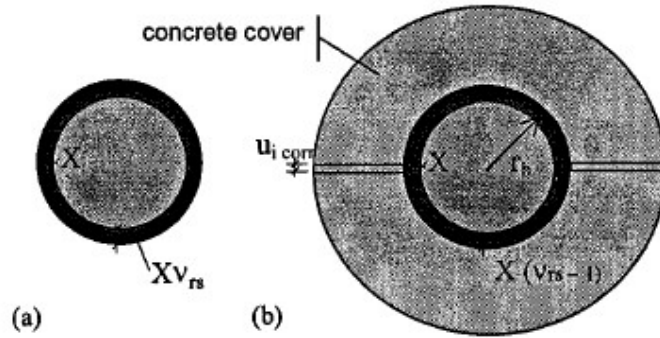


Figure 3.2: (a) Corrosion-product accumulation around a bar and (b) total corrosion crack width w_{cr}

Many formulas and methods are used in literature to examine corrosion. Especially, quantifying it is fundamental to know exactly the response of the RC structure. For instance, one-dimensional Fick's second law including the apparent diffusion coefficient of chloride ions of concrete suggested by the AIJ (2004) and JSCE (2008) can be applied. This formula (Eq. 3.10) can be useful to estimate the time when chloride ions diffuse from concrete surfaces to a passive film on the surface of reinforcing steel bars [10]:

$$C_0 = 13.14 \cdot C_{air}^{0.64} \quad (3.9)$$

$$CI = C_0 \left[1 - \operatorname{erf} \left(\frac{0.1 \cdot c}{2\sqrt{D_c t}} \right) \right] \quad (3.10)$$

$$\log D_c = -6.77(w/c)^2 + 10.1(w/c) - 3.14 \quad (3.11)$$

Where CI is the chloride concentration on the surface of reinforcing steel bars (kg/m^3), C_0 is the chloride concentration of the concrete surface (kg/m^3), c is the diffusion distance as the concrete cover (mm), D_c is the apparent diffusion coefficient of chloride ions ($cm^2/year$), w/c is the water-cement ratio, t is a specified service period expressed in years and erf is the error function. The relationship between the chloride concentration on the surface of reinforcing steel bars and one of the concrete surfaces was estimated empirically with a regression equation. Then, it is possible to quantify the corrosion by means the average weight loss of reinforcing steel bars, ΔW_{avg} [11]:

$$V_{corr} = \frac{78}{\sqrt{c}} (0.578 \cdot CI + 0.023(w/c) - 1.52) \quad (3.12)$$

$$\Delta W_{avg} = \frac{4V_{corr}}{\gamma \cdot d_{bi}} \quad (3.13)$$

Where V_{corr} is the corrosion rate ($mg/cm^2/year$), γ is the density of reinforcing steel bars (approximately 7850 mg/cm^3) and d_{bi} is the diameter of reinforcing steel bars (mm). Moreover, to study the mechanical properties of corroded reinforcing steel bars, Equation (3.14) that puts in relationship the yielding stress of steel bars with the investigation time can be applied, after corrosion occurs [12]:

$$f_y = (1 - 1.14(\alpha \cdot \Delta W_{avg})) f_{yo} \quad (3.14)$$

Where α is the modification factor for the pitting corrosion effect (it can be set as 2.0), f_y and f_{yo} are the stresses before and after corrosion.

3.2 Marine chloride-induced corrosion

As can be seen, corrosion is fundamental to take into account. In addition, it is aggravated if the structure is placed in a marine environment, because corrosion occurs more quickly. For example, in the case of a bridge, RC columns exposed to chloride environments inevitably suffer from the effect of chloride-induced corrosion. Consequently, it determines cracking or spalling of concrete cover and steel reinforcement volume expansion [13, 14].

Specifically, the difference between pitting and uniform corrosion can be clearly seen. This is evident in the case of chloride-induced attack, because pitting affects more the structure leading to localized losses in reinforcing bar areas. Moreover, it is known by literature

[15, 16] that once concrete cracking takes place, reinforcing steel corrosion rate increases significantly due to the easier ingress of oxygen and water. Additionally, corrosion can increase its hazard in the presence of seismic fragility. This is certainly true in the case of RC bridge columns that are the most affected resistant elements, because they are more vulnerable than the superstructure to seismic motions [17]. Thereby, to perform this kind of analysis it is recommendable to follow a recent method (2017) suggested by Cui et al. This study aims to obtain the residual reinforcement diameter $d(t)$ and the residual pitting depth $p(t)$ at time t . Finally, **the residual cross-sectional area of steel reinforcement** $A(t)$, is determined by Equation (3.16), as follows [18, 19]:

$$d(t) = d_0 - 2 \int_{t_{corr}}^t \lambda(t) dt \quad (3.15)$$

$$A(t) = \frac{\pi}{4} [d(t)]^2 \quad (3.16)$$

Where d_0 represents the initial diameter of the reinforcement bars.

In conclusion, it can be mentioned that the effect of marine chloride-induced corrosion may not be neglected. Especially, when seismic analysis of the RC bridges substructures in marine environments is performed.

3.3 Bonding

Bonding can be mentioned as an essential characteristic in RC structural elements. Bonding regards the force permitting the bond between concrete and steel reinforcement. Moreover, bond is one of the main keys to assess the performance of RC structures against seismic load.

In RC structures, the concrete cover plays the role of protection of the steel bars from the external environment. A good transfer of force between the two materials can only be achieved by a strong interaction between them. Indeed, such attributes ensure the durability and serviceability of the structure.

Bond performance of reinforced concrete is important in the study of the load transfer mechanism from concrete to the inner reinforcing bar and vice versa. Moreover, bond strength is influenced by curing conditions, concrete compressive strength, concrete cover, embedded length, flexural crack length, chemical adhesion, and friction. Bond strength is also expressed as a function of the applied load, bars diameter, and embedded length. The relationship among bonds between concrete and steel bars, durability, and chloride penetration rate are nowadays structural engineering challenges [20].

When reinforcement in concrete is subjected to corrosion, the internal pressure is created

due to volumetric increase upon the formation of iron oxides. As corrosion of the reinforcement bars propagates, the surrounding concrete eventually fails to carry the induced tensile stresses and longitudinal splitting cracks develop. After cracking, the structural strength decreases markedly with further corrosion. Afterwards, corrosion of reinforcement reduces the cross-sectional area of reinforcing bars and thereby their capacity and ductility. That is, the ability of the structure to absorb large energy and produce certain deformation without destroying under a shock or vibration load [3].

From the structural point of view, corrosion affects shear and moment capacity, tension stiffening and especially, seismic resistance. Consequently, a corroded structure can collapse abruptly, so reliable assessment of structural capacity and corrosion analysis is particularly important.

In the standard, e.g. in Model Code 2010, this topic is discussed and the splitting strength is estimated as follows:

$$\tau_{bu,split} = \eta_2 \cdot 6.5 \cdot \left(\frac{f_{cm}}{25}\right)^{0.25} \cdot \left(\frac{25}{\phi_m}\right)^{0.2} \left[\left(\frac{c_{min}}{\phi_m}\right)^{0.25} \left(\frac{c_{max}}{c_{min}}\right)^{0.1} + k_m \cdot K_{tr} \right] \quad (3.17)$$

Where η_2 is 1.0 and 0.7 for “good” and “all other” bond conditions respectively; f_{cm} is the mean cylinder compressive strength in MPa; ϕ_m is the diameter of the anchored bar in mm; c_{min} and c_{max} are given in the equations below; k_m and K_{tr} are the confinement coefficient and the amount of the transverse reinforcement respectively. It should be noted that Eq. (3.17) assumes constant bond stress over a bonded length of five times the diameter of the anchored bar.

$$c_{min} = \min(c_s/2, c_x, c_y) \quad (3.18)$$

$$c_{max} = \max(c_s/2, c_x) \quad (3.19)$$

Where c_s is the clear spacing between main bars; c_x is the cover in x-direction and c_y is the cover in y-direction; $k_m = 12$ for bars located within $5\phi_m \leq 125mm$ from a stirrup corner, $k_m = 6$ if $c_s > 8c_y$ or $k_m = 0$ if $c_s < 8c_y$, or if a crack can propagate to the concrete surface without crossing transverse links.

On the other hand, the transverse reinforcement can be expressed by:

$$K_{tr} = n_t A_{st} / (n_b \phi_m s_t) \leq 0.05 \quad (3.20)$$

Where n_t is the number of legs of confining reinforcement crossing a potential splitting-failure surface at a section, A_{st} is the cross-sectional area of one leg of a transverse bar, s_t is the longitudinal spacing of confining reinforcement and n_b is the number of anchored bars or pairs of lapped bars in the potential splitting surface [21].

The relationship in Eq. (3.17) is useful, but it does not take into account the decrease of the confinement provided by the concrete cover due to corrosion. Therefore, a new formula [3] is developed reducing the factor for concrete cover to 1, thus the reduced splitting strength is obtained as:

$$\tau_{bu,split,red} = \eta_2 \cdot 6.5 \cdot \left(\frac{f_{cm}}{25}\right)^{0.25} \cdot \left(\frac{25}{\phi_m}\right)^{0.2} (1 + k_m \cdot K_{tr}) \quad (3.21)$$

Where these terms are the same ones of Eq. (3.17). The expression above is based on an embedment length of five times the bar diameter.

The purpose of this new model, called **ARC2010**, is to be used in the structural assessments of corroded structures in engineering practice. The use of the assessment model aims to improve the estimation of the anchorage capacity of concrete structures with corroded reinforcement. If the ARC2010 assessment model is used, this will make it possible to keep **using more corrosion-damaged concrete bridges** [3].

Another aspect related to bond regards the fundamental presence of stirrups, corroded and non-corroded, that changes the behaviour of an anchorage region, the failure mode and the bond capacity. Corrosion of stirrups not only reduces the stirrup area but also weakens the confinement provided by the concrete towards extensive cover cracking. If both longitudinal and transverse reinforcements are corroded, anchorage and shear failure become more probable.

A literature study [22] suggests that for large corrosion penetration causing extensive cover cracking, stirrups play an important role in terms of being the main source of confinement. It can be checked that failure is relatively brittle without stirrups. Thus, their presence is fundamental to prevent corrosion in the longitudinal bars. The least bond deterioration can be measured on the corner bars in the uncorroded stirrups and this depends on the effective interaction between the stirrups and the main bars at the angle of the corner. However, it can be concluded that significant bond deterioration usually starts only when the level of stirrup corrosion is very high, for example more than 50% [22].

3.4 Validity of corrosion models

The concept of corrosion analysis, discussed in the Introduction, is a matter of increasing concern. Over the years new studies have discovered how to prevent corrosion and new models of analysis develop.

Nowadays, most bridges are affected by this issue causing the decrease of the load carrying capacity, the long-term reduction in the structural performance of RC columns and the reduction of the ductility performance [23]. Moreover, corrosion can be emphasized by the earthquake action, which reduces the service life of the structure. That is, a bridge can survive an earthquake in normal conditions, but not in a deteriorating state, e.g. due to chloride contamination. For this reason, new studies have developed a model of marine chloride-induced corrosion in order to prevent this phenomenon which can be applied to most deteriorated bridges located on the sea.

A recent study [24] recommends the performance of this kind of corrosion analysis. It proposes a new time-dependent corrosion rate model for RC bridge substructures exposed to typical marine environments. The combination of post-cracking corrosion rate and pitting corrosion model are integrated to produce an accurate simulation of the effect.

The chloride-induced reinforcement corrosion process could be divided into three main steps as Figure 3.3 illustrates [25, 26]:

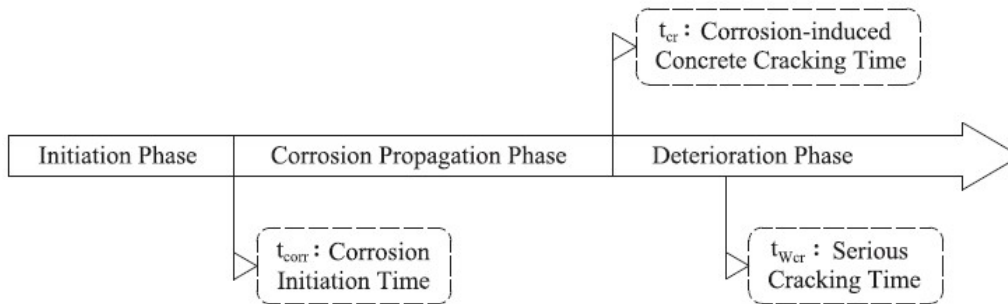


Figure 3.3: Phases of chloride-induced corrosion process of reinforcing steel

In the *initiation phase*, the access of chloride ions occurs from the external environment. This phase lasts until the ions reach the surface of the reinforcement bars. Once the corrosion initiation time, t_{corr} , has been reached, the *corrosion propagation phase* begins. The diffusion process of chloride ions in the concrete can be described by means of the Fick's second law based on the semi-infinite solid assumption. This is shown in Equation (3.22) [17]:

$$\frac{\partial C(x, t)}{\partial t} = \frac{\partial}{\partial x} \left[D \frac{\partial C(x, t)}{\partial x} \right] \quad (3.22)$$

Where D = diffusion coefficient; $C(x, t)$ = chloride ion concentration; x = depth from concrete surface; and t = time in years.

When the chloride concentration at the steel reinforcement surface reaches a critical value C_{cr} , the point in time is called corrosion time, t_{corr} (Equation 3.23) and it depends on many factors listed in Figure 3.4 [27, 28]:

$$t_{corr} = X_1 \left[\frac{d_c^2}{4k_e k_t k_c D_0 (t_0)^n} \left[\text{erf}^{-1} \left(1 - \frac{C_{cr}}{C_0} \right) \right]^{-2} \right]^{\frac{1}{(1-n)}} \quad (3.23)$$

Parameter	Units	Distribution	Mean	St. dev.	
A_{cs}	Tidal	mass%	Normal	7.758	1.36
	Atmospheric (0 m)	of binder		6.44	0.894
ε_{cs}	Tidal	mass%	Normal	0	1.105
	Atmospheric (0 m)	of binder		0	0.753
Critical chloride concentration C_{cr}	mass% of binder	Normal	0.8	0.1	
Diffusion factor D_0	mm ² / yr	Normal	220.9	25.4	
Curing factor k_c	—	Normal	1.5	0.3	
Test method factor k_t	—	Normal	0.85	0.024	
Environmental factor k_e	—	Normal	1	0.3	
Aging factor n	—	Beta	0.25	0.05	
Model uncertainty factor X_1	—	Lognormal	1	0.05	

Figure 3.4: Deterioration parameters considered in the case study of the paper [24]

$$C_0 = A_{cs}(w/c) + \varepsilon_{cs} \quad (3.24)$$

The previous deterioration parameters have been inserted by Cui et al. into a *Monte Carlo Simulation* (MCS), to generate 10000 samples and the value of the corrosion time has been found to be:

$$t_{corr} = 11.3 \text{ years}$$

Once the *corrosion propagation phase* has begun, the deterioration process can occur in two possible corrosion forms: pitting and general. Pitting is the primary deterioration form leading to localized losses in reinforcing bar areas and concentrates over small areas of reinforcement. By contrast, general corrosion is due to a uniform effect on the surface and it is employed to study the influence of deterioration on RC members in chloride environments.

Finally, at initial cracking time, t_{cr} , i.e. the time in which the concrete cover cracks, the *deterioration phase* starts, reaches severe cracking time, t_{Wcr} , and eventually the service life of the bridge ends.

The initial cracking time has been estimated by means of Eq. (3.25):

$$t_{cr} = \left[\frac{p_{cr} d_c}{0.52494(1 - w/c)^{-1.64}} \right]^{1.40845} + t_{corr} \quad (3.25)$$

Where d_c is the concrete cover, w/c is the water-cement ratio, p_{cr} is the critical pitting penetration computed by the equation in CECS code [29], as follows:

$$p_{cr} = 0.012 \frac{d_c}{d_0} + 0.00084 f_{cu} + 0.018 \quad (3.26)$$

where f_{cu} = compressive strength of concrete.

Thus, $p_{cr} = 0.0692$ and consequently, $t_{cr} = 15.7$ years.

The severe cracking time is implicit in the formulas and so, it has been determined by numerical methods. However, experimental studies [24] have demonstrated that t_{Wcr} occurs usually 6.4 years after t_{cr} .

$$t_{Wcr} \simeq 22.1 \text{ years}$$

Once parameters t_{cr} and t_{Wcr} are estimated, the whole corrosion rate model could be obtained by applying the following steps.

3.4.1 Corrosion rate model

The corrosion rate model is expressed by the corrosion rate function, $\lambda(t)$. Experimental studies indicate that it depends on time during the service life as $\lambda(t)$ is affected by many factors [30, 31, 32, 33]. For this reason, the function can be split into three phases based on the precise instant of time as follows:

$$\lambda(t) = \begin{cases} \lambda_1(t) & t_{corr} < t \leq t_{cr} \\ (t - t_{cr}) \cdot \frac{\lambda_3(t_{Wcr}) - \lambda_1(t_{cr})}{t_{Wcr} - t_{cr}} + \lambda_1(t_{cr}) & t_{cr} < t \leq t_{Wcr} \\ \lambda_3(t) & t > t_{Wcr} \end{cases} \quad (3.27)$$

1. The first phase, $\lambda_1(t)$: from the initial corrosion to the initial cracking;
2. The second phase, $\lambda_2(t)$: from the initial cracking to severe concrete cracking, it is assumed to increase with time linearly;
3. The third phase, $\lambda_3(t)$: after severe concrete cracking.

In the first phase, it can be computed as [34]:

$$\lambda_1(t) = 0.0116 \cdot i_{corr,0} \cdot 0.85 \cdot (t - t_{corr})^{-0.29} \quad (3.28)$$

Where $i_{corr,0}$ is the corrosion current density at the beginning of corrosion propagation phase, expressed as:

$$i_{corr,0} = \frac{37.8(1 - w/c)^{-1.64}}{d_c} \quad (3.29)$$

The second phase is developed in the study because it accounts for the gradual increase of corrosion rate after initial concrete cracking. The corrosion rate, $\lambda_2(t)$, in this phase is assumed to increase linearly with time. In this case this assumption can solve issues with the discontinuity in the CECS model [29].

$$\lambda_2(t) = (t - t_{cr}) \cdot \frac{\lambda_3(t_{Wcr}) - \lambda_1(t_{cr})}{t_{Wcr} - t_{cr}} + \lambda_1(t_{cr}) \quad (3.30)$$

The last phase depicts the corrosion rate after severe concrete cracking. Equation (3.31) is used to compute it:

$$\lambda_3(t) = (4.5 - 26 \cdot \lambda_1(t)) \cdot \lambda_1(t) \quad (3.31)$$

The behaviour of the corrosion rate function shows a curve that begins vertically at the corrosion time and then reduces sharply during the first few years. Subsequently, the corrosion rate changes more slowly and reaches a nearly uniform value until the initial cracking time. As recent studies suggest [15, 33], after this phase the corrosion rate function has a large continuous increase and crack growth, as concrete cracking leads to easier ingress of chlorides, oxygen and water. After reaching a peak value, $\lambda(t)$ decreases slowly to a

steady state in critical cracking condition. This depends on the difficulty that oxygen and moisture have to attain the steel reinforcement surface after the accumulation of corrosion products.

A case study is used in order to apply the corrosion rate model to this structure. The input parameters used are listed in Figure 3.5 [13, 24, 35, 36].

Parameter	Units	Distribution	Mean	St. dev.
Compressive strength of unconfined concrete	MPa	Lognormal	32.4	6.48
Ultimate compressive strain of unconfined concrete	—	Lognormal	0.005	0.001
Compressive strength of confined concrete	MPa	Lognormal	35.8	7.16
Ultimate compressive strain of confined concrete	—	Lognormal	0.0085	0.0017
Yield strength of steel	MPa	Lognormal	Eq. (14)	0.07mean
Ultimate strain of steel	—	Lognormal	Eq. (16)	0.2mean
Elastic modulus of concrete	MPa	Normal	3×10^4	3600
Elastic modulus of steel	MPa	Normal	2×10^5	4000
Concrete cover depth	mm	Normal	50	7.5
Bearing shear modulus	MPa	Uniform	1.365	0.407
Bearing coefficient of friction	MPa	Lognormal	0.36	0.036
Translational stiffness of foundation	kN/m	Uniform	6.2×10^5	1.8×10^5
Rotational stiffness of foundation	kN m/rad	Uniform	1.8×10^7	5.2×10^6
Passive stiffness of abutment	kN/m	Uniform	3.2×10^5	8×10^4
Active stiffness of abutment	kN/m	Uniform	7×10^4	2×10^4
Damping ratio	—	Normal	0.045	0.0125
Deck mass ratios	—	Uniform	1.0	0.058
Abutment-deck gaps	mm	Normal	60	1.62

Figure 3.5: Random variables considered in finite element bridge model

Once the input parameters are known, the output behaviour of the corrosion rate function can be plotted. In fact, Figure 3.6 represents the findings regarding the splash and atmospheric zone.

In the present thesis, each formula and equation has been followed to implement the corrosion rate model of the paper by Cui et al. for the splash zone. This analysis was made possible by *Matlab*, and the script is shown in the Appendix.

The input parameters were those used by Cui et al. and so, Figure 3.7 illustrates the function that was obtained.

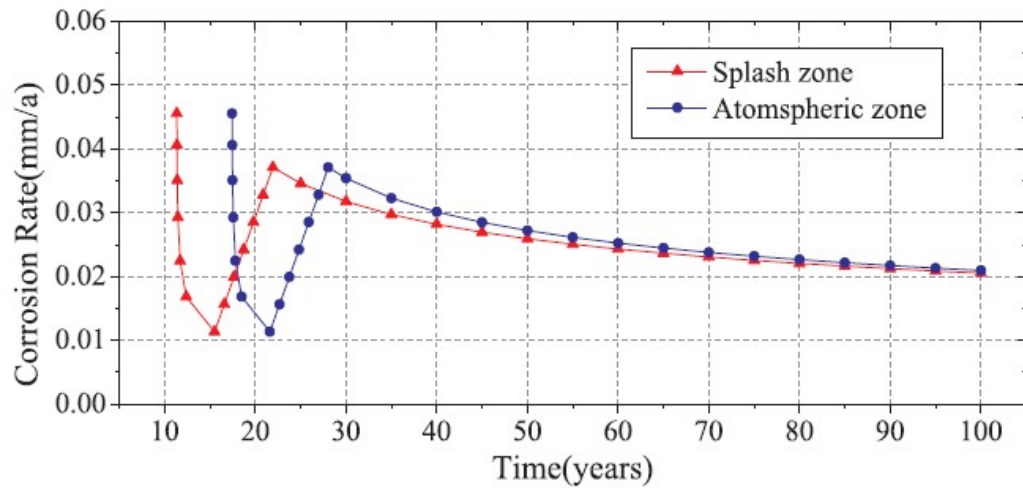


Figure 3.6: Corrosion rate curves found by Cui et al.

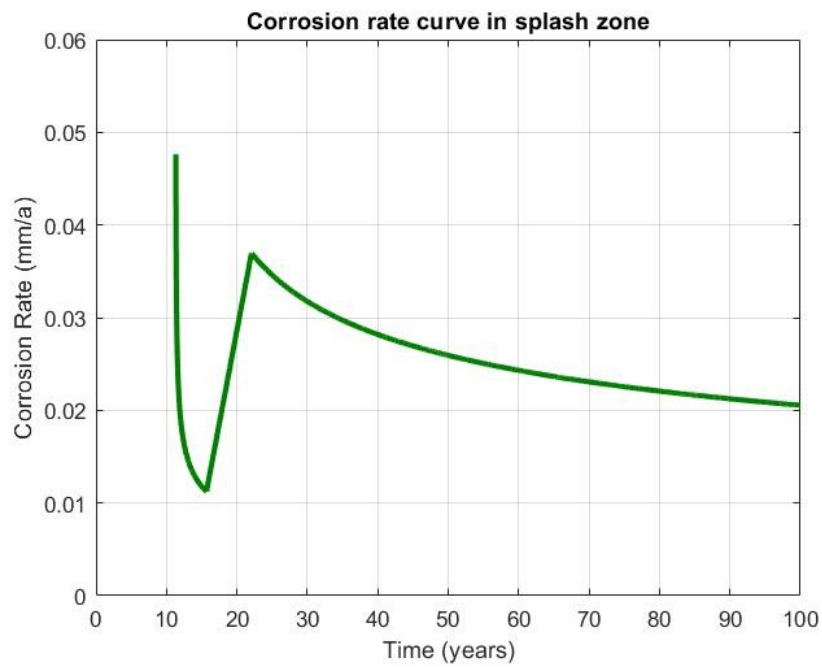


Figure 3.7: Corrosion rate graph obtained by *Matlab*

Here, a comparison between two figures has been carried out in order to check if the model in the paper corresponds to the implemented one. Thereby, it can be shown overlaying the green curve obtained by *Matlab* to the red points found in the paper. The green curve refers only to the splash zone.

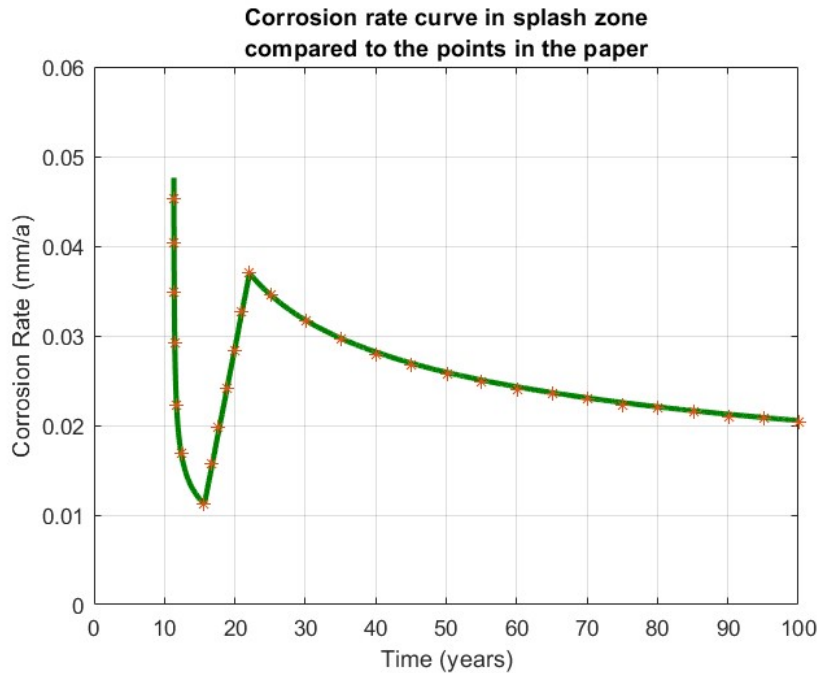


Figure 3.8: Comparison between corrosion rate obtained by *Matlab* and points in the paper

The most interesting aspect of this graph is that the two figures coincide. This significant outcome means that the implemented formulation makes sense because it corresponds to the one of the paper by Cui et al. The present study was looking for this kind of check in order to develop the same corrosion rate model. Next, it can be easily applied to the bridge case study discussed in the following chapters of the dissertation.

Once the check has been carried out, the study can continue to be developed.

Subsequently, the general and pitting corrosion models have been applied to compute $A(t)$, i.e. the net cross-sectional area of reinforcement bars subject to corrosion at time t .

3.4.2 General corrosion model

The general corrosion model consists of a uniform distribution. The residual reinforcement diameter at time t can be determined by Eq. (3.15).

Accordingly, the residual cross-sectional area of reinforcement at any time t is expressed as in Eq. (3.16):

$$A(t) = \frac{\pi}{4}[d(t)]^2$$

Figure 3.9 shows the general corrosion situation obtained by the *Matlab* script and compared to the blue points of the paper by Cui et al.

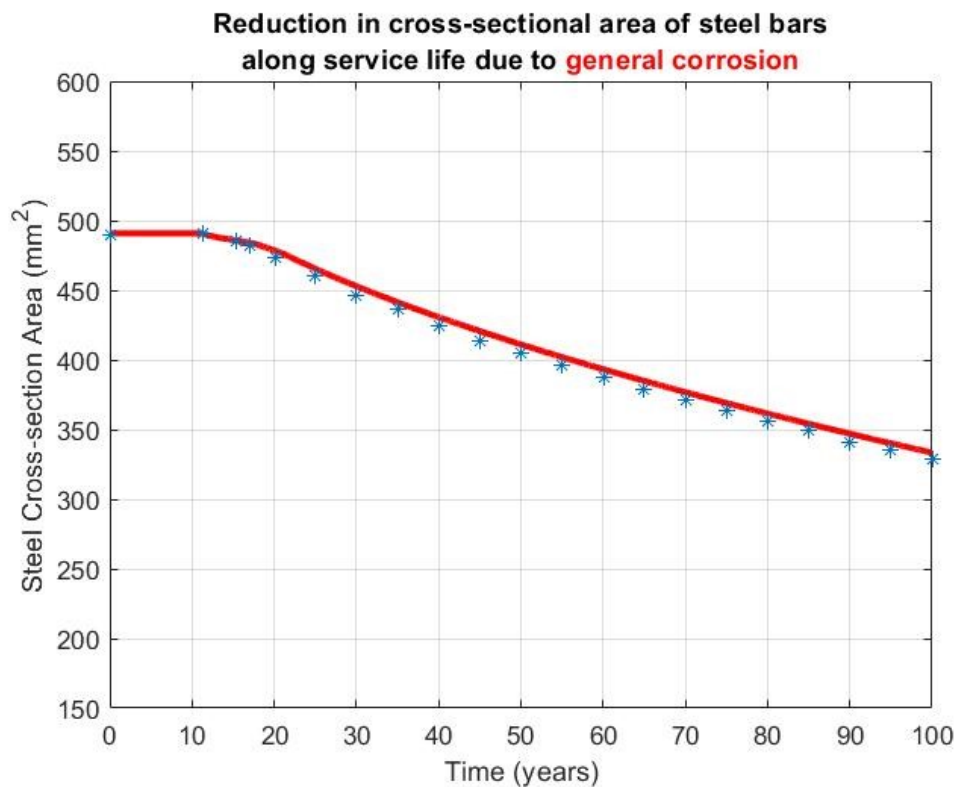


Figure 3.9: Comparison between the residual area obtained by *Matlab* and points in the paper

In this case, the curve follows the distribution of the points and so the result is as the study expected.

3.4.3 Pitting corrosion model

It is the primary cause for marine chloride-induced corrosion under service conditions. The model proposed by Val and Melchers [4] has been taken into account to simulate the development of pitting corrosion. In the model, pitting corrosion is assumed to take a hemispherical form as shown in Figure 3.1. It represents the pitting depth that expands with time, denoted by $p(t)$ at any time t and expressed by:

$$p(t) = R \int_{t_{corr}}^t \lambda(t) dt \quad (3.32)$$

Where $R = 7.1$ is the amplification factor representing the ratio between maximum and uniform corrosion penetration. $A(t)$ is the net cross-sectional area of reinforcement bars that depends on the pitting depth expansion. The area can be computed by Eq. (3.4).

Figure 3.10 depicts the findings found by Cui et al. By contrast, Figure 3.11 shows what it has been found by the *Matlab* code for the pitting corrosion situation in splash zone.

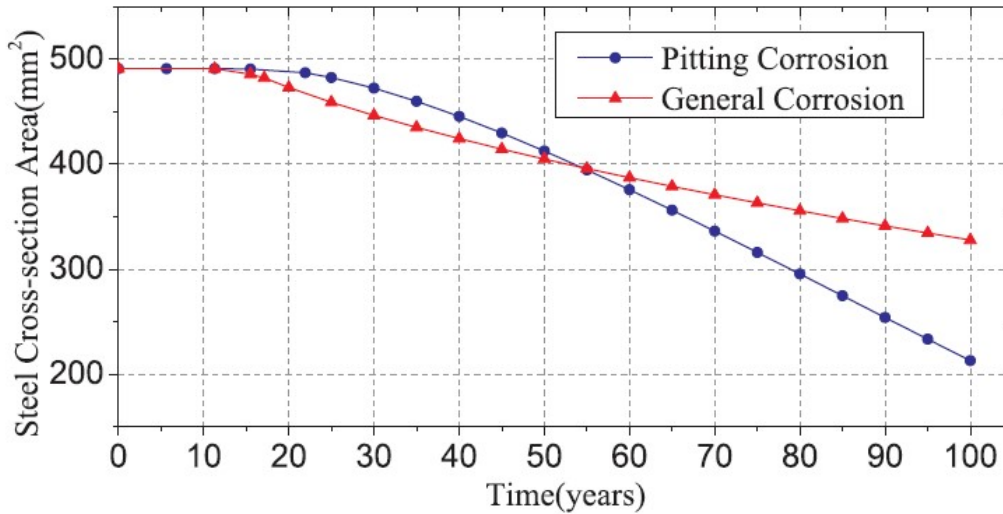


Figure 3.10: Comparison by Cui et al. of pitting and general corrosion in splash zone

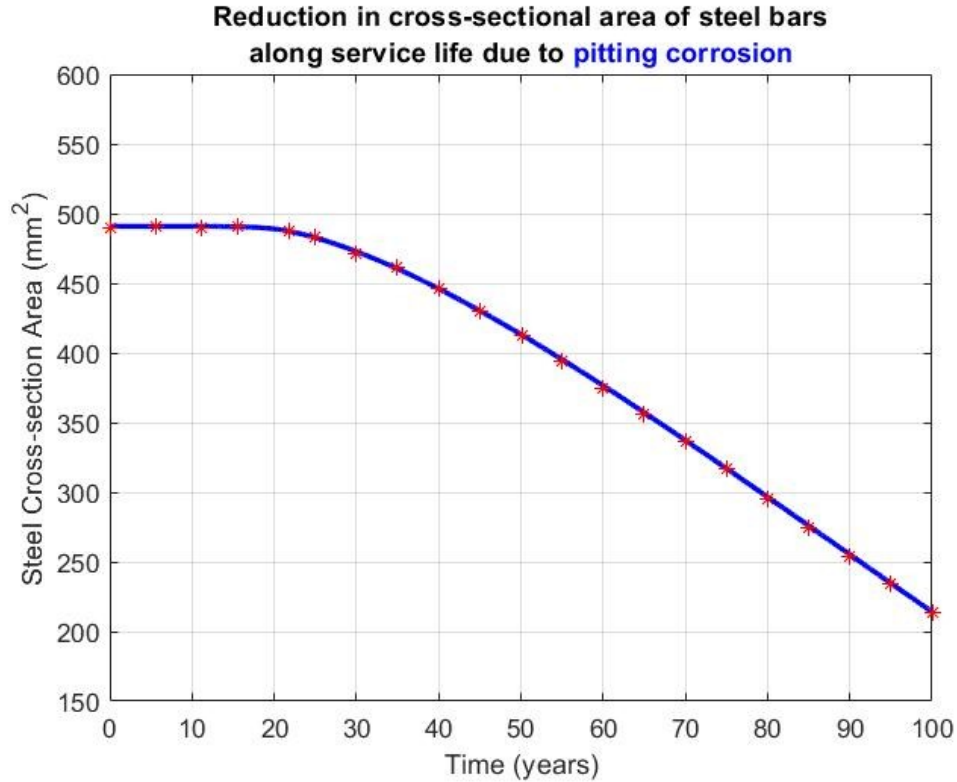


Figure 3.11: Comparison between the residual area obtained by *Matlab* and points in the paper

A positive correlation was found between the residual area obtained by *Matlab* and the points in the paper. Indeed, the two models match perfectly, so the script is valid and runs well.

Finally, a comparison between the two figures for the case of pitting and general corrosion in splash zone is shown. The continuous lines in blue and red, respectively related to pitting and general case, have been found by *Matlab* and correspond to the points in the paper by Cui et al.

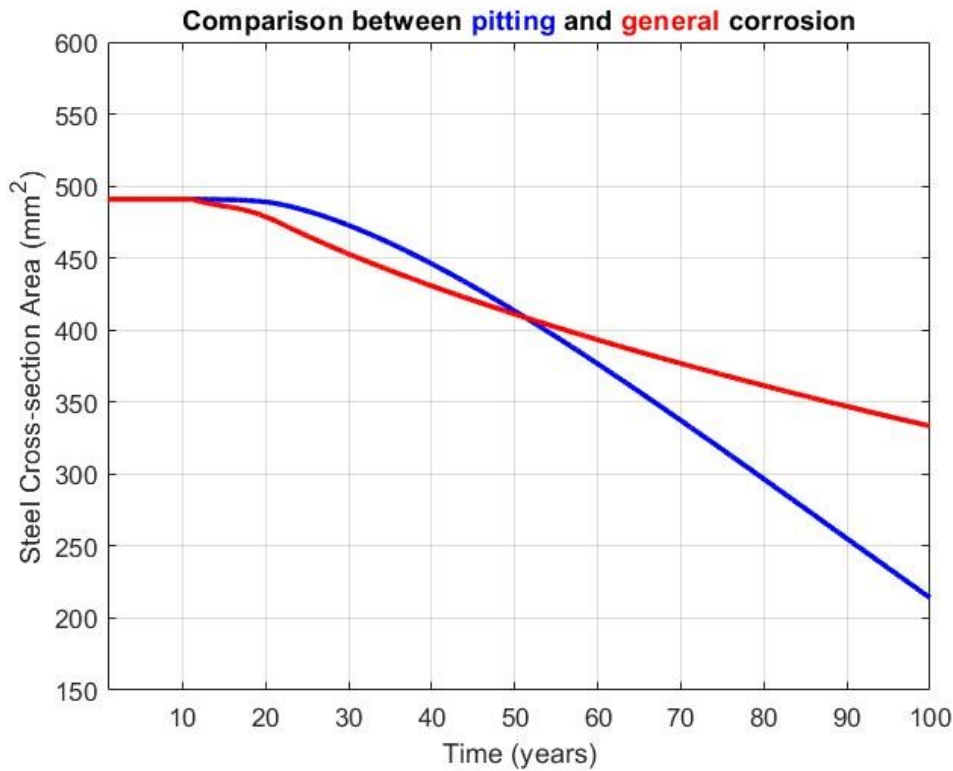


Figure 3.12: Comparison of pitting and general corrosion in splash zone

As can be seen from Figure 3.12, steel cross-sectional area reduction regarding pitting corrosion exceeds general corrosion and the gap between them increases quickly with time. Consequently, the usual general corrosion model can underestimate the long-term influence of chloride-induced corrosion on structural performance. That is, it can be non-conservative for the design and maintenance of RC substructures of the bridge [24].

In the following chapters this corrosion model, which has been validated here, is applied to the bridge case study of this thesis.

Chapter 4

Bridge case study

4.1 Typology

The bridge case study regards a motorway overpass. The platform is made up of a 7.5 m carriageway, 1.5 m docks and 2.5 m wide pedestrian sidewalks as shown in Figure 4.2. Thus, the total width of the bridge is 15.5 m. The representation of the front view can be shown in Figure 4.1.

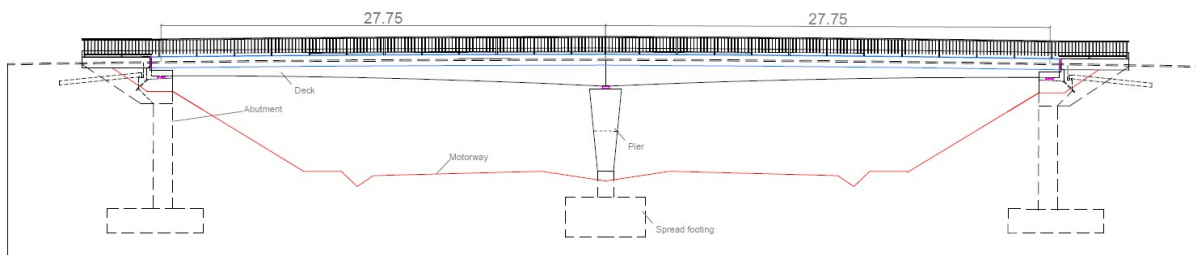


Figure 4.1: Representation of the bridge front view

Moreover, this bridge overpasses a motorway, which is represented in Figure 4.3. This motorway consists of two carriageways of 7 m differentiated by an 8 m wide median, and with a 2 meters gutter. For this reason, a 2-span bridge has been chosen, in order to locate a central pier in the median. An additional lateral distance of 2.4 m has been determined on each side of the gutter for safety reasons, since vehicles circulate at high speed in the motorway.

The typology of the abutments is open to be more aesthetic and safer. Therefore, the

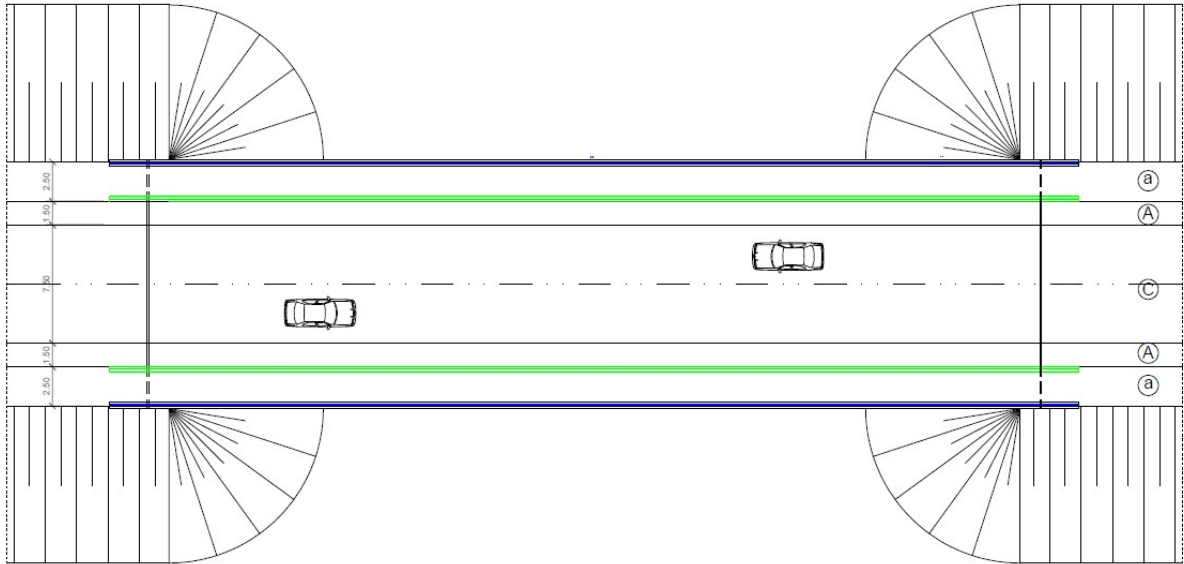


Figure 4.2: Representation of the bridge top view



Figure 4.3: Representation of the motorway morphology

total length of the bridge is 55.5 m, with a 27.75 m span. Table 4.1 summarizes geometric features.

Table 4.1: Geometric data of the bridge

L total	55.5 m
L span	27.75 m
Abutments slope	2:3

Bridge engineering suggests that a span length, which measures $L \simeq 30$ m, requires a solid concrete slab with lightnings such as cross-section of the bridge, since the cost is lower as well.

This corresponds to the bridge case study, thus a solid concrete slab with lightnings is chosen.

4.2 Longitudinal profile

4.2.1 Convex profile

A convex profile is required to design the bridge in the longitudinal profile with a coefficient of curvature of $K_v = 2500$. A convex profile is usually used in order to favour longitudinal drainage of rainwater. Thus, in the case study the total length of the junction is 100 m and the slope is defined as $i_1 = i_2 = 2\%$.

Once the span length of 55.5 m is known, the convex profile starts at the coordinate $x=22$ m and ends at $x=78$ m. In this way, the height increase in the center is equal to 0.157 m. The pattern is shown in Figure 4.4, not in scale.

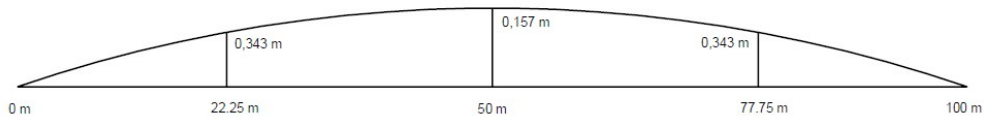


Figure 4.4: Representation of the convex junction

4.2.2 Variable depth definition

A variable depth is chosen in the bridge case study in order to reduce cross-section in the abutments, to optimize material and to have a major aesthetic appeal.

To determine the variable depth geometry, two design conditions have been used:

1. Depth above the pier: $H = \frac{L}{20} = 1.57 \text{ m}$
2. Depth above the abutments: $H = \frac{L}{40} = 0.78 \text{ m}$

Following these conditions, the curve that joins the two edges by means of an arc has been determined.

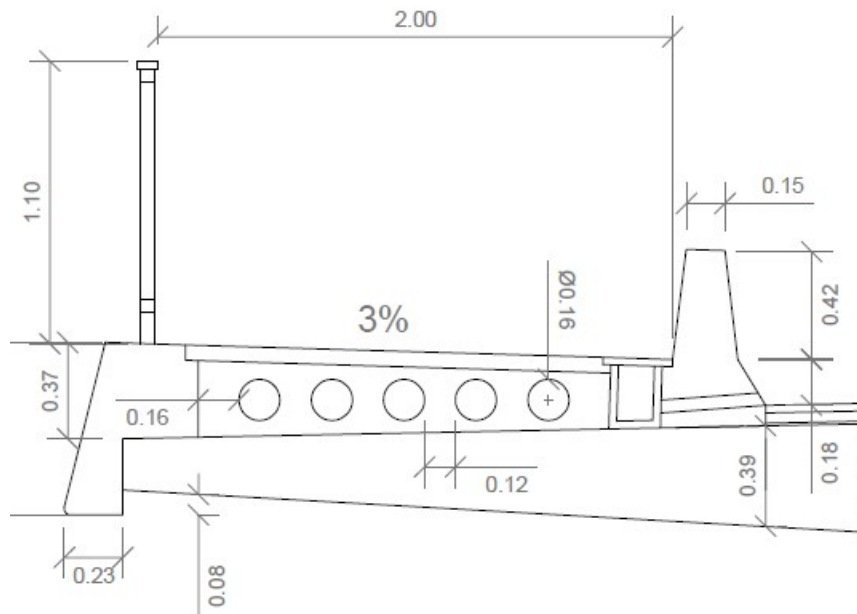


Figure 4.6: Representation of edge details

Accordingly with Figure 4.5, the maximum width of the deck is 15.5 m divided into the 7.5-metre-long roadway, equally divided into 2 lanes, the docks of 1.5 meters, the sidewalks of 2.5 meters, safety barriers at both ends of the deck. The deck floor is reinforced with 8 cm thick paving and waterproofing.

The cantilever sides of the section are 3 meters long, to ensure that the depth is at least $1/7$ of its length: $h = v/7$, where v is the length of the cantilever. The depth of the ends must be between 15 and 20 cm, so a value of 20 cm has been chosen.

According to the standard, the solid concrete slab is composed of 8 lightening elements of 40 cm diameter each one. The spacing between the lightening elements is 45 cm, at the end 50 cm, and 20 cm both above and below, without taking into account the 2% slope.

4.4 Edge details

On the cantilever parts of the deck, there are 2.5 meters of sidewalk, in particular 2 meters are used for the circulation of people. The safety railings are added at both ends of the cantilevers. According to the standard, the railings have a minimum height of 1 meter, so a height of 1.1 meters has been chosen. The spacing between intermediate vertical bars

is 0.18 meters. In order to provide the electricity supply of the bridge, pipes are located under the pavement. There are 5 tubes of 0.16 meters diameter, spaced between them 0.12, and 0.16 from the edges. A sewage system with a slope of 3% has been designed as well, in order to carry the water to the pipes. Figure 4.6 shows the edge details.

4.5 Abutments

In this case, open-type abutments on both sides have been chosen. This is due to a question of luminosity and aesthetics.

In the abutment, a distance of 80 cm has been left from the embankment. In addition, a transition slab at the end of the abutment is present. It allows a smooth transition of the pavement when a settlement of the embankment occurs. For this reason, the appearance of a step between the bridge structure and the earth embankment can be avoided. This transition slab is approximately 5 meters long, 20 centimeters thick and have a 10% slope. The slab is cast over the compacted soil. In the preliminary design of the abutment supports, a height of 15 cm has been chosen, whereas in the case of the central support on the pile, a height of 20 cm.

The retaining wall of the abutment is hidden within the embankment. It has a regular geometry with a thickness of 1 m in each column. Moreover, the choice of a rigid foundation completes the lowest part of the structure, assuming that the soil has good mechanical characteristics. The depth of the abutment in the transverse direction of the bridge is as wide as that of the bridge deck.

A support surface inclined towards the guard wall with a 5% slope is designed as water evacuation element. The water is collected and discharged to the back of the abutment by means of drainage pipes.

4.6 Pier

4.6.1 Geometry

The choice of the pier geometry is based mainly on the architectural and structural aspect, because it is a low bridge (minimum gauge = 5.30 m). The goal is to find a shape that is attractive and combines well with the typology of the deck. The cross section of the pier changes with the height.

The designed pile has two different shapes. It is trapezoidal in the elevation with major base at the top and Y-shaped in the transverse section, wherein each arm has a support device. This shape has been chosen in order to be harmonic.

Additionally, from a structural point of view, the base area (1.70 m^2) has been chosen to stay correctly on the foundation. Thus, a rectangular shape (1.00 x 1.70 m) has been

chosen with the longest side in the direction of the cross section.

The height of the pier is 6.70 m. The bifurcation of the Y-shaped arms allows to increase the distance between the supports of the deck in order to have greater stability. The type of pier foundation has been chosen as a rigid spread footing measuring (5x5) m. Especially, it is assumed that the soil has good mechanical characteristics already close to the surface. Thus, Figure 4.7 provides an overview of the pier geometry.

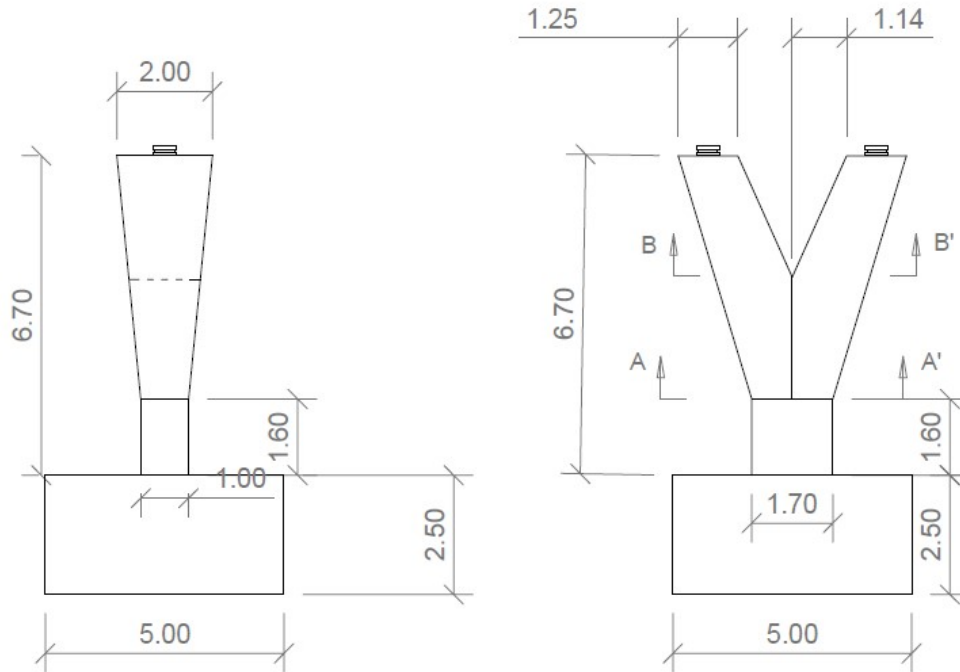


Figure 4.7: Pier geometry

4.6.2 Preliminary design

An approximate computation of the loads applied to the pier is proposed here to verify its dimensions. Regarding the preliminary design of the pier, a higher load hypothesis has been performed. Thereby, the following loads have been considered:

- Concrete specific weight: 25 kN/m^3
- Uniform live load: 9 kN/m^2 over the entire length of the bridge
- Concentrated load: 600 kN in the span center

The cross-section area has been computed as shown in Eq. (4.3). This solution regards the most feasible and conservative computation in the preliminary design of the base.

$$A_{centralsection} = 15.31 \text{ m}^2 \quad (4.1)$$

$$A_{lightenings} = n \cdot \pi \cdot \left(\frac{d}{2}\right)^2 = 8 \cdot \pi \cdot \left(\frac{0.4}{2}\right)^2 = 1.01 \text{ m}^2 \quad (4.2)$$

$$A_{real} = 15.31 - 1.01 = 14.30 \text{ m}^2 \quad (4.3)$$

In this way, it is possible to compute the reaction of the central support. In particular, the reaction represents the force applied to the pier of the bridge examined as a continuous 2-span beam. Figure 4.8 represents the continuous beam with the two uniform loads applied.

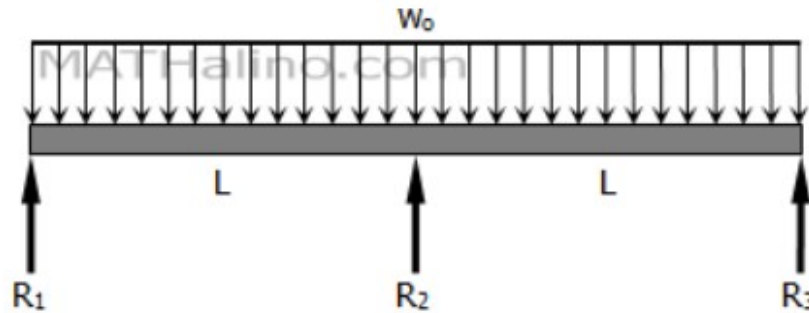


Figure 4.8: 2-span beam with uniform load

In this case, the values of the uniform loads are listed as follows:

- Load due to the bridge dead weight:

$$A_{real} \cdot deadweight = 14.31 \cdot 25 = 357.5 \text{ kN/m} \quad (4.4)$$

- Overload due to vehicle traffic:

$$Overload \cdot lanewidth \cdot n \text{ lanes} = 9 \cdot 3 \cdot 2 = 54 \text{ kN/m} \quad (4.5)$$

- Total uniform load:

$$W_o = 357.5 + 54 = 411.5 \text{ kN/m} \quad (4.6)$$

Thus, the reaction is equal to:

$$R_{2_{W_o}} = \frac{5W_oL}{4} = \frac{5 \cdot 411.5 \cdot 31.36}{4} = 16130.8 \text{ kN} \quad (4.7)$$

Figure 4.9 presents the second typology regarding the concentrated load applied in the span center.

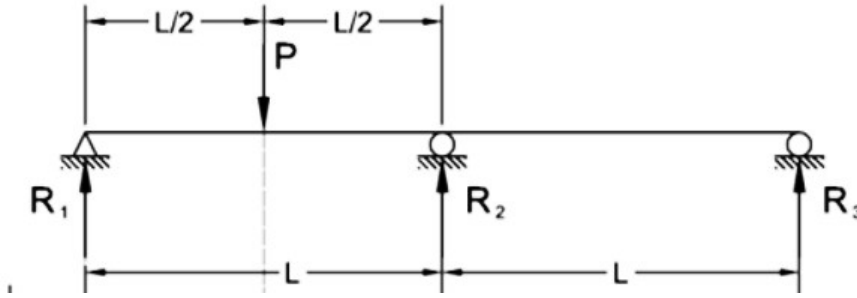


Figure 4.9: 2-span beam with concentrated load

In the case of concentrated load in the span center, Eq. (4.8) accounts for the vertical reaction, as follows:

$$R_{2_P} = \frac{F \cdot \left(\frac{L}{2}\right)}{2L^3} \left(3L^2 - \left(\frac{L}{2}\right)^2\right) = 412.5 \text{ kN} \quad (4.8)$$

Finally, the total reaction of the pier can be computed as follows:

$$R_{2,tot} = R_{2_{W_o}} + R_{2_P} = 16130.8 + 412.5 = 16543.3 \text{ kN} \quad (4.9)$$

Once this value is found, it can be assumed that the characteristic compressive strength of concrete is quite low, $\sigma = 10 \text{ MPa}$. This assumption depends on the application of the bending moment due to wind load and braking force that is neglected here. Thus, an area of the pier base is found as follows:

$$A_{\text{pier}} = \frac{R_{2,tot}}{\sigma} = \frac{16543.3 \text{ kN}}{10^4 \text{ kPa}} = 1.65 \text{ m}^2 \quad (4.10)$$

Eq. (4.10) describes that the preliminary design is structurally acceptable. Indeed, the value of the pier area chosen in the design is more conservative.

4.7 Bridge modelling on SAP2000

A FEM (finite element model) of the bridge has been obtained by means of the software *SAP2000*. This method is useful to analyse the bridge affected by all loads combination. Among the others, seismic action is the most interesting for the present work. In the beginning, the 2-span bridge has been modelled as a simple-supported beam. Each span has been divided into six different sections in order to obtain a more accurate discretization. The deck consists of an irregular, curved and variable thickness that varies increasing from the abutment to the pier. For this reason, an irregular beam section has been assigned in the model. In the six sections of the deck each mechanical and geometrical property, such as area, moment of inertia, torsional stiffness, and material has been computed (Table 4.2-3). The class of concrete is C40/50, thus, the real model of the bridge deck has been obtained.

Afterwards, the model has been improved with the pier addition that has a Y-shape. Thus, the pier has been modelled by dividing the sections of the Y arms into four parts and the vertical shaft into seven parts. All the modelled sections are rectangular according to the dimensions of variable pier geometry. A frame element has been adopted for the sections modelling, thereby the related shape function is a spline curve. Figure 4.10 shows the 3D pier modelling.

The connection between the pier and the deck has been obtained by means of very stiff bars placed from the gravity center of the deck to the beginning of the pier. These bars have null mass but the stiffness is ten times bigger than the other sections of the deck. In particular, the bars are connected to each arm of the pier with a neoprene device that is detailed at the end of this chapter.

All the sections properties which constitute the bridge modelling are reported in Table 4.2-3.

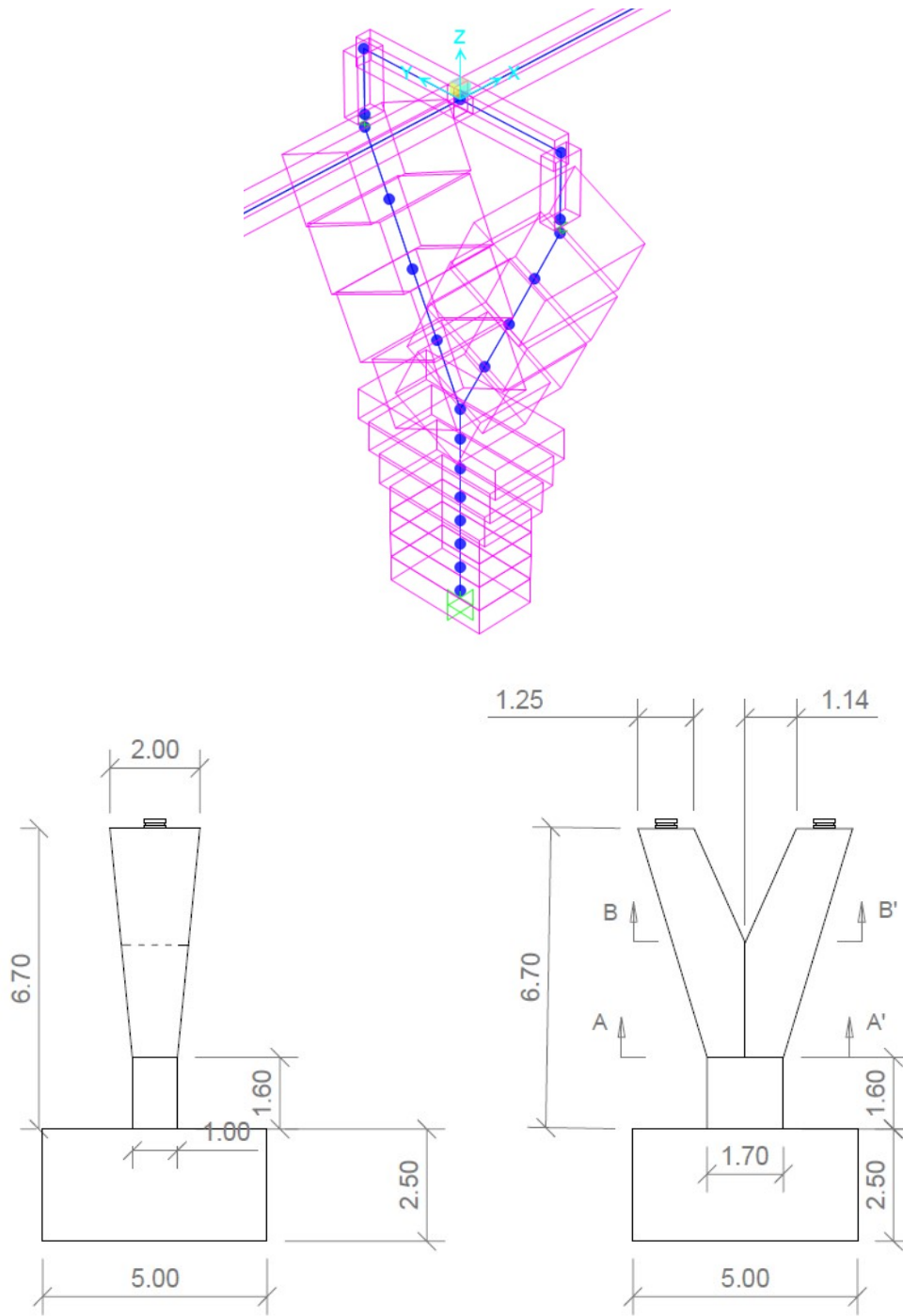


Figure 4.10: 3D pier modelling on SAP2000

Table 4.2: Frame section properties part 1 of 2

Section Name	Material	Shape	t3	t2
			[m]	[m]
shaft pier 1	C40/50	Rectangular	1,29	2,59
shaft pier 2	C40/50	Rectangular	1,19	2,29
shaft pier 3	C40/50	Rectangular	1,1	2
shaft pier 4	C40/50	Rectangular	1	1,7
arm pier 1	C40/50	Rectangular	1,38	1,82
arm pier 2	C40/50	Rectangular	1,52	1,64
arm pier 3	C40/50	Rectangular	1,56	1,46
arm pier 4	C40/50	Rectangular	1,29	1,29
section 1	C40/50	General	0,4572	0,254
section 2	C40/50	General	0,4572	0,254
section 3	C40/50	General	0,4572	0,254
section 4	C40/50	General	0,4572	0,254
section 5	C40/50	General	0,4572	0,254
section 6	C40/50	General	0,4572	0,254

Table 4.3: Frame section properties part 2 of 2

Section Name	Area	Torsional Constant	I33	I22
	[m ²]	[m ⁴]	[m ⁴]	[m ⁴]
shaft pier 1	3,3411	1,274752	0,463327	1,867703
shaft pier 2	2,7251	0,867776	0,321585	1,190891
shaft pier 3	2,2	0,582217	0,221833	0,733333
shaft pier 4	1,7	0,358762	0,141667	0,409417
arm pier 1	2,5116	0,853727	0,398591	0,693285
arm pier 2	2,4928	0,86775	0,479947	0,55872
arm pier 3	2,2776	0,725134	0,461897	0,404578
arm pier 4	1,6641	0,39	0,230769	0,230769
section 1	7,69	0,48	0,89	2,4
section 2	8,21	0,59	1,11	3,12
section 3	9,03	0,76	1,49	3,92
section 4	10,12	1	3	4,38
section 5	11,59	1,36	5,14	6,87
section 6	13,45	1,81	8,44	10,25

Finally, the undeformed bridge shape is shown in Figure 4.11. A rigid spread footing has been assumed as a possible foundation, so in the abutments and pier supports the built-in restraints have been chosen.

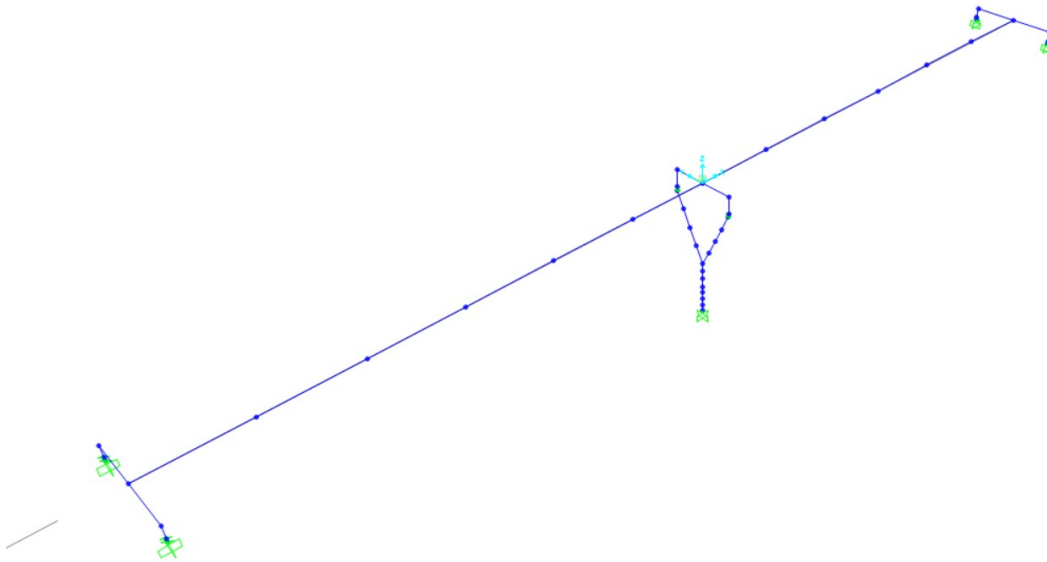


Figure 4.11: Undeformed shape of the bridge

4.8 Loads definition

Loads definition has been performed according to the standard IAP11, that includes vertical, longitudinal and transverse actions. Specifically, it takes into account the evolution of the vehicles loads in the future during the whole bridge service life, that is estimated as one hundred years.

Vertical actions are listed as follows:

- Dead load
- Non-structural permanent load
- Live load
- Vehicles load
- Seismic force
- Thermal vertical variations
- Snow
- Wind

Longitudinal actions are:

- Seismic force
- Braking force
- Lineal deformations: prestressing, creep, shrinkage, temperature

Lineal deformations are all the imposed ones that can occur in a PC structure. In this analysis, a bridge fixed point has been chosen to compute all the displacements due to these deformations. It appears very clearly that the fixed point is placed in the middle, because of symmetry. Therefore, this suggests that it is possible to measure the displacements only in the abutments and not in the pier. This hypothesis is due to the assumption of a couple of multi-directional neoprene bearings used as devices supports. This topic is discussed better in the next chapters.

Obviously, linear deformations are only one of the many factors that contribute to the displacement of the pier, as a consequence of the presence of vertical, longitudinal and transverse actions.

Table 4.4 summarizes the deformation values considered, with the total final value. This has

been computed by increasing the results with the appropriate coefficient and considering the most unfavorable combination of actions.

Table 4.4: Values of the lineal deformations

Action	Deformation	Value
Prestressing	ε_p	$-100 \cdot 10^{-6}$
Creep	ε_{cr}	$-2,40 \cdot 10^{-4}$
Shrinkage	ε_c	$-300 \cdot 10^{-6}$
Temperature, expansion	$\varepsilon_{t,exp}$	$3,50 \cdot 10^{-4}$
Temperature, contraction	$\varepsilon_{t,con}$	$-1,97 \cdot 10^{-4}$
Total deformation	$1,5 \cdot (\varepsilon_p + \varepsilon_{cr} + \varepsilon_c + \varepsilon_{t,con})$	$-1,26 \cdot 10^{-3}$

Consequently, calculating the displacement of the abutments of the bridge is immediately simple. It is equal to the value of the total deformation multiplied by the relative distance between the two points. In this case, it is equivalent to the span of the bridge (27.75 m), as follows:

$$u_{x,abutment} = \varepsilon_{tot} \cdot L_{span} = 0.035 \text{ m} \quad (4.11)$$

Finally, to complete the list of applied actions, transverse forces are listed below:

- Seismic force
- Wind

4.9 Seismic analysis

Earthquake is the main *character* among all the actions applied to the bridge, in particular in the longitudinal direction. Basically, it depends on the zone where the bridge is placed. Thus, there are sites where seismic force is low and other zones where earthquake action is strong. This is evident in the present case study.

The bridge is located in Sicily, the largest island in Southern Italy. In particular, a site close to the Strait of Messina has been selected with a high seismic hazard. Accordingly, with the current Italian standard for constructions, it belongs to the first seismic category among four. Indeed, a strong earthquake destroyed all the city in 1908.

Seismic analysis is performed according to the actions related to SLV (Life-saving limit state), that belongs to ULS (ultimate limit state). When the earthquake occurs, the construction undergoes breakages and collapses of non-structural and plant components and significant damage to structural components, which is associated with a significant loss of stiffness regarding horizontal actions. The construction instead retains a part of the strength and stiffness for vertical actions and a margin of safety compared to the collapse for horizontal seismic actions.

Seismic analysis follows the Italian standard, NTC2018 [37], and also the European standard, EN 1998-2 Eurocode 8 [38]. Accordingly with NTC2018 (§ 7.3.6.1), it must be verified that the individual structural elements and the whole structure have sufficient strength capacity to satisfy the demand for the SLV (Life-saving limit state).

The standards specify that the proportions of the structure must be such as to permit the plastic involvement of the pier. The inelastic dissipative behaviour must be regarding the flexural type, with the exclusion of possible mechanisms of shear failure, because this failure is very brittle and thus, ductility would not be fulfilled. For this reason, the “capacity design” criterion is used [37].

Therefore, an adequate behaviour factor, q , is chosen according to the table of the standard, Eurocode 8. In this case, a ductile category is chosen to ensure structure ductility in order to prevent the earthquake actions. The correct choice for the present case study is shown in Figure 4.12: “Vertical piers in bending”. For this reason, taking into account that $\lambda(\alpha) = 1$, a value of $q_0 = 3.5$ is obtained.

Actually, for reinforced concrete ductile members the value of q -factors is valid when the normalized axial force ν_k does not exceed 0.30, i.e. the axially applied load divided by the resistant concrete area.

If $0.30 < \nu_k \leq 0.60$ even in a single ductile member, the value of the behaviour factor must be reduced, as follows:

$$q_r(\nu_k = 0.4) = q_0 - \frac{\nu_k - 0.3}{0.3}(q_0 - 1) = 2.7 \quad (4.12)$$

It is necessary here to clarify exactly what is meant by q . The behaviour factor is used in seismic design to reduce the full elastic seismic demand on structures since well-designed structures can dissipate energy through inelastic response. Its principle is based especially on the presence of ductility of the structure. The value of the behaviour factor computed above is referred to the horizontal directions (x and y) of the earthquake. On the other hand, the standard suggests to use a value equal to 1 regarding the vertical way (z).

Table 4.5-6 provides a summary of all introduced parameters, geotechnical input data found in the soil report as well: category of subsoil and topographic typology.

As can be seen from Figure 4.13, the red curve represents the horizontal elastic response spectrum, the blue one the vertical response spectrum and the black one accounts for the horizontal design spectrum.

Type of Ductile Members	Seismic Behaviour	
	Limited Ductile	Ductile
Reinforced concrete piers:		
Vertical piers in bending	1,5	3,5 $\lambda(\alpha_s)$
Inclined struts in bending	1,2	2,1 $\lambda(\alpha_s)$
Steel Piers:		
Vertical piers in bending	1,5	3,5
Inclined struts in bending	1,2	2,0
Piers with normal bracing	1,5	2,5
Piers with eccentric bracing	-	3,5
Abutments rigidly connected to the deck:		
In general	1,5	1,5
Locked-in structures (see. 4.1.6(9), (10))	1,0	1,0
Arches	1,2	2,0
<p>* $\alpha_s = L_s/h$ is the shear span ratio of the pier, where L_s is the distance from the plastic hinge to the point of zero moment and h is the depth of the cross-section in the direction of flexure of the plastic hinge.</p> <p>For $\alpha_s \geq 3$ $\lambda(\alpha_s) = 1,0$</p> <p>$3 > \alpha_s \geq 1,0$ $\lambda(\alpha_s) = \sqrt{\frac{\alpha_s}{3}}$</p>		

Figure 4.12: Maximum values of the behaviour factor q

The term “response spectrum” refers to a plot of the peak or steady-state response (displacement, velocity or acceleration) of a series of oscillators of varying period, that are forced into motion by the same base vibration or shock. The resulting plot can then be used to pick off the response of any linear system, given its natural frequency of oscillation. As a result, modal analysis is performed to identify the modes, and the response in that mode can be picked from the response spectrum. These peak responses are then combined to estimate a total response. A typical combination method is the square root of the sum of the squares (SRSS) if the modal frequencies are not close. By contrast, the complete quadratic combination (CQC) is used, as an improvement on SRSS.

Response spectra can be defined as useful tools regarding earthquake engineering for analysing the performance of structures during an earthquake. In seismic regions, this method forms the basis for computing the forces that a structure must resist. Significant seismic damage may occur if the building response is “in tune” with the components of the ground motion (resonance), which may be identified from the response spectrum.

The response spectra related to the Messina Earthquake can be seen more clearly in the

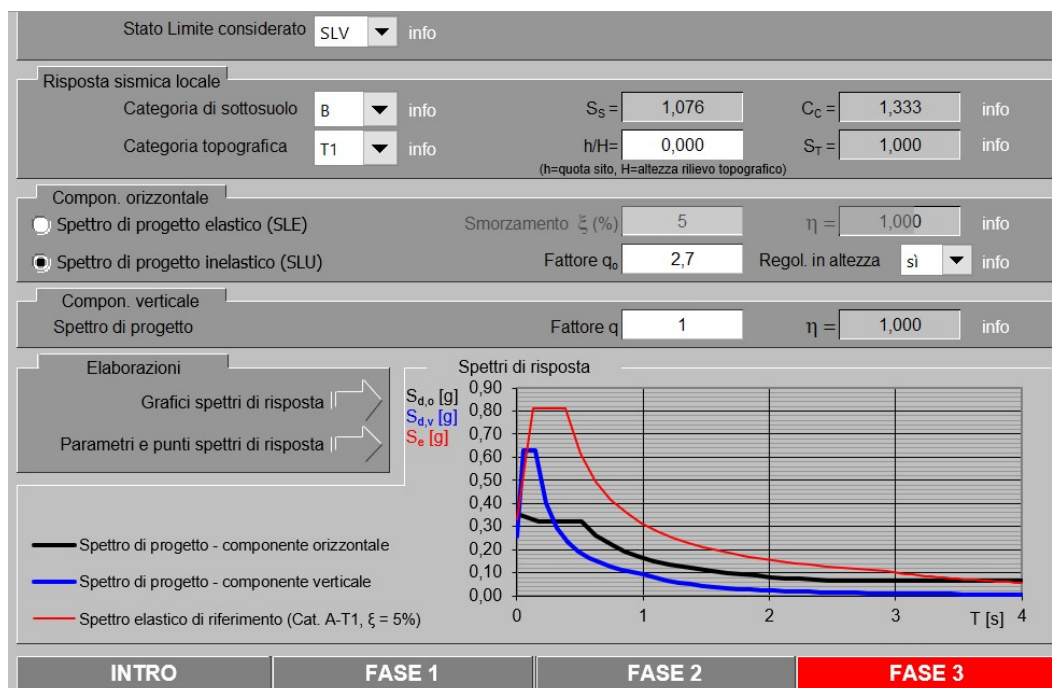


Figure 4.13: Response spectra obtained by an *Excel spreadsheet*

graph in Figure 4.14, which shows the horizontal acceleration component in black, and the vertical one in blue. The period (T) and the response acceleration as a fraction of the gravitational acceleration ($S_d[g]$) are plotted respectively on the x and y-axis. The response spectra have been obtained by means of an Excel spreadsheet guided by the Italian NTC2018 regulation [37]. In particular, some important parameters can be highlighted in Table 4.5-6.

As can be seen from Table 4.5-6, the PGA values are quite high. Interestingly, this correlation is related to the first category of hazard among four included into the Italian standard. Consequently, this highlights the importance of an accurate seismic analysis. Peak ground acceleration (PGA) is the most important parameter and refers to the maximum ground acceleration that occurred during earthquake shaking at a location. PGA is equal to the amplitude of the largest absolute acceleration recorded on an accelerogram at a site during a particular earthquake. Earthquake shaking generally occurs in all the three directions. Therefore, PGA is often split into horizontal and vertical components. Horizontal PGA is generally larger compared to the vertical direction but this is not always true, especially close to large earthquakes.

PGA is a fundamental parameter (also known as an intensity measure) for earthquake en-

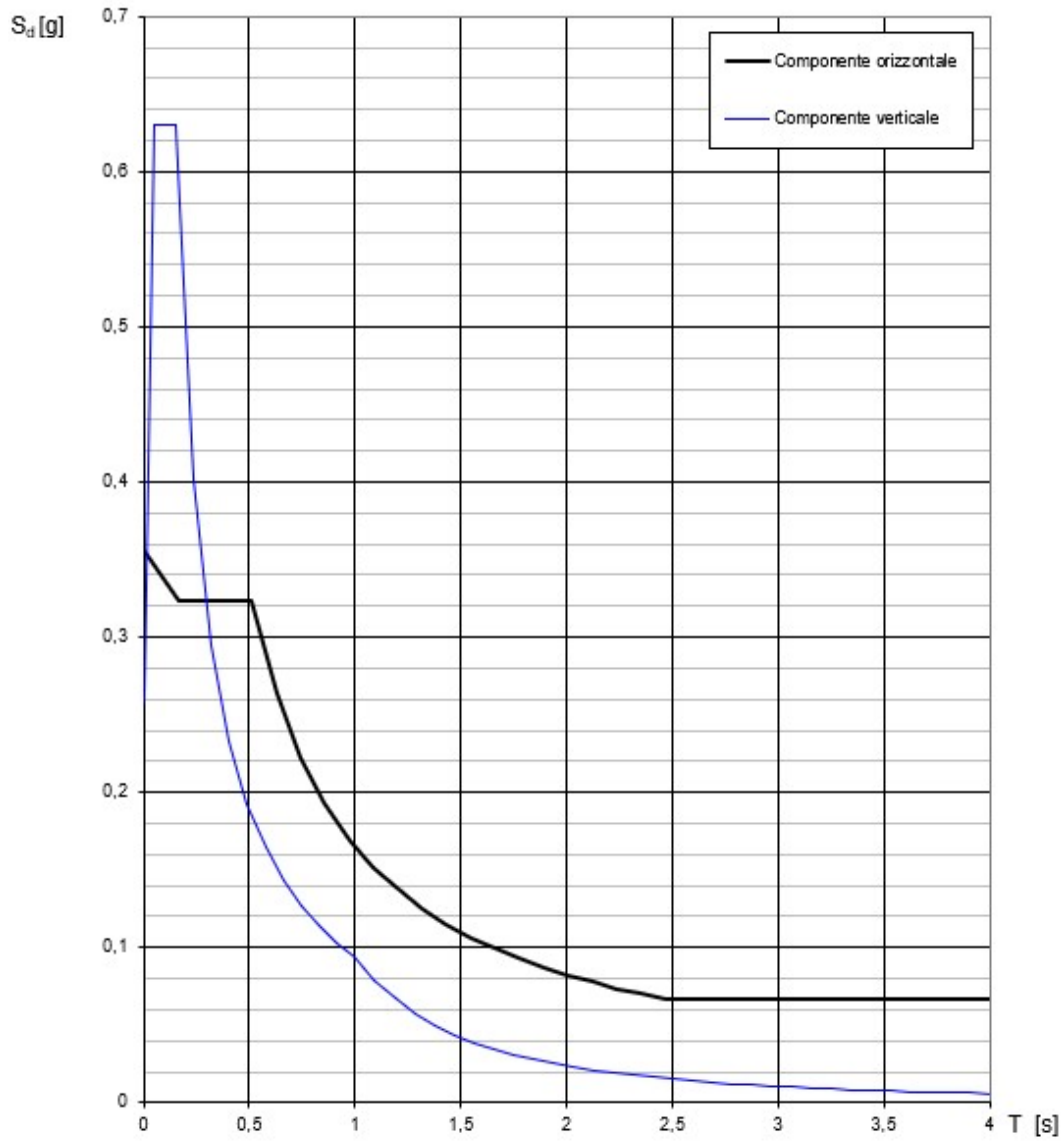


Figure 4.14: Horizontal and vertical components of the response spectra

Table 4.5: Horizontal component parameters

PGA	0.332 g
S	1.076
η	0.370
T_B	0.170 s
T_C	0.511 s
T_D	2.927 s

Table 4.6: Vertical component parameters

PGA_v	0.258 g
S	1.0
η	1.0
T_B	0.050 s
T_C	0.150 s
T_D	1.000 s

gineering. Moreover, the peak horizontal acceleration (PHA) is the most commonly used type of ground acceleration in engineering applications. It is used within earthquake engineering (including seismic building standards, as NTC18 or Eurocode 8) and it is commonly plotted on seismic hazard maps. In an earthquake, damage to buildings and infrastructure is closely related to ground motion, expressed by the PGA value. It is measured by instruments, such as accelerographs.

Figure 4.15 illustrates a European PGA map that shows where the seismic hazard is stronger. This is evident in the case of Messina where the bridge is set. Indeed, the PGA value is high compared to the whole of Europe.

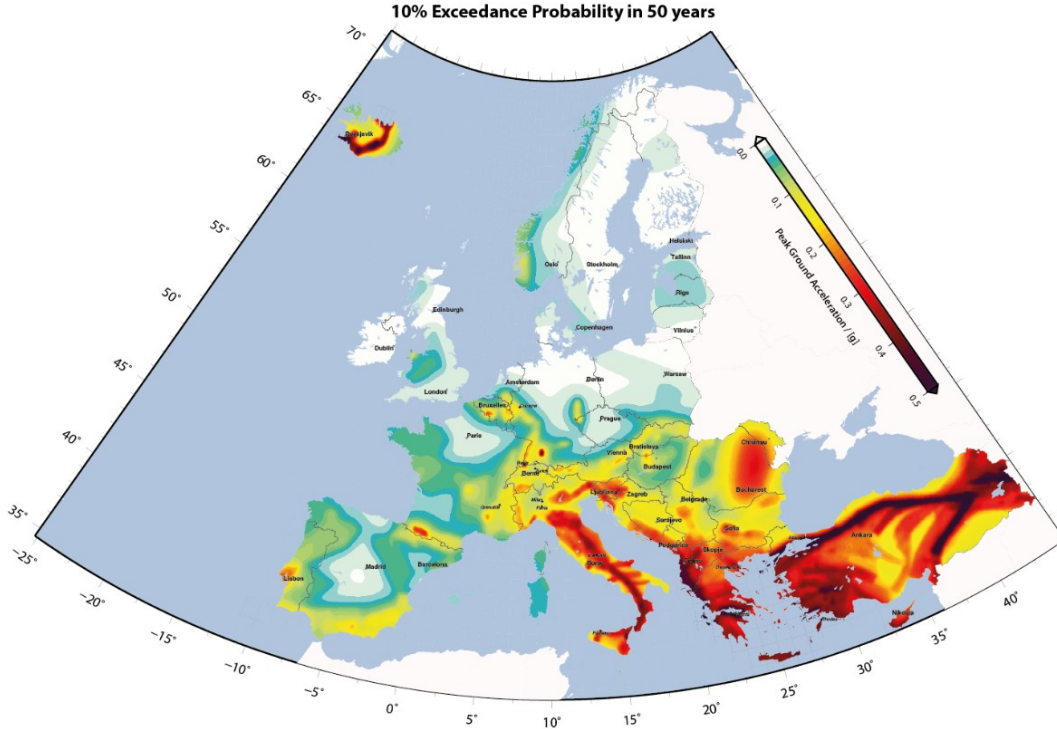


Figure 4.15: European PGA map

4.9.1 Earthquake application in the software

Once the earthquake parameters are known, they can be inserted into the software SAP2000 as the typology of the “response spectrum” load. Accordingly, they can be combined as the standard suggests, as follows:

$$E_{xd} + 0.3E_{yd} + 0.3E_{zd} \quad (4.13)$$

$$0.3E_{xd} + E_{yd} + 0.3E_{zd} \quad (4.14)$$

$$0.3E_{xd} + 0.3E_{yd} + E_{zd} \quad (4.15)$$

This combination depends on the presence of the earthquake at the same time in all the directions with different percentages. In the model analysis, the worst combination that can damage the bridge is reported in Eq. (4.13), i.e. the situation in which the longitudinal

component (x) is greater.

4.9.2 Loads combination

Loads combination takes into account all loads with their own coefficients. In this case, this seismic combination is applied. Indeed, partial safety coefficients of all the loads are equal to 1 because an earthquake is considered such as a strong event, and thus it is not necessary to increase loads values.

Equation (4.16) accounts for the seismic combination:

$$E + G_1 + G_2 + P + \psi_{21} \cdot Q_{k1} + \psi_{22} \cdot Q_{k2} + \psi_{23} \cdot Q_{k3} + \dots \quad (4.16)$$

- E: seismic force
- G1: dead load
- G2: non-structural permanent load
- P: prestressing action
- Q_{kj} : variable loads (braking force, live load, vehicles, wind, snow,...)
- ψ_{kj} : coefficients values, reported in Figure 4.16

In this case study, all the variable loads (except the snow) have null coefficient, because of the presence of the earthquake. Thus, Table 4.7 summarizes the whole loads combination.

Table 4.7: Summary of the whole loads combination

Combo name	Case type	Case name	Scale factor unitless
seism x	Response Spectrum	Eq. x	1
seism x	Linear Static	Braking force	0
seism x	Response Spectrum	Eq. y	0,3
seism x	Response Spectrum	Eq. z	0,3
seism x	Linear Static	Live load	0
seism x	Linear Static	Wind	0
seism x	Linear Static	Snow	0,5
seism x	Linear Static	No-structural load	1
seism x	Linear Static	DEAD	1

Azioni	Gruppo di azioni (Tab. 5.1.IV)	Coefficiente Ψ_0 di combi- nazione	Coefficiente Ψ_1 (valori frequentanti)	Coefficiente Ψ_2 (valori quasi permanenti)
Azioni da traffico (Tab. 5.1.IV)	Schema 1 (carichi tandem)	0,75	0,75	0,0
	Schemi 1, 5 e 6 (carichi distribuiti)	0,40	0,40	0,0
	Schemi 3 e 4 (carichi concentrati)	0,40	0,40	0,0
	Schema 2	0,0	0,75	0,0
	2	0,0	0,0	0,0
	3	0,0	0,0	0,0
	4 (folla)	--	0,75	0,0
	5	0,0	0,0	0,0
Vento	a ponte scarico SLU e SLE	0,6	0,2	0,0
	in esecuzione	0,8	0,0	0,0
	a ponte carico SLU e SLE	0,6	0,0	0,0
Neve	SLU e SLE	0,0	0,0	0,0
	in esecuzione	0,8	0,6	0,5
Temperatura	SLU e SLE	0,6	0,6	0,5

Figure 4.16: Values of partial coefficients for bridges reported in NTC2018

4.10 SAP2000 outcomes

Software outcomes are extrapolated, when the loads combination has been defined. Here, the deformed shape of the bridge due only to dead load is shown in Figure 4.17. Obviously, central span displacements are accentuated in order to highlight the remaining smaller displacements in the bridge. The order of magnitude of displacements is the centimeter and the central span deflection is:

$$u_{central-span} = 4.7 \text{ cm}$$

Following seismic analysis and combination reported above, the deformed shape is obtained as shown in Figure 4.18. In this case, displacements are greater, especially in the longitudinal direction, as follows:

- $u_{x,abutment} = 6.74 \text{ cm}$
- $u_{x,pier} = 6.23 \text{ cm}$
- $u_{y,abutment} = 1.49 \text{ cm}$
- $u_{y,pier} = 1.89 \text{ cm}$
- $u_{central-span} = 5.11 \text{ cm}$

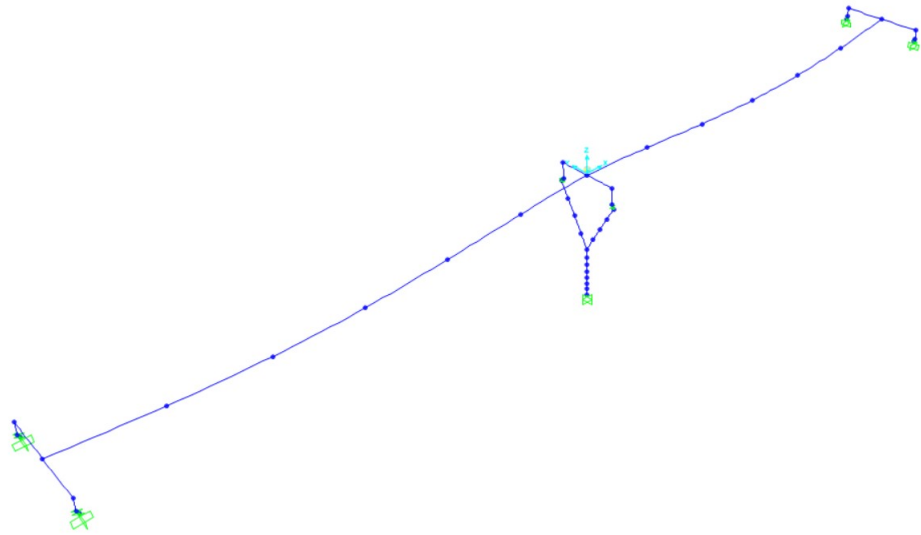


Figure 4.17: Deformed shape of the bridge due only to dead load

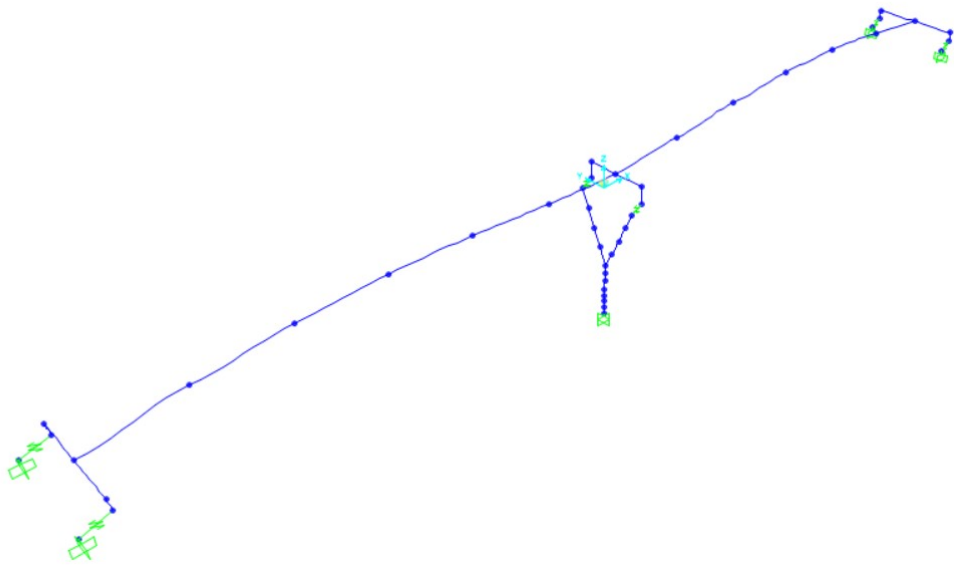


Figure 4.18: Deformed shape of the bridge due to the whole loads combination

4.10.1 Applied actions

In this bridge modelling, applied actions in the pier have been found as well. Additionally, axial force (N), bending moment in the x-direction (M_x), bending moment in the y-direction (M_y), shear force in both directions (V_x and V_y) have been highlighted in Figure 4.19-23. The maximum value of the axial force is at the base of the pier: $N=18380$ kN. In contrast,

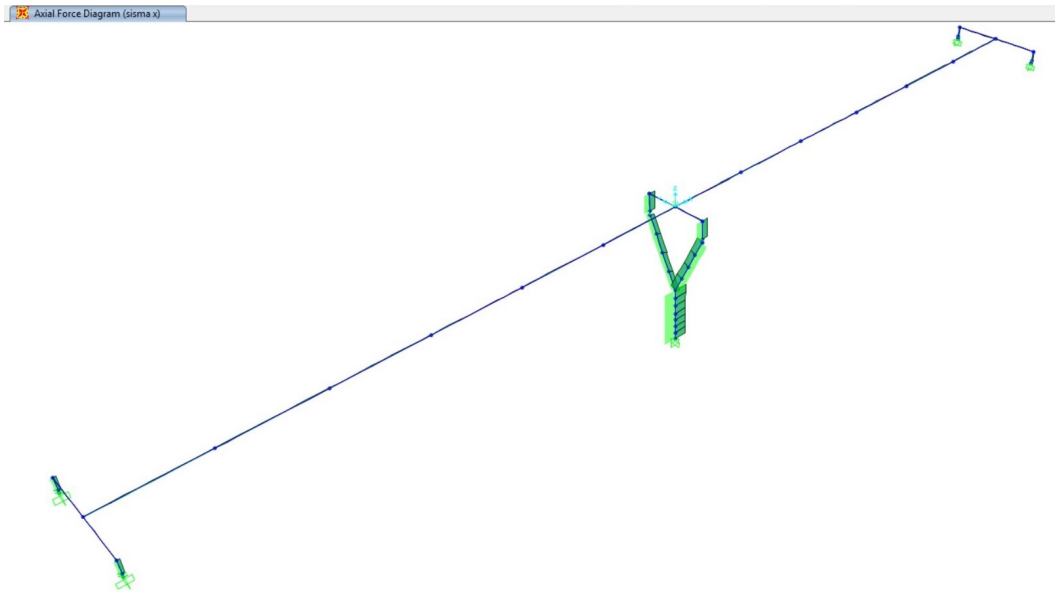


Figure 4.19: Axial force diagram

at the end of the vertical shaft, another smaller value has been found: $N=8322$ kN.

As can be seen from Figure 4.20, the biggest value of the bending moment in the x-direction is in the bridge deck. However, this analysis is focused only on the pier. Thus, even if it is not pretty clear, there is a bending moment in the pier as well:

- $M_{base} = 3710 \text{ kN} \cdot \text{m}$
- $M_{top} = 2833 \text{ kN} \cdot \text{m}$

As it is shown in Figure 4.21, the maximum value of the bending moment in the y-direction is at the end of the vertical shaft, where the Y-shape arms open: $M = 16494 \text{ kN} \cdot \text{m}$. Another interesting point is at the base of the pier in which $M = 9415 \text{ kN} \cdot \text{m}$.

The maximum value of the shear force in the y-direction is at the end of the vertical shaft, where the Y-shape arms open: $V=4138$ kN. By contrast, in the point at the base of the pier, shear force has been found as $V=1409$ kN (Fig. 4.22).

The biggest value of the shear force in the x-direction has been found in the bridge deck.

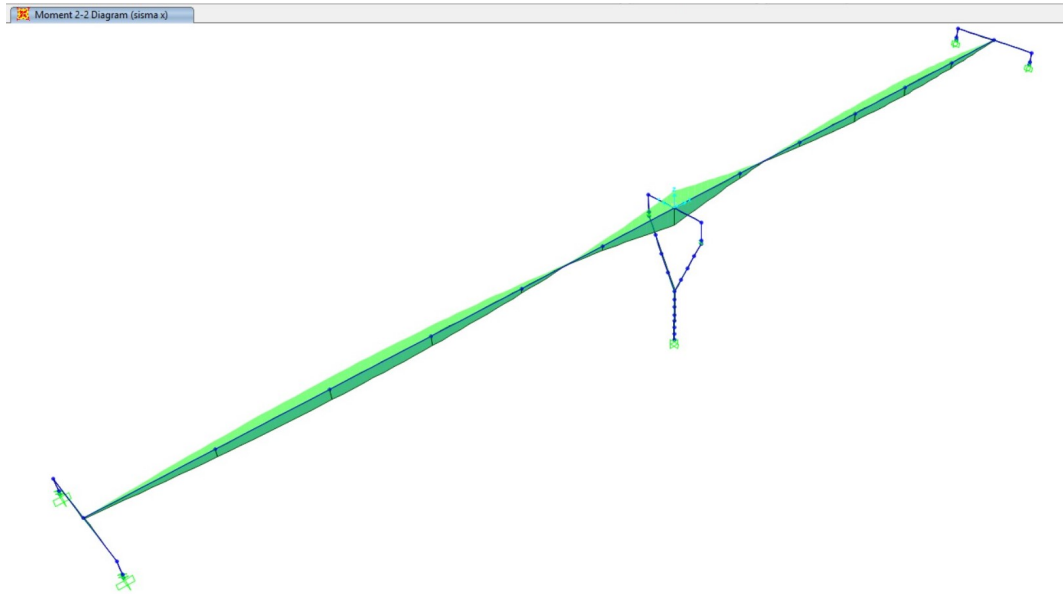


Figure 4.20: Bending moment diagram

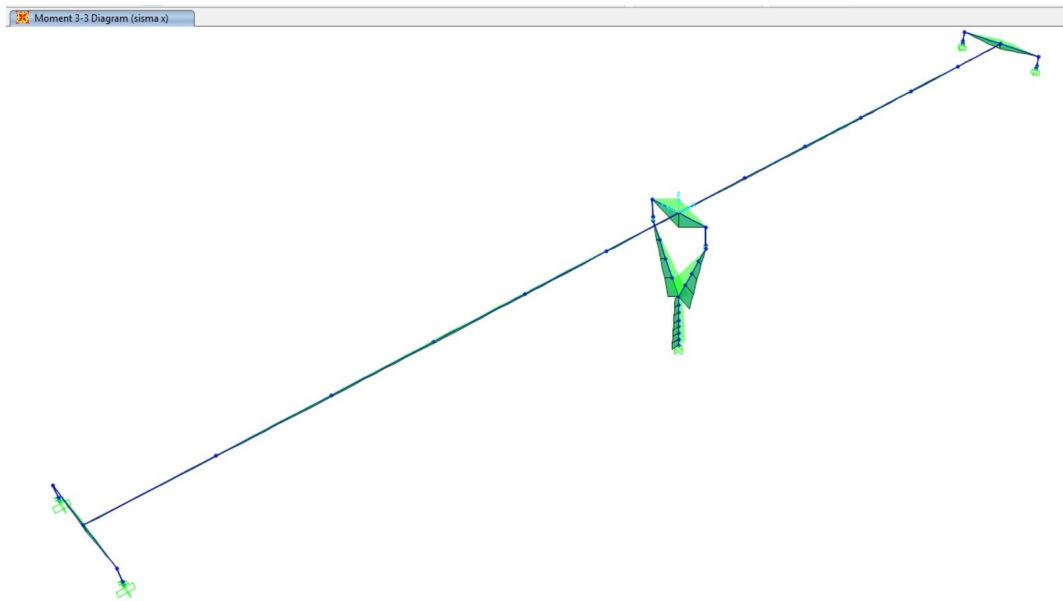


Figure 4.21: Bending moment diagram

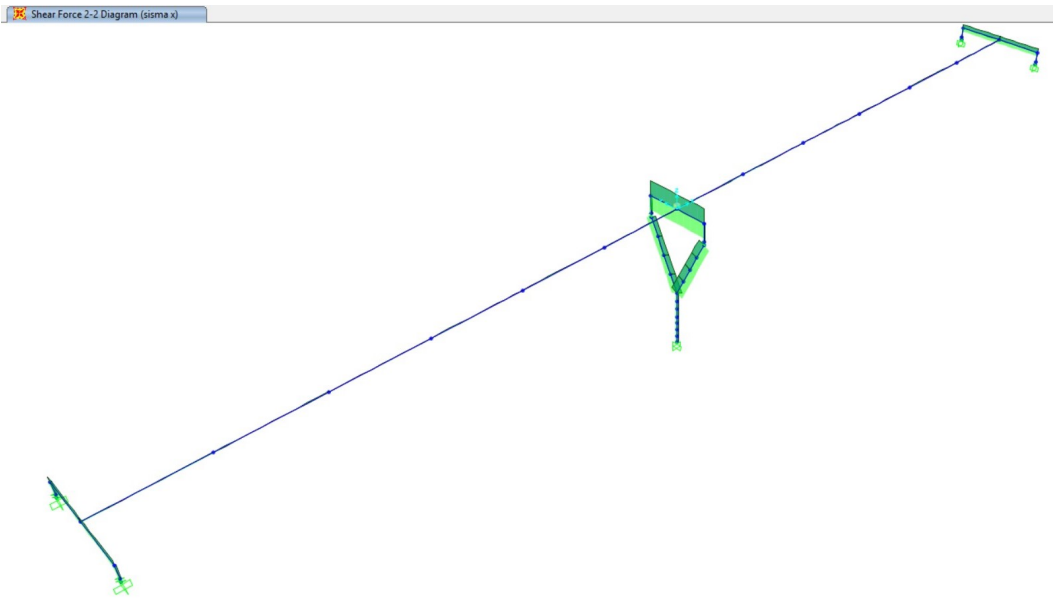


Figure 4.22: Shear force diagram

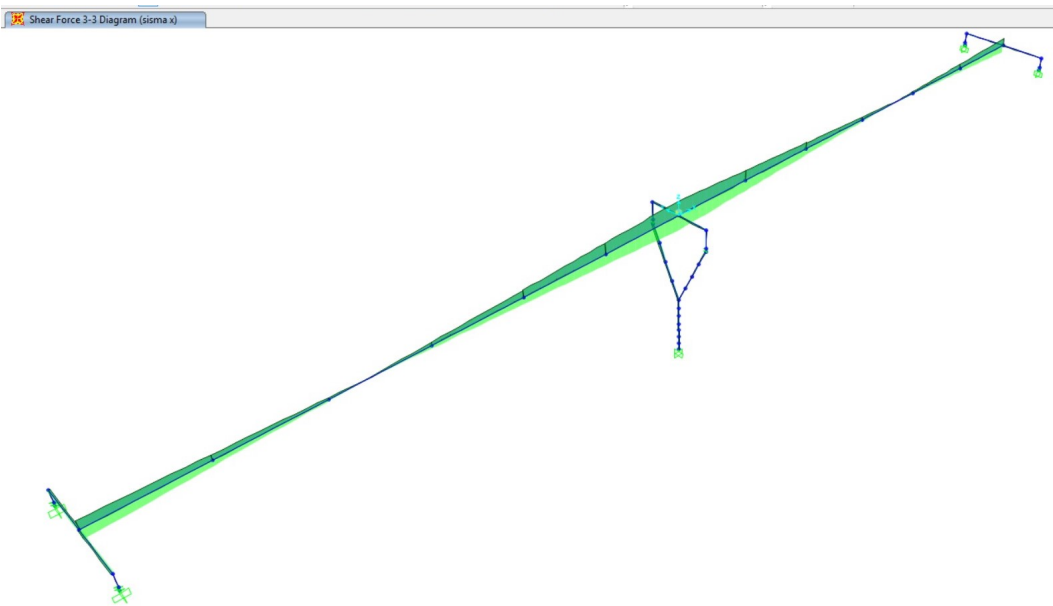


Figure 4.23: Shear force diagram

On the other hand, it is reminded that the analysis is focused only on the pier. So, even if it is not pretty clear, there is shear force in the pier as well, as shown in Figure 4.23:

- $V_{base} = 536 \text{ kN}$
- $V_{top} = 704 \text{ kN}$

4.11 Modal analysis

Modal analysis is an important aspect of bridge diagnostics. It studies the dynamic properties of systems in the frequency domain. It uses the overall mass and stiffness of a structure to find the various periods in which the structure naturally resonates. For this reason, modal analysis makes possible to show all vibration modes of the bridge. In earthquake engineering, knowing these periods of vibration is fundamental.

The goal of modal analysis in structural mechanics is to determine the natural mode shapes and frequencies of an object or structure, such as a bridge, during free vibration. It is common to use the finite element method (FEM) to perform this kind of analysis.

The types of equations which arise from modal analysis are those seen in eigensystems. The physical interpretation of the eigenvalues and eigenvectors, which come from solving the system, is that they represent the frequencies and corresponding mode shapes. Usually, the lowest frequencies determine the most prominent modes.

Table 4.9-15 list all the information relating to vibration periods, frequencies, modal load participation ratios, modal load participation mass ratios, modal participation factors.

Table 4.8: Modal Periods and Frequencies

Output Case	Step Type	Step Num	Period	Frequency	Circ Freq	Eigenvalue
			<i>Sec</i>	<i>Cyc/sec</i>	<i>rad/sec</i>	<i>rad²/sec²</i>
MODAL	Mode	1	1,515617	0,65979730	4,14562876	17,18623782
MODAL	Mode	2	1,505986	0,6640168	4,17214073	17,4067583
MODAL	Mode	3	1,175616	0,8506178	5,344589479	28,5646367
MODAL	Mode	4	0,617122	1,620426	10,18143739	103,661667
MODAL	Mode	5	0,450252	2,220978	13,95481967	194,736992
MODAL	Mode	6	0,41631	2,4020588	15,09258106	227,786003
MODAL	Mode	7	0,261858	3,8188673	23,99465132	575,7432919
MODAL	Mode	8	0,163314	6,1231694	38,47300804	1480,17234
MODAL	Mode	9	0,151221	6,6128473	41,54974547	1726,381349
MODAL	Mode	10	0,147093	6,7984053	42,71564061	1824,625953

Table 4.9: Modal Load Participation Ratios

Output Case	Item Type	Item	Static	Dynamic
			Percent	Percent
MODAL	Acceleration	UX	99,996	98,6465
MODAL	Acceleration	UY	99,9979	98,3096
MODAL	Acceleration	UZ	99,2739	78,1824

Table 4.10: Modal Participating Mass Ratios, Part
1 of 3

Output Case	Step Type	Step Num	Period	UX	UY	UZ	SumUX	SumUY
			Sec					
MODAL	Mode	1	1,515617	0,98643	0	0	0,98643	0
MODAL	Mode	2	1,505986	0	0,97757	0	0,98643	0,97757
MODAL	Mode	3	1,175616	0	0	0	0,98643	0,97757
MODAL	Mode	4	0,617122	1,09E-05	0	0	0,98644	0,97757
MODAL	Mode	5	0,450252	0	0,00518	0	0,98644	0,98276
MODAL	Mode	6	0,41631	0	0	0,74359	0,98644	0,98276
MODAL	Mode	7	0,261858	0	0	0	0,98644	0,98276
MODAL	Mode	8	0,163314	2,11E-05	4,944E-20	0	0,98647	0,98276
MODAL	Mode	9	0,151221	0	0	0,03824	0,98647	0,98276
MODAL	Mode	10	0,147093	0	0,00034	0	0,98647	0,9831

Table 4.11: Modal Participating Mass Ratios, Part
2 of 3

Output Case	Step Type	Step Num	SumUZ	RX	RY	RZ	SumRX	SumRY
MODAL	Mode	1	0	0	2,804E-05	0	0	2,804E-05
MODAL	Mode	2	0	0,01467	0	0	0,01467	2,804E-05
MODAL	Mode	3	0	0	0	0,9944	0,01467	2,804E-05
MODAL	Mode	4	0	0	0,58001	0	0,01467	0,58004
MODAL	Mode	5	0	0,00026	0	0	0,01494	0,58004
MODAL	Mode	6	0,74359	5,419E-20	1,304E-20	0	0,01494	0,58004
MODAL	Mode	7	0,74359	0	0	0,00546	0,01494	0,58004
MODAL	Mode	8	0,74359	5,675E-18	0,12761	0	0,01494	0,70765
MODAL	Mode	9	0,78182	0	0	0	0,01494	0,70765
MODAL	Mode	10	0,78182	6,516E-05	1,637E-19	0	0,015	0,70765

Table 4.12: Modal Participating Mass Ratios, Part
3 of 3

Output Case	Step Type	Step Num	SumRZ
MODAL	Mode	1	0
MODAL	Mode	2	0
MODAL	Mode	3	0,9944
MODAL	Mode	4	0,9944
MODAL	Mode	5	0,9944
MODAL	Mode	6	0,9944
MODAL	Mode	7	0,99986
MODAL	Mode	8	0,99986
MODAL	Mode	9	0,99986
MODAL	Mode	10	0,99986

Table 4.13: Modal Participation Factors, Part 1 of
2

Output Case	Step Type	Step Num	Period	UX	UY	UZ	RX	RY
			Sec	KN-m	KN-m	KN-m	KN-m	KN-m
MODAL	Mode	1	1,515617	-55,161955	-6,792E-10	-8,537E-10	-1,967E-09	-4,524897
MODAL	Mode	2	1,505986	-4,789E-11	-54,913639	-3,234E-11	3,987067	5,999E-09
MODAL	Mode	3	1,175616	-3,206E-10	2,736E-10	2,151E-10	6,839E-10	7,551E-08
MODAL	Mode	4	0,617122	-0,18339	7,786E-12	-4,66E-11	3,025E-11	650,796565
MODAL	Mode	5	0,450252	7,543E-11	3,998538	3,837E-09	-0,535009	5,764E-08
MODAL	Mode	6	0,41631	-2,056E-10	2,809E-09	-47,892957	7,662E-09	9,757E-08
MODAL	Mode	7	0,261858	3,054E-10	-7,625E-11	1,784E-09	-1,204E-10	-8,481E-08
MODAL	Mode	8	0,163314	0,255098	1,235E-08	2,86E-09	7,841E-08	305,258269
MODAL	Mode	9	0,151221	1,771E-09	1,613E-10	10,860485	2,31E-09	-8,215E-08
MODAL	Mode	10	0,147093	1,209E-09	1,024244	3,378E-09	0,265703	-3,458E-07

Table 4.14: Modal Participation Factors, Part 2 of
2

Output Case	Step Type	Step Num	RZ	Modal Mass	Modal Stiff
			KN-m	KN-m-s2	KN-m
MODAL	Mode	1	-1,668E-10	1	17,18624
MODAL	Mode	2	8,881E-10	1	17,40676
MODAL	Mode	3	851,564501	1	28,56464
MODAL	Mode	4	-5,972E-11	1	103,66167
MODAL	Mode	5	6,16E-10	1	194,73699
MODAL	Mode	6	1,207E-10	1	227,786
MODAL	Mode	7	63,084156	1	575,74329
MODAL	Mode	8	-4,781E-08	1	1480,17235
MODAL	Mode	9	-4,666E-08	1	1726,38135
MODAL	Mode	10	1,325E-08	1	1824,62595

Figure 4.24-33 show all ten vibration modes of the bridge. In blue, the deformed shape is depicted, by contrast in green there is the undeformed shape. Periods are expressed in seconds, frequencies in hertz.

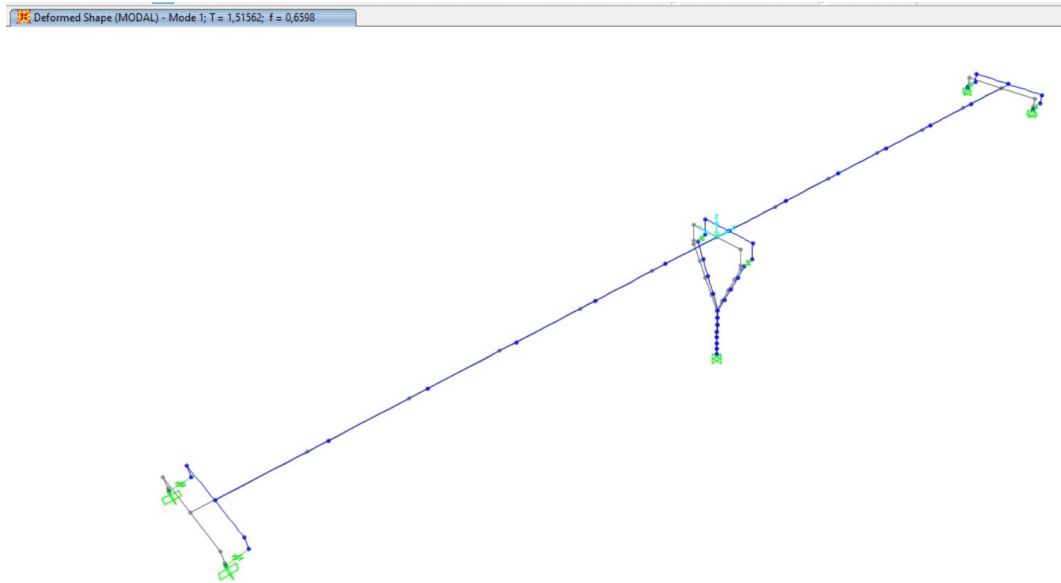


Figure 4.24: 1st vibration mode

The 1st mode depicts the longitudinal movement of the structure.

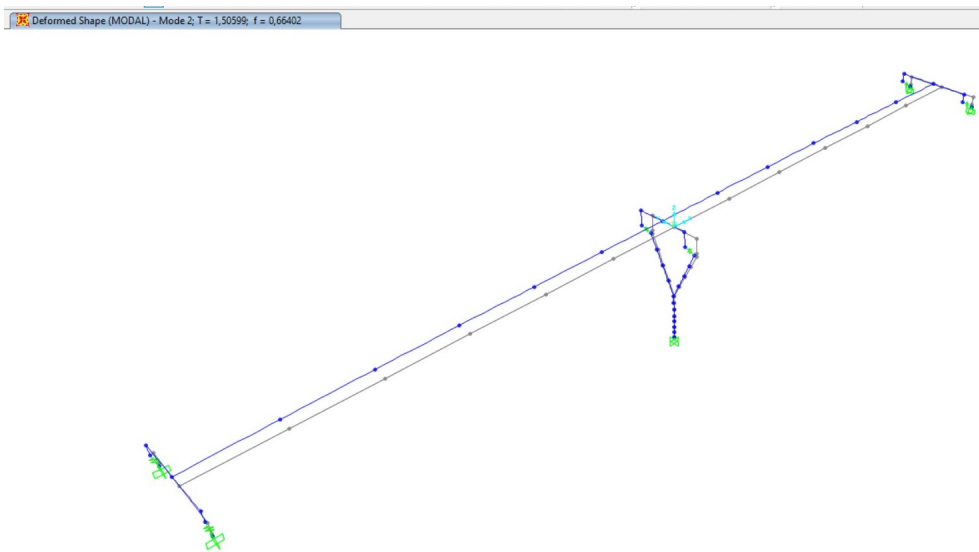
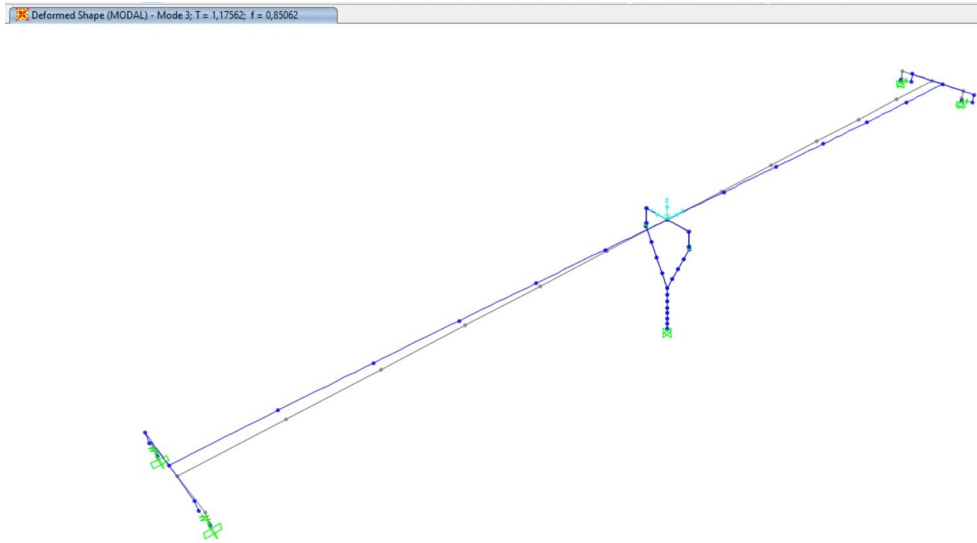
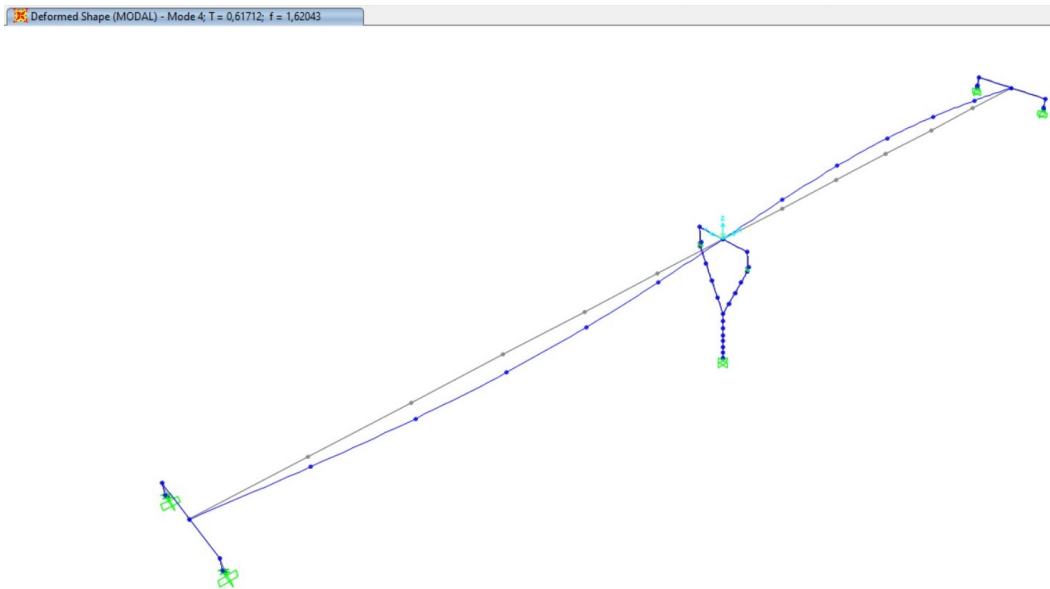


Figure 4.25: 2nd vibration mode

The 2nd mode represents the transverse movement of the structure.

Figure 4.26: 3rd vibration mode

The 3rd vibration mode accounts for the transverse and opposite movement of the abutments, on the contrary, the pier is almost stationary.

Figure 4.27: 4th vibration mode

The 4th mode shows the desynchronized longitudinal deflection of the deck.

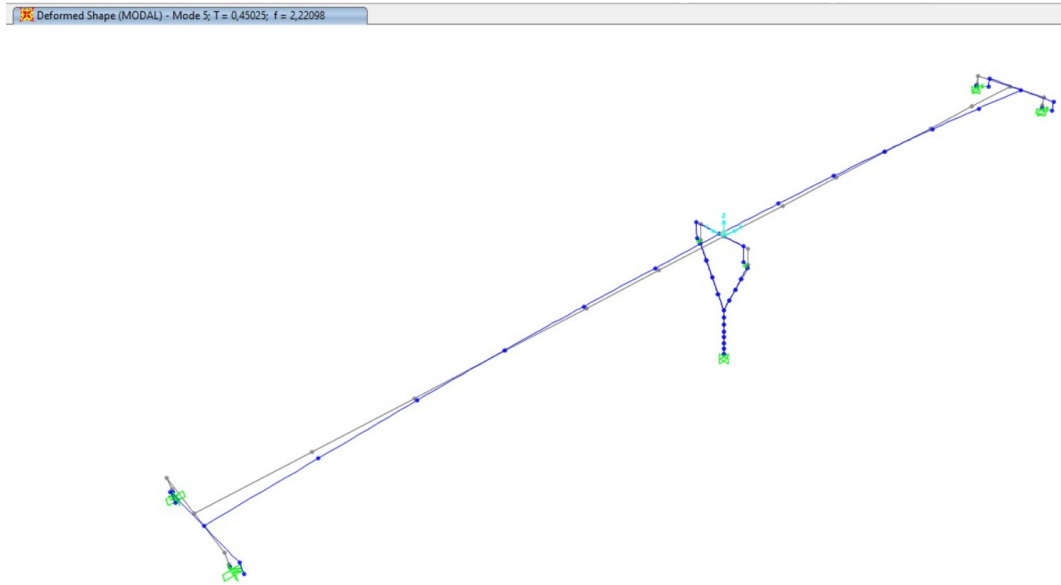


Figure 4.28: 5th vibration mode

The 5th vibration mode is a transverse undulatory motion.

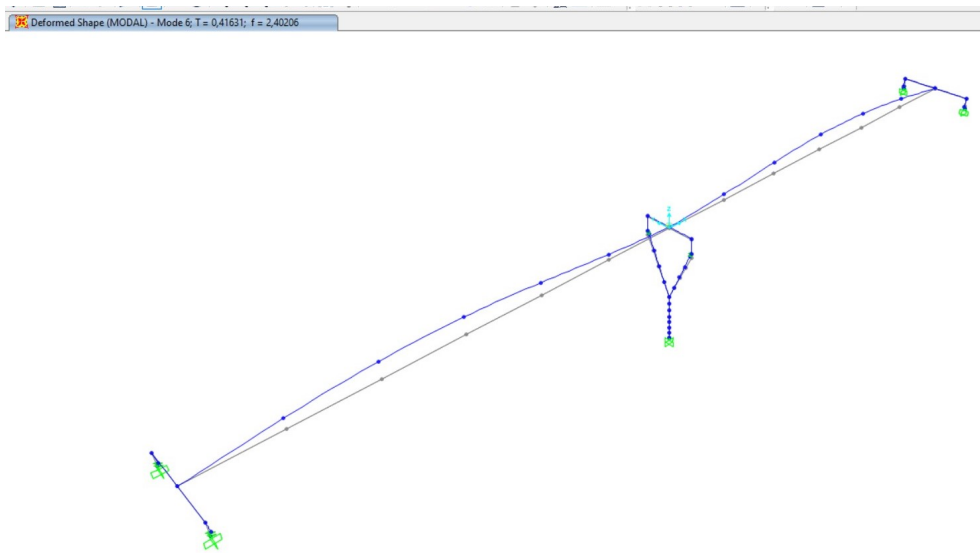
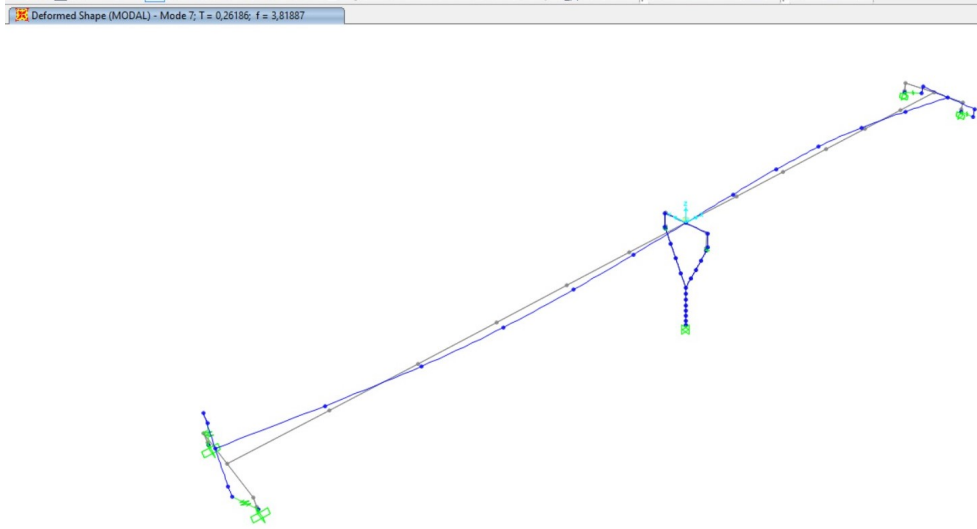
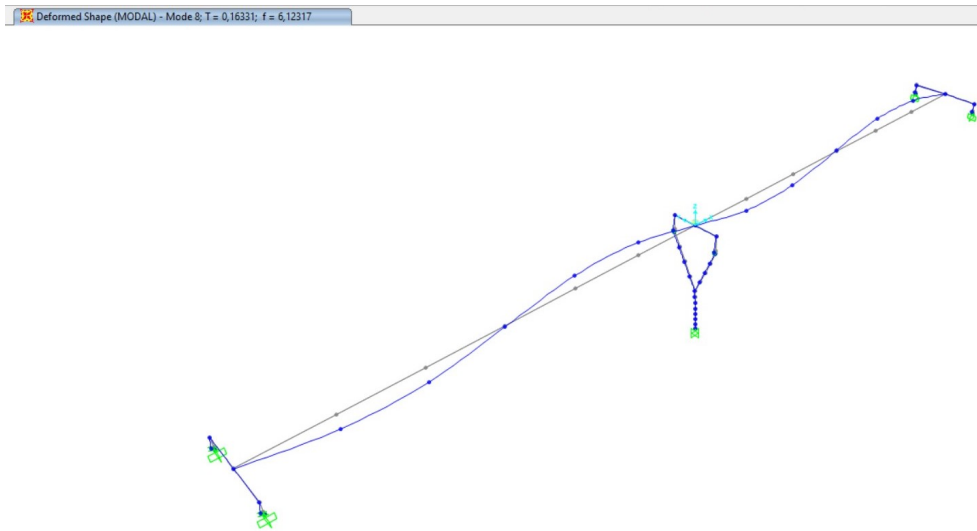


Figure 4.29: 6th vibration mode

The 6th mode shows the synchronized longitudinal deflection of the deck.

Figure 4.30: 7th vibration mode

The 7th vibration mode is a transverse undulatory motion more emphasised than the fifth one.

Figure 4.31: 8th vibration mode

The 8th vibration mode accounts for a longitudinal undulatory motion of the deck with the longitudinal movement of the pier.

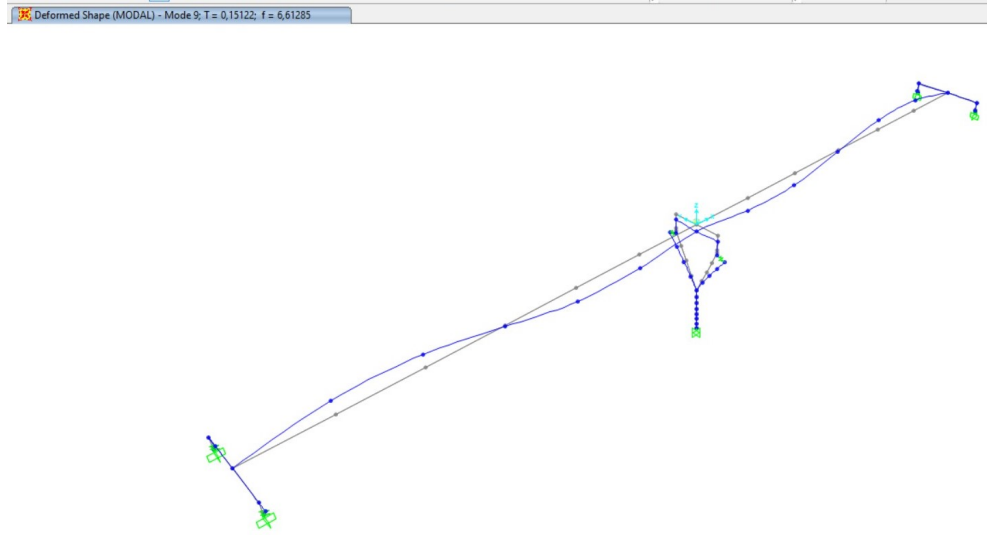


Figure 4.32: 9th vibration mode

The 9th vibration mode depicts a longitudinal undulatory motion of the deck with the oscillatory movement of the arms of the Y-shaped pier.

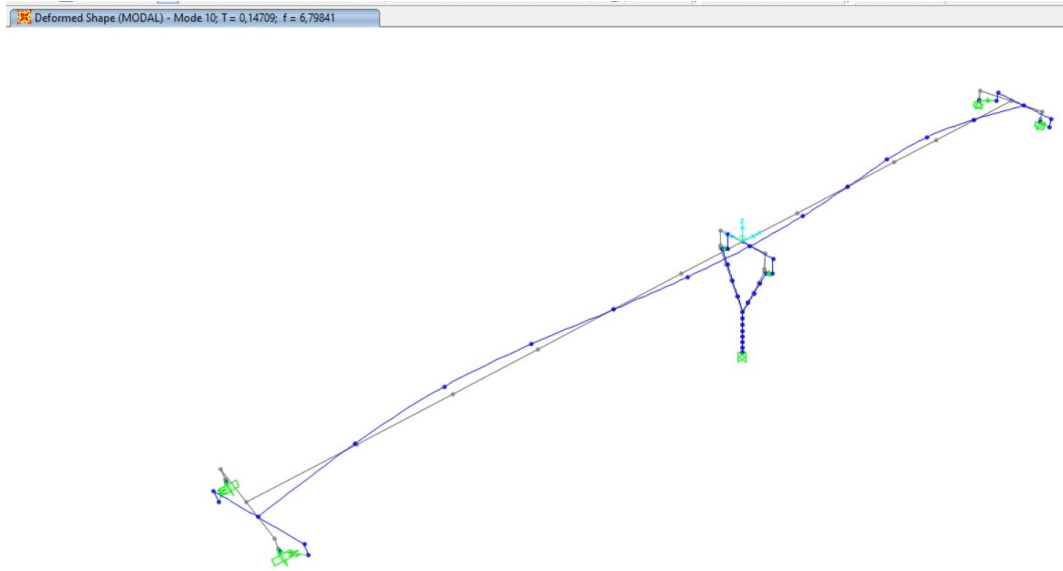


Figure 4.33: 10th vibration mode

The 10th and last vibration mode regard a torsional motion in the abutments with the transverse movement of the deck in the position of the central supports. There is also a

slight movement of the pier, which is much more rigid, in the same direction.

4.12 Computation of the longitudinal steel reinforcement area

When the static linear analysis has been carried out, it is possible computing the steel reinforcement area. Specifically, this computation is related only to the pier because it is the most seismic-affected element. For this reason, longitudinal and transverse steel reinforcement is required.

The reinforcement located at the base has been designed by means of the *capacity design* criterion. The term refers to the assumption that the expected plastic mechanism in bridges is the presence of a plastic hinge in the pier. This is fundamental to avoid a plastic behaviour in the deck and the foundation. So, a safety coefficient is required and it depends on the behaviour factor ($q = 2.7$), as the Italian standard suggests:

$$\gamma_{rd} = 0.7 + 0.2 \cdot q \quad (4.17)$$

Actually, γ_{rd} depends on the dimensionless axial force as well, because of $\nu_k > 0.1$:

$$\gamma_{rd}(\nu_k) = \gamma_{rd}[1 + 2(\nu_k - 0.1)^2] \quad (4.18)$$

$$\gamma_{rd}(\nu_k = 0.4) = 2.43[1 + 2(0.4 - 0.1)^2] = 1.46$$

The materials used in the RC pier are reported below:

- Concrete C40/50: $f_{cd} = \frac{40}{\gamma_c} = \frac{40}{1.5} = 26.67 \text{ MPa}$
- Steel B450C: $f_{yd} = \frac{450}{\gamma_s} = \frac{450}{1.15} = 391.3 \text{ MPa}$

The most affected sections of the pier are two, indicated in Figure 4.34. Basically, these sections are placed at the base (section A) and in the middle of the pier

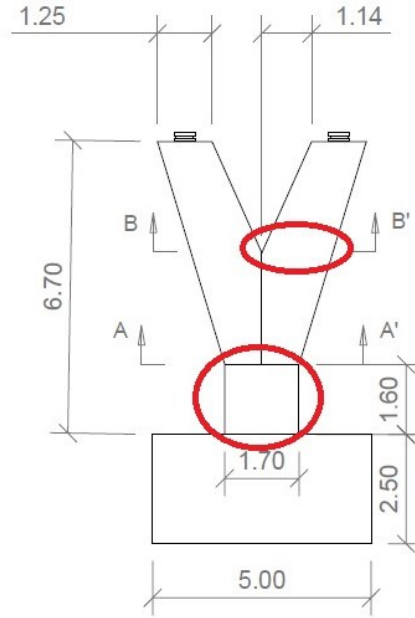


Figure 4.34: Sections of the pier under consideration

(section B).

First, steel amount of **section A** has been computed by means of Montoya's graphs, as follows:

$$\nu = \frac{N_d}{f_{cd}bh} = \frac{18380 \cdot 10^{-3}}{26.67 \cdot 1.7 \cdot 1} = 0.41 \quad (4.19)$$

$$\mu_{xd} = \frac{\gamma_{sr} \cdot M_{xd}}{f_{cd}bh^2} = \frac{1.46 \cdot 3710 \cdot 10^{-3}}{26.67 \cdot 1 \cdot 1.7^2} = 0.07 \quad (4.20)$$

$$\mu_{xd} = \frac{\gamma_{sr} \cdot M_{xd}}{f_{cd}b^2h} = \frac{1.46 \cdot 3710 \cdot 10^{-3}}{26.67 \cdot 1^2 \cdot 1.7} = 0.41 \quad (4.21)$$

The value of the steel reinforcement ratio has been obtained as: $\omega = 0.8$. Afterward, steel reinforcement amount is computed, as follows:

$$A_s = \frac{\omega f_{cd}bh}{f_{yd}} = \frac{0.8 \cdot 26.67 \cdot 1000 \cdot 1700}{391.3} = 92695 \text{ mm}^2 \quad (4.22)$$

Once quantity of steel has been found, the number of bars can be computed by selecting a

4.12. COMPUTATION OF THE LONGITUDINAL STEEL REINFORCEMENT AREA

suitable steel diameter, i.e. $\phi 32$ ($A_b = 804.25 \text{ mm}^2$):

$$n = A_s/A_b = \frac{92695}{804.25} \simeq 116 \text{ bars} \quad (4.23)$$

The bars have been distributed in 2 rows coupled together. Exactly, 40 on the longest side (1.7 m) and 18 on the shortest one (1 m), as can be seen in Figure 4.35 which represents the cross section under consideration.

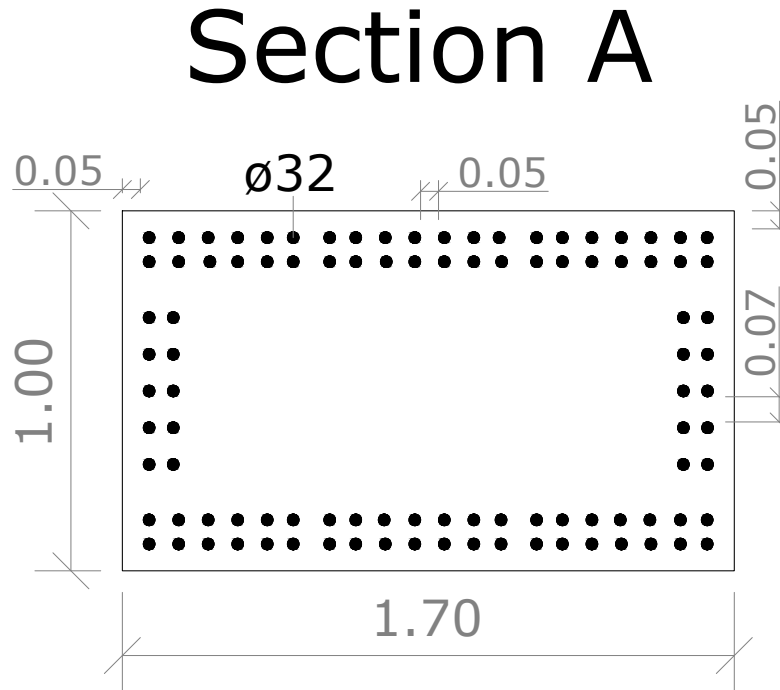


Figure 4.35: Representation of the reinforced Section A

A 50 mm concrete cover and a spacing between bars have been selected to complete the design of longitudinal bars. Especially, in the longest side (1.7 m) the spacing measures 50 mm, and in the shortest one (1 m) is 70 mm, as shown in Figure 4.35.

Successively, the same procedure has been carried out for the remaining **section B**, placed in the middle of the vertical shaft, by means of Montoya's graphs, as follows:

$$\nu = \frac{N_d}{f_{cd}bh} = \frac{8322 \cdot 10^{-3}}{26.67 \cdot 1.5 \cdot 1.62} = 0.13 \quad (4.24)$$

$$\mu_{xd} = \frac{\gamma_{sr} \cdot M_{xd}}{f_{cd}bh^2} = \frac{1.46 \cdot 16494 \cdot 10^{-3}}{26.67 \cdot 1.5 \cdot 1.62^2} = 0.16 \quad (4.25)$$

$$\mu_{xd} = \frac{\gamma_{sr} \cdot M_{xd}}{f_{cd}bh^2} = \frac{1.46 \cdot 2833 \cdot 10^{-3}}{26.67 \cdot 1.5^2 \cdot 1.62} = 0.03 \quad (4.26)$$

The value of the steel reinforcement ratio has been found as: $\omega = 0.5$. Thus, steel reinforcement amount is computed as follows:

$$A_s = \frac{\omega f_{cd}bh}{f_{yd}} = \frac{0.5 \cdot 26.67 \cdot 1500 \cdot 1620}{391.3} = 82812 \text{ mm}^2 \quad (4.27)$$

Once quantity of steel has been found, the number of bars can be computed by selecting a suitable steel diameter, i.e. $\phi 32$ ($A_b = 804.25 \text{ mm}^2$):

$$n = A_s/A_b = \frac{82812}{804.25} \simeq 104 \text{ bars} \quad (4.28)$$

The bars in the main side (1.62 m) have been distributed in two rows coupled together. Exactly, 18 are on the longest side (1.62 m) only in one row. On the other hand, 34 are placed in two rows on the shortest one (1.5 m), as can be seen in Figure 4.36 which depicts the cross section under consideration. A 50 mm concrete cover and a spacing between bars have been selected to complete the design of longitudinal bars. Especially, in the longest side (1.62 m) the spacing measures 50 mm, and in the shortest one (1.5 m) is 50 mm, as shown in Figure 4.36.

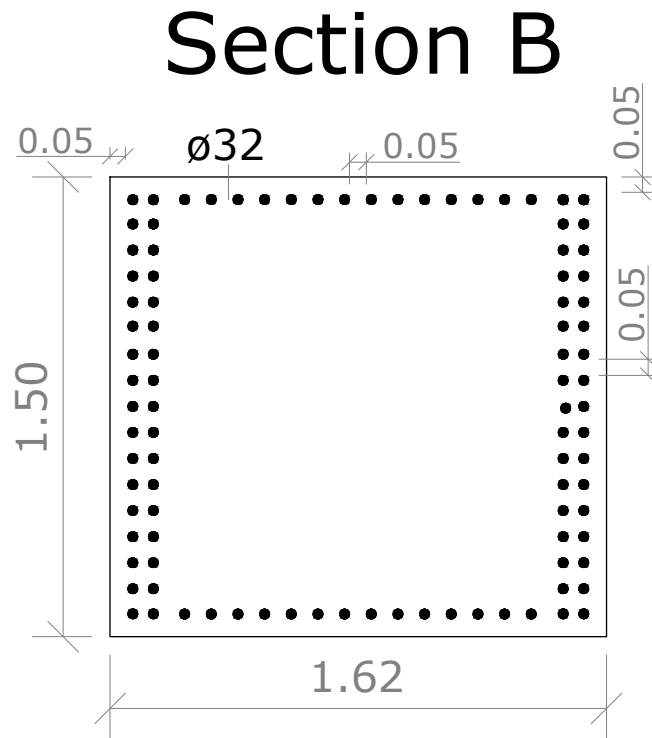


Figure 4.36: Representation of the reinforced Section B

4.13 Computation of the transverse steel reinforcement area

Transverse steel reinforcement is a fundamental aspect of the structure. In addition, this reinforcement consists of stirrups and ties that ensure several advantages to the pier, including:

- Stirrups help to hold in place the primary reinforcement bars. The use of stirrups is needed to prevent the columns and beams from buckling.
- Concrete is made strong by running bars of steel through them. However, stirrups are used to keep everything in a straight line. Stirrups help to keep order and also add strength to the structure at critical points of probable vulnerability from use over time.
- Rebars act as the bones of the concrete, in contrast stirrups aid the rebars to remain straight and provide enhanced backing to the column of concrete inside which it is placed.
- Stirrups help secure much needed strength. When the load is applied on the column, stirrups act like tendons. They help the rebar and concrete to provide sustainable support for the extreme amounts of load.
- The spacing of the stirrup along the beam is important and it should ideally be specified by the designer. This helps the stirrups to be manufactured accordingly.

“For bridges of ductile behaviour, capacity design shall be used to ensure that an appropriate hierarchy of resistance exists within the various structural components. This is to ensure that the intended configuration of plastic hinges will form and that brittle failure modes are avoided.” [38]

Thereby, in each cross section (in this case in the end and in the middle of the pier) the capacity must be greater than the corresponding demand. The applied shear is computed considering the *theory of capacity design* which guarantees a specific order of collapse among the different elements. The goal is to have a ductile behaviour of the whole structure, a correct geometry of the cross section, the right amount of steel and a reduced damage.

Thus, the applied shear is computed from the resisting moment in order to ensure the collapse in shear after the one in bending. The shear action can be expressed by:

$$V_{Ed} = V_E \cdot \frac{M_{Rd}}{M_E} \quad (4.29)$$

Where V_E is the value of the shear force obtained by the linear analysis, M_{Rd} is the effective resisting bending moment, M_E is the corresponding bending moment applied to the section of the pier.

In the **x-direction of Section A** (Fig. 4.35) a value of $V_{E,x} = 536 \text{ kN}$ is obtained from

4.13. COMPUTATION OF THE TRANSVERSE STEEL REINFORCEMENT AREA

the linear analysis (Fig. 4.23), $M_{E,x} = 3710 \text{ kN} \cdot \text{m}$ as well (Fig. 4.20).

In contrast, the resisting bending moment is found by means of the interaction domains. In this case, $M_{Rd,x} = 19166 \text{ kN} \cdot \text{m}$. Once these values are known, the design shear action can be found in Eq. (4.29):

$$V_{Ed,x} = 536 \cdot \frac{3710}{19166} = 2769 \text{ kN} \quad (4.30)$$

The same computation is performed regarding the **y-direction**, as follows:

$$V_{Ed,y} = 1409 \cdot \frac{27532}{9415} = 4120.3 \text{ kN} \quad (4.31)$$

Consequently, this analysis is repeated for the **x and y-direction of Section B** (Fig. 4.36).

$$V_{Ed,x} = 4138 \cdot \frac{21293}{16494} = 5342 \text{ kN} \quad (4.32)$$

$$V_{Ed,y} = 704 \cdot \frac{13567}{2833} = 3371.4 \text{ kN} \quad (4.33)$$

4.13.1 General requirements of the concrete pier confinement in Section A

Ductile behaviour of the compression concrete zone should be ensured within the potential plastic hinge regions. In potential hinge regions the normalized axial force exceeds the limit [38]:

$$\nu = \frac{N_{Ed}}{A_c f_{ck}} > 0.08 \quad (4.34)$$

This means that the confinement of the compression zone should be provided. In particular, all the sections under consideration have the normalised axial force exceeding the limit. Thus, the quantity of confining reinforcement is defined through the mechanical reinforcement ratio:

$$\omega_{wd} = \frac{A_{sw}}{s} \frac{f_{yd}}{b f_{cd}} \quad (4.35)$$

In this case, $\omega_{wd} = \omega_{min} = 0.33 \frac{A_c}{A_{cc}} \nu_k - 0.07 \geq 0.12$

Where:

$$A_{cc} = (b - 2 \cdot d')(h - 2 \cdot d') = (1000 - 2 \cdot 50)(1700 - 2 \cdot 50) = 144 \cdot 10^4 \text{ mm}^2 \quad (4.36)$$

$$A_c = 1700 \cdot 1000 = 170 \cdot 10^4 \text{ mm}^2 \quad (4.37)$$

So, $\omega_{min} = 0.09 < 0.12$, for this reason a value of 0.12 is given.

Successively, a $\phi 14$ steel reinforcement with 6 arms is chosen as type of stirrups. The amount of this stirrup is computed as follows:

$$A_{sw} = 153.94 \cdot 6 = 923.64 \text{ mm}^2 \quad (4.38)$$

Therefore, as a consequence of the mechanical reinforcement ratio (Eq. 4.35), the minimum amount of the ratio A_{sw}/s can be defined in order to verify all the cross sections.

In y-direction:

$$\frac{A_{sw}}{s} = 0.12 \cdot 1000 \frac{26.67}{391.3} \cdot 1000 = 8178.89 \text{ mm}^2/m \quad (4.39)$$

In x-direction:

$$\frac{A_{sw}}{s} = 0.12 \cdot 1700 \frac{26.67}{391.3} \cdot 1000 = 13904.11 \text{ mm}^2/m \quad (4.40)$$

Finally, a spacing of $s = 6 \text{ cm}$ between all the arms of the stirrups and ties is chosen, as the standard recommends [38].

4.13.2 Resisting shear and failure assessment

Shear failure in a RC structure depends on the strut and tie mechanism in compression and tension, respectively. Thus, the resisting shear depends on both cases.

The assessment is given by:

$$V_{Ed} < V_{Rd,min} = \min(V_{Rsd}, V_{Rcd}) \quad (4.41)$$

According to NTC2018, the resisting shear is computed for the compressed concrete and for the transverse steel, as well.

$$V_{Rcd} = 0.31 d \nu b_w \alpha_c \sigma_{cd} = 0.31(1700 - 50) \cdot 0.5 \cdot 1000 \cdot 1.25 \cdot 26.67 = 8526.1 \text{ kN} > 4120.3 \text{ kN} \quad (4.42)$$

- σ_{cd} is the compression strength equal to 26.67 MPa

4.13. COMPUTATION OF THE TRANSVERSE STEEL REINFORCEMENT AREA

- f_{yd} is the yielding strength of the steel equal to 391.3 MPa
- d is the useful height of the cross section
- b_w is the smallest width of the section
- $\nu = 0.5$
- α_c changes with respect to σ_{cp} which is the average compression stress.

$$\sigma_{cp} = \frac{N_{Ed}}{A} = 10.81 \text{ MPa} \quad (4.43)$$

In this case $\alpha_c = 1.25$.

Table 4.15: Values of α_c

$\alpha_c = 1$	for $\sigma_{cp} = 0$
$\alpha_c = 1 + \sigma_{cp}/\sigma_{cd}$	for $0 \leq \sigma_{cp}/\sigma_{cd} \leq 0.25$
$\alpha_c = 1.25$	for $0.25 \leq \sigma_{cp}/\sigma_{cd} \leq 0.5$
$\alpha_c = 5(1 - \sigma_{cp}/\sigma_{cd})$	for $0.5 \leq \sigma_{cp}/\sigma_{cd} \leq 1$

On the other hand, the resisting steel mechanism due to the reinforcement is expressed by:

$$V_{Rsd} = \frac{A_{sw}}{s} 0.9 d f_{yd} = 15394 \cdot 0.9 \cdot (1700 - 50) \cdot 391.3 = 8945.15 > 4120.3 \text{ kN} \quad (4.44)$$

Where A_{sw}/s is the biggest transverse reinforcement in both directions equal to 15394 mm^2/m . Thereby, in both cases the assessment is positively checked.

4.13.3 General requirements of the concrete pier confinement in Section B

The same computation performed in Section A is repeated here for Section B, located in the middle of the pier, outside the plastic hinge zone. In this cross-section the minimum steel amount adopted is equal to the half used in the plastic hinge zone, i.e. $A_{sw}/s = 7697 \text{ mm}^2/\text{m}$ with a spacing of 6 cm between stirrups.

4.13.4 Resisting shear and failure assessment

Shear failure in a RC structure depends on the strut and tie mechanism in compression and tension, respectively. Thus, the resisting shear depends on both cases.

The assessment is given by:

$$V_{Ed} < V_{Rd,min} = \min(V_{Rsd}, V_{Rcd}) \quad (4.45)$$

According to NTC2018, the resisting shear is computed for the compressed concrete and for the transverse steel, as well.

$$V_{Rcd} = 0.31d\nu b_w \alpha_c \sigma_{cd} = 0.31(1620 - 50) \cdot 0.5 \cdot 1500 \cdot 1.13 \cdot 26.67 = 11000.8 \text{ kN} > 5342 \text{ kN} \quad (4.46)$$

The parameters are those used above in Eq. (4.42). The only difference is the average compression stress that changes as follows:

$$\sigma_{cp} = \frac{N_{Ed}}{A} = 3.43 \text{ MPa} \quad (4.47)$$

In this case $\alpha_c = 1 + \frac{\sigma_{cp}}{\sigma_{cd}} = 1 + 0.13 = 1.13$.

On the other hand, the resisting steel mechanism due to the reinforcement is expressed by:

$$V_{Rsd} = \frac{A_{sw}}{s} 0.9 d f_{yd} = 7697 \cdot 0.9 \cdot (1620 - 50) \cdot 391.3 = 4255.72 \text{ kN} < 5342 \text{ kN} \quad (4.48)$$

Where A_{sw}/s is the biggest transverse reinforcement in both directions equal to 15394 mm^2/m . Thereby, in both cases the assessment is NOT positively checked.

Thus, the minimum steel amount previously chosen is not sufficient and, for this reason, the applied shear ($V_{Ed} = 5342 \text{ kN}$) is used here to determine the required minimum steel reinforcement, as follows:

$$\frac{A_{sw}}{s} = \frac{V_{Ed}}{0.9 \cdot d \cdot f_{yd}} = \frac{5342 \cdot 10^6}{0.9 \cdot (1620 - 50) \cdot 391.3} = 9661.66 \text{ mm}^2/\text{m} \quad (4.49)$$

Finally, a $\phi 14$ steel reinforcement with 4 arms is chosen as type of stirrups.

4.13.5 Computation of reinforcements to prevent instability of compressed vertical bars

Finally, according to NTC2018 (§ 7.9.6.1.2) it is recommended to bind the longitudinal reinforcement to prevent the instability of compressed bars. This is possible using a stirrup arm by means of intermediate tie rods arranged in alternating positions along the vertical axis of the pier.

In transverse direction the distance s_T in the horizontal plane between two arms of stirrup or tie-rods must be less than or equal to 200 mm. Indeed, a spacing of 180 mm has been chosen. The minimum number of tie rods necessary to limit the instability of the longitudinal bars along the pier is provided by Equation (4.50) [37].

$$\frac{A_T}{s_T} = \sum A_s \cdot f_{yk,s} \cdot \frac{1}{1.6 \cdot f_{yk,t}} \quad (4.50)$$

Where:

- $A_s = 804.25 \text{ mm}^2$ is the diameter of a longitudinal compressed bar
- A_T and s_T are respectively the area of a stirrup or tie rod arm (in mm^2) and the distance measured in the transverse direction between the arms of the tie rods (m)
- $f_{yk,s}$ and $f_{yk,t}$ are respectively the steel yielding stresses of the vertical and horizontal reinforcement (in this case they have the same value equal to 391.3 MPa)

Thus, in the **longitudinal section** the minimum amount of tie rods is expressed as:

$$\frac{A_T}{s_T} = 2 \cdot \frac{804.25}{1.6} = 1005.31 \text{ mm}^2/\text{m} \quad (4.51)$$

On the other hand, in the transverse section the minimum amount of tie rods is expressed by:

$$\frac{A_T}{s_T} = 4 \cdot \frac{804.25}{1.6} = 2010.63 \text{ mm}^2/\text{m} \quad (4.52)$$

In conclusion, Figure 4.37 shows the two cross-sections under investigation (A and B) with the total reinforcement.

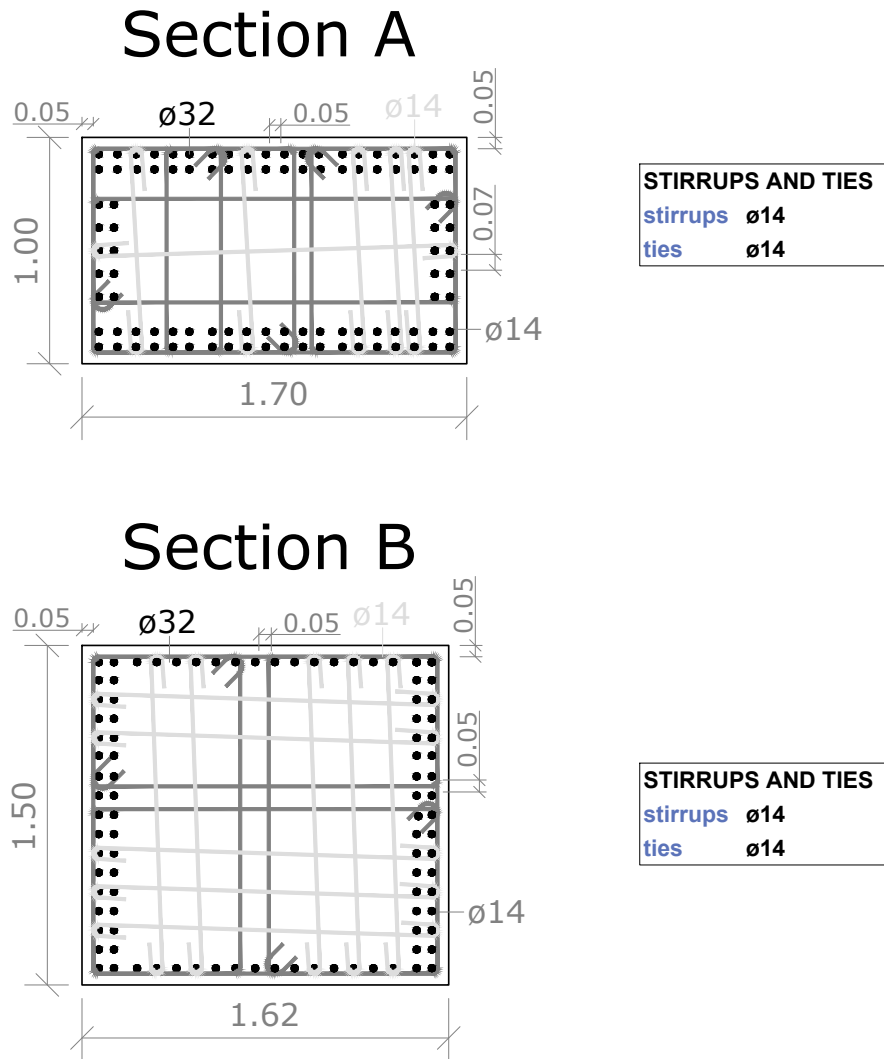


Figure 4.37: Total reinforcement in Section A and B

4.14 Support devices

Support devices are fundamental components in the bridge, and thereby they have the purpose to withstand vertical loads and allow horizontal imposed displacements. In particular, displacements are due to linear and imposed deformations, represented by prestressing force, temperature, creep and shrinkage. Moreover, displacements depend on wind, braking force and especially seismic activity as well.

A bridge bearing is a component of a bridge which typically provides a resting surface between the piers and the deck of a bridge. There are several different types of bridge bearings which are used depending on a number of different factors including the bridge span. A common form of modern bridge bearing is the elastomeric bearing pad, made of reinforced neoprene. They are designed and manufactured based on standards and specifications of organizations such as British Standard, AASHTO, and European Standard EN 1337 [39].

4.14.1 Neoprene bridge bearings

Neoprene bearing pads are moulded or cut from a moulded sheet of high-grade, new neoprene synthetic rubber compounds. Neoprene pads permit a smooth and uniform transfer of load from the deck to the substructure and allow beam rotation at the bearing due to deflection of the beam under load. This kind of supports have no movable parts and thermal expansion and contraction are absorbed by the pad ability to give and take in shear. There is no sliding motion between pad and pier or between pad and abutment. Bearings have steel plates separating the elastomeric layers. Additionally, they are placed at the top of the piers and a Y-shaped column has usually a couple of them, as can be seen highlighted with a red circle in Figure 4.38 regarding the case study of this thesis.

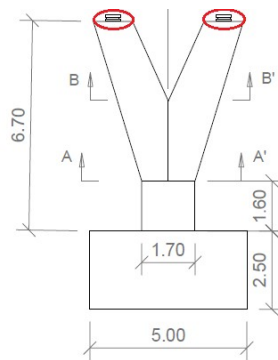


Figure 4.38: Position of the neoprene bridge bearings

4.14.2 Design of the support devices

In order to perform the design of the support devices, an iterative procedure has been chosen respecting the values of deformations according to the standard EN 1337.

The vertical actions, rotation and imposed longitudinal displacements have been determined by *SAP2000* and *Excel*. The horizontal transverse and longitudinal actions, also previously computed, have to be distributed among all the supports. Consequently, geometric features are listed in Table 4.16.

Table 4.16: Geometric features of support devices

	PIER support	ABUTMENT support
a [mm]	700	600
b [mm]	700	600
e_{edge} [mm]	5	6
e_{int} [mm]	10	12
t [mm]	3	3
n	5	7

Where:

- a and b are the two sides of the support base
- e_{edge} and e_{int} are the elastomeric layers in the edges and inside, respectively
- t represents the thickness of the steel plates
- n is the number of the steel plates

Therefore, a couple of **NZ 700x700x5(10+3)** has been chosen as support device in the pier. On the other hand, in the abutments a couple of **NZ 600x600x7(12+3)** has been selected. Thus, the stiffness of the support has been computed as follows:

$$K_p = \frac{A'G}{n e} = \frac{0.4761 \text{ m}^2 \cdot 1800 \text{ kPa}}{5 \cdot 0.01 \text{ m}} = 17140 \text{ kN/m} \quad (4.53)$$

$$K_a = \frac{A'G}{n e} = \frac{0.3481 \text{ m}^2 \cdot 1800 \text{ kPa}}{7 \cdot 0.012 \text{ m}} = 7460 \text{ kN/m} \quad (4.54)$$

Where:

- K_p and K_a are the stiffness of the supports in the pier and abutment, respectively
- G is the stiffness modulus equal to 1.8 MPa referred to instantaneous actions
- A' is the reduced area of the neoprene bearing

Then, the values of the stiffness computed in Eq. (4.53-54) have been inserted into *SAP2000* as “*Support Properties*”. As a result of the analysis, the applied horizontal force has been computed. Thus, all the ULS assessments have been carried out according to the standard EN 1337. A recap is listed in Table 4.17.

Table 4.17: ULS assessments according to EN 1337

Assessment	Outcome
Limitation of distortion ε_{tot}	OK
Buckling stability	OK
Non-slip	OK
Traction in the plates	OK
Limit in rotation	OK

Chapter 5

Application of the corrosion model to the case study

The goal of this chapter is to apply the corrosion model discussed and validated in Chapter 3 to the bridge case study presented in Chapter 4. As explained above, the bridge is located in Sicily, in an atmospheric zone and 1 km from the sea. Cui et al. [24] draw a distinction between splash and atmospheric zone, in contrast this study is only interested in the atmospheric zone, because of the absence of thawing salts in Sicily.

5.1 Deterioration input parameters

Depending on the exposure condition of concrete structures, DuraCrete [27] divides concrete members in marine environments into four categories: a) submerged, b) tidal, c) splash and d) atmospheric exposure. Given that surface chloride concentrations vary significantly with the distance from the coastline, Chinese durability assessment code for concrete structures (CECS) [29] provides a more detailed model for reinforced concrete exposed to marine environments based on data collected in several field investigations. The CECS-recommended parameters to perform the analysis are summarized in Table 5.1. It should be noted that the parameters in Table 5.1 are only applicable to Portland cement. The parameters adopted by the Chinese Institute [29] are compatible with the location of the bridge case study.

Table 5.1: Deterioration input parameters

Parameter	Condition	Units	Value
D_0	w/c = 0.4	mm^2/a	220.9
k_c	Curing 3 day	-	1.5
k_t	All	-	0.85
k_e	All	-	1
X_1	All	-	1
A_{cs}	Atmospheric (distance from coastline (1 km))	-	1.084
n	All	-	0.25
t_0	Reference period (28 days)	years	0.0767
Concrete cover depth d_c	All	mm	50
bars diameter d_0	All	mm	32
Compressive strength of concrete f_{cu}	All	MPa	40
Yield strength of steel f_0	All	MPa	450
water cement ratio w/c	All	-	0.4
Critical chloride concentration C_{cr}	Constantly humid (w/c = 0.4)	-	0.8
Amplification factor R	All	-	7.1

The deterioration parameters reported above have been inserted into *Matlab* in a deterministic way, and the script is shown in Appendix. Thus, the value of the corrosion time has been found as:

$$t_{corr} = 6.7 \text{ years} \quad (5.1)$$

Once the *corrosion propagation phase* has begun, the deterioration process can occur in two possible corrosion forms: pitting and general.

Successively, at initial cracking time, t_{cr} , i.e. the time in which the concrete cover cracks, the *deterioration phase* starts, reaches severe cracking time, t_{Wcr} , and eventually the service life of the bridge ends.

The initial cracking time has been estimated by means of Equation (3.25). Thus, $p_{cr} = 0.0704$ and consequently, $t_{cr} = 11.2$ years.

The severe cracking time is implicit in the formulas and so, it should be determined by numerical methods. However, experimental studies have demonstrated that t_{Wcr} occurs usually 6.4 years after t_{cr} [24].

$$t_{Wcr} = 17.6 \text{ years} \quad (5.2)$$

Once parameters t_{cr} and t_{Wcr} are estimated, the whole corrosion rate model could be obtained by applying the following steps.

5.2 Corrosion rate model

The corrosion rate model is expressed by the corrosion rate function, $\lambda(t)$. As discussed in Chapter 3, this function depends on time during service life as $\lambda(t)$ is affected by many factors [30, 31, 32, 33]. For this reason, the function can be split into three phases based on the precise instant of time (Eq. 3.27).

The behaviour of the corrosion rate function is similar to that found in Cui et al [24]. Figure 5.1 shows a curve that begins vertically at the corrosion time and then reduces sharply during the first few years. This corrosion rate model was derived using a regression analysis of experimental data over a 5-year period in service conditions, which could only depict the beginning phase of chloride-induced corrosion before concrete cracking [24].

Subsequently, the corrosion rate changes more slowly and reaches a nearly uniform value until the initial cracking time. As recent studies suggest [15, 33], after this phase the corrosion rate function has a large continuous increase and crack growth, as concrete cracking leads to easier ingress of chlorides, oxygen and water. After reaching a peak value, $\lambda(t)$ decreases slowly to a steady state in critical cracking condition. This depends on the difficulty that oxygen and moisture have to attain the steel reinforcement surface after the accumulation of corrosion products.

Consequently, the bridge case study of this dissertation is used in order to apply the corrosion rate model to this structure. The input parameters used are those listed in Table 5.1. Once the corrosion model runs, the output behaviour of $\lambda(t)$ function can be plotted. Figure 5.1 refers only to the atmospheric zone.

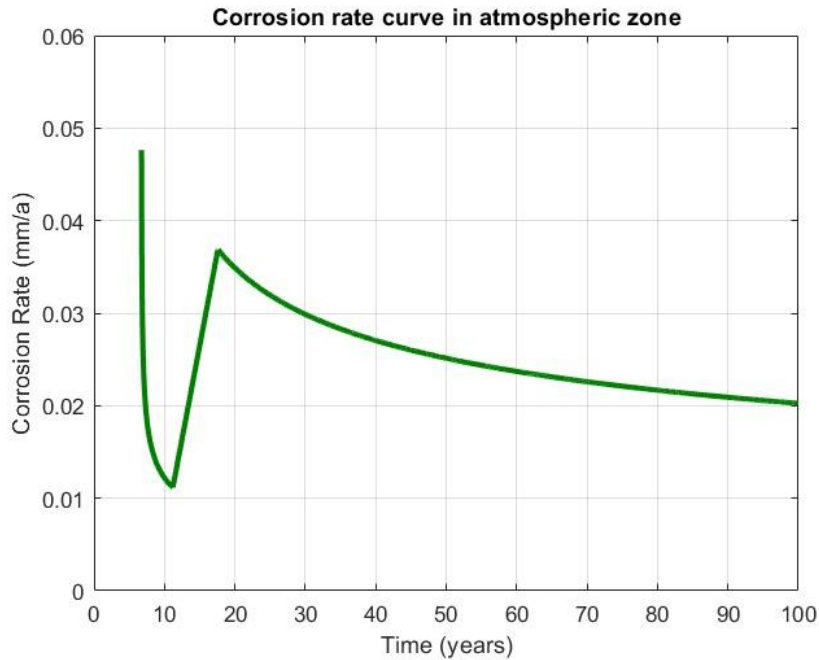


Figure 5.1: Corrosion rate graph obtained by *Matlab*

The most interesting aspect of this graph is that it is similar to the one obtained by Cui et al. As can be seen, the only difference is in the significant points of time (t_{corr} , t_{cr} , t_{Wcr}) that assume other values. This remarkable outcome supports the formulation implemented in this study.

Subsequently, the general and pitting corrosion models have been applied to compute $A(t)$, i.e. the net cross-sectional area of reinforcement bars subjected to corrosion at time t .

5.3 General corrosion analysis

The general corrosion model consists of a uniform distribution. The residual reinforcement diameter at time t can be determined as in Eq. (3.15). Accordingly, the residual cross-sectional area of reinforcement at any time t is expressed as in Eq. (3.16). Figure 5.2 shows the general corrosion situation obtained by the *Matlab* script.

In this case, the curve follows a clear trend represented by a gradual decline of the residual cross-sectional area of reinforcement, as the study expected. The loss percentage regarding the area of reinforcement is around 26.57%.

These results reflect those of Cui et al. [24] who also found a decreasing trend. In addi-

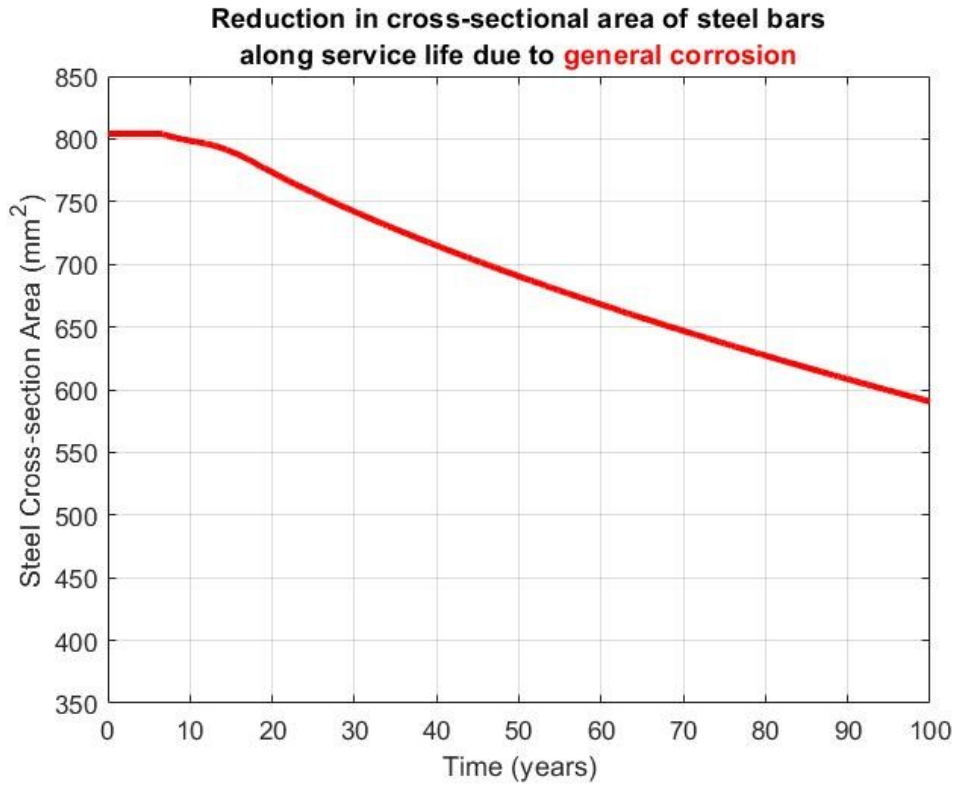


Figure 5.2: Reduction in cross-sectional area due to general corrosion

tion, the findings reported in the study by Cui et al. show a greater decrease (32.86%). This is due to the different zone taken under examination, i.e. the splash zone. Thus, the deteriorating process is faster and the loss percentage regarding the area of reinforcement is greater along 100 years service life.

5.4 Pitting corrosion analysis

Pitting corrosion is the primary cause for marine chloride-induced corrosion under service conditions. The model proposed by Val and Melchers [8] has been taken into account to simulate the development of pitting corrosion. In the model, pitting corrosion is assumed to take a hemispherical form as shown in Figure 3.1.

The net cross-sectional area of reinforcement bars which depends on the pitting depth expansion can be computed as reported in Eq. (3.4).

The parameters used above are the same as those applied in Chapter 3 [27]. Thus, Figure 5.3 illustrates what has been found by the Matlab code for the pitting corrosion situation in atmospheric zone. The pitting corrosion case depicts a graph where the curve has a

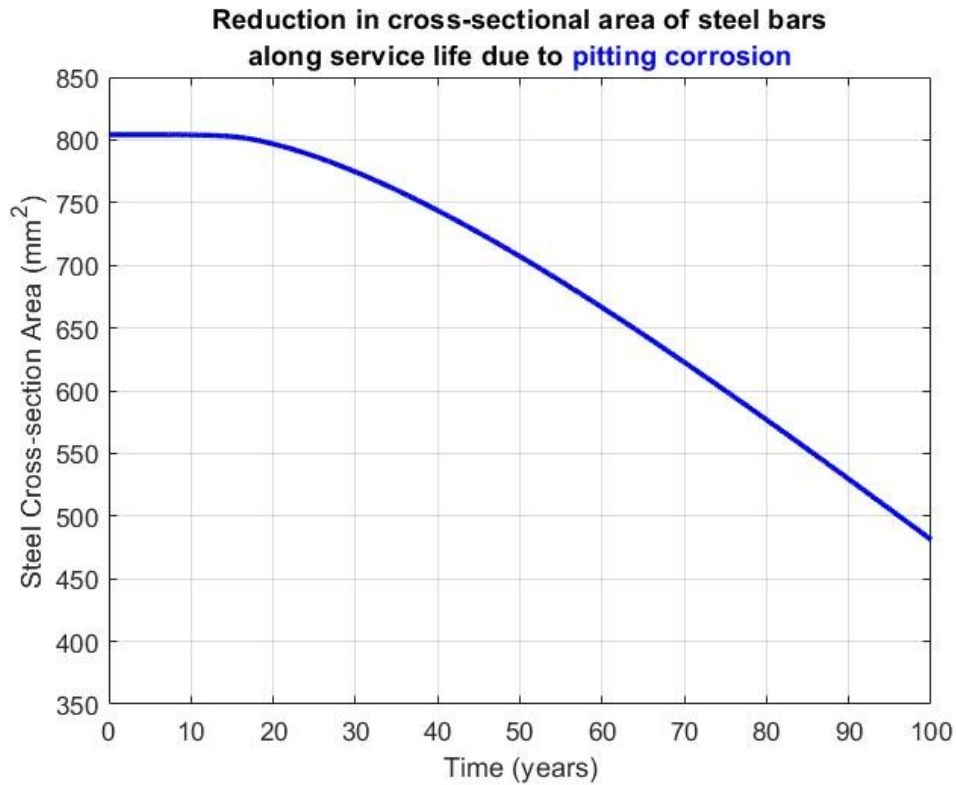


Figure 5.3: Reduction in cross-sectional area due to pitting corrosion

step decrease, due to the stronger corrosion effect. Indeed, the loss percentage regarding the area of reinforcement is around 40.17%.

In accordance with the present results, previous studies [24] have demonstrated that a significant reduction in cross-sectional area in atmospheric zone is present. In terms of percentage, the lost area of reinforcement is around 53.06%.

Similar to the case of general corrosion, here the percentage obtained by Cui et al. is greater due to the lowest distance from the sea. In particular, Cui et al. choose a case study far 0 km from the sea. In contrast, in the bridge case study of this dissertation the distance is 1 km.

Finally, a comparison between the two figures for the case of pitting and general corrosion is shown in Figure 5.4. The two curves in blue and red, related respectively to pitting and general case, have been found by *Matlab*. It can be seen from Figure 5.4 that

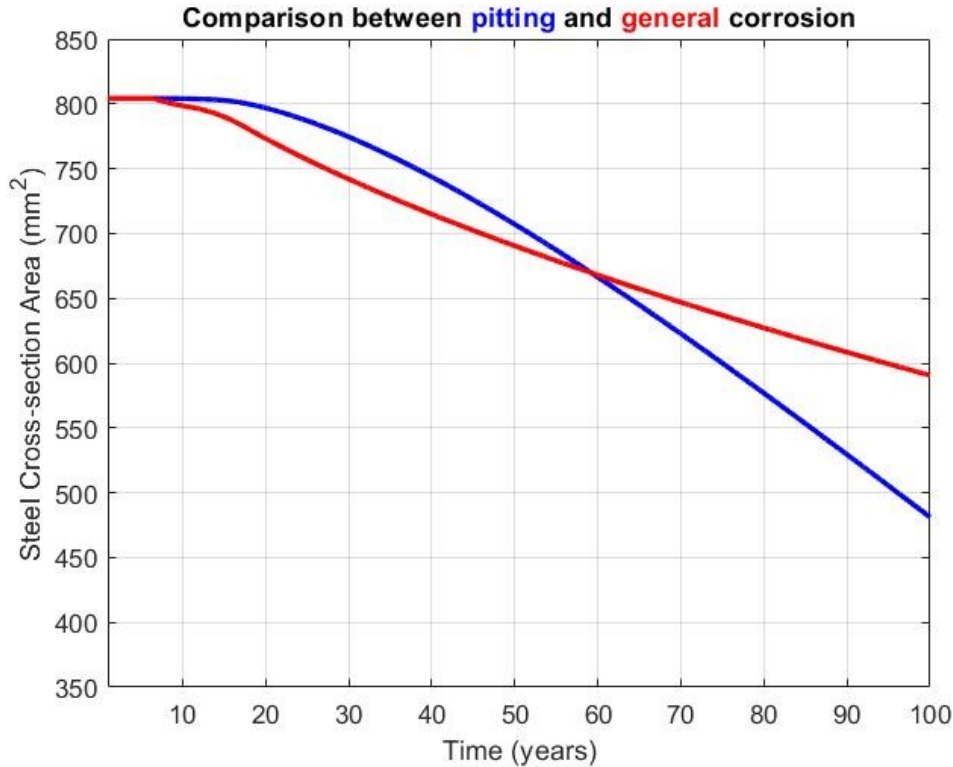


Figure 5.4: Comparison of pitting and general corrosion

the steel cross-sectional area reduction of pitting corrosion exceeds the general corrosion after 60 years and then, the gap between them increases quickly with time. In the case of the general corrosion, the model has 26.57% as the loss percentage of the area. In contrast, with regard to pitting the loss percentage is more, that is 40.17%.

Consequently, the usual general corrosion model can underestimate the long-term influence of chloride-induced corrosion on structural performance. That is, it can be non-conservative for the design and maintenance of RC substructures of the bridge [24].

Thus, Table 5.2 numerically reports the experimental data on $A(t)$ which decrease with time in both situations.

Table 5.2: Experimental data of residual steel area changing with time

t [years]	A(t) general [mm^2]	A(t) pitting [mm^2]
0	804	804
10	799	804
20	773	797
30	742	775
40	715	744
50	690	707
60	668	665
70	647	623
80	627	577
90	608	529
100	591	481

5.5 Combination of general and pitting corrosion analysis

A combination of general and pitting corrosion effects can occur along bridge service life. Chloride attack and carbonation can operate synergistically, creating serious problems, predominantly in hot coastal areas, such as in the location of the bridge case study [40]. Thus, an in-depth analysis is considered in this thesis as well, in order to prevent the most dangerous corrosion effect regarding the combination of general and pitting forms.

Thereby, Equation 5.3 has been used to find the residual cross-sectional area of steel bars due to general and pitting corrosion effects. The findings related to Equation 5.3 are shown in Figure 5.5, which accounts for a greater area loss due to the sum of the two corrosion contributions.

$$A(t) = A_0 (1.0 - (P_{general} + P_{pitting})) \quad (5.3)$$

Where:

- $A(t)$ = residual cross-sectional area of reinforcement due to general and pitting corrosion at time t
- A_0 = initial net cross-sectional area of reinforcement
- $P_{general}$ = percentage of reinforcement area loss due to general corrosion

- $P_{pitting}$ = percentage of reinforcement area loss due to pitting corrosion

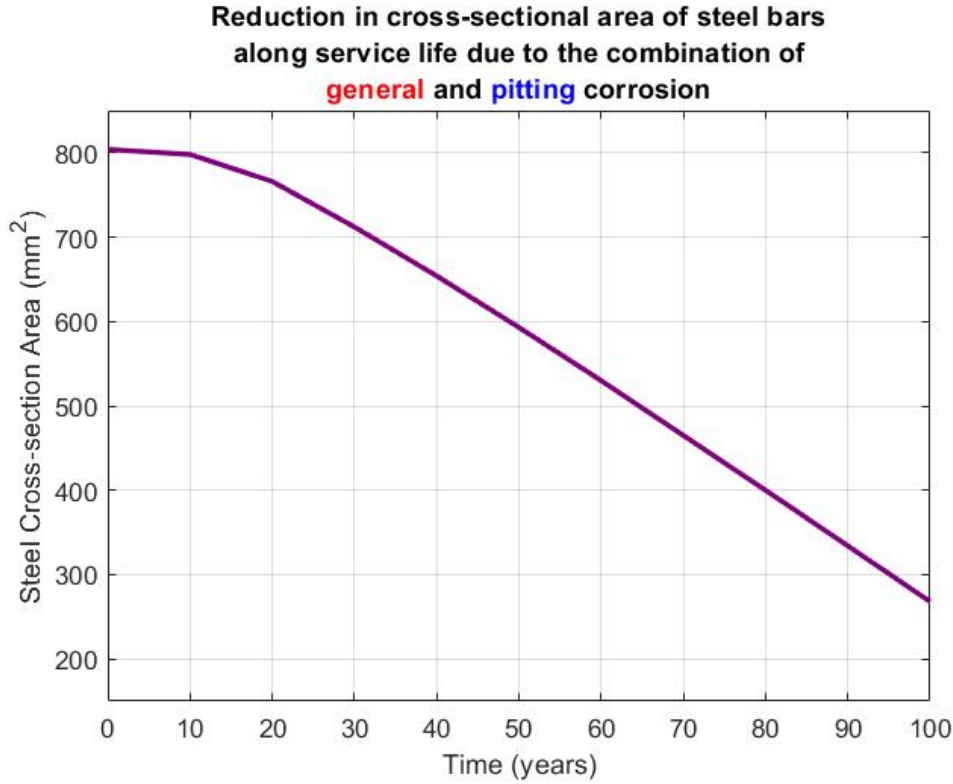


Figure 5.5: Reduction in cross-sectional area due to general and pitting corrosion

5.6 Yield strength analysis

Another relevant aspect regards the reduction of the reinforcement yield strength along the service life of the bridge using equations proposed by Du et al. [6]. This can be expressed by:

$$f(t) = (1.0 - 0.005Q_{corr}) f_0 \quad (5.4)$$

Where:

- $f(t)$ = yield strength of corroded reinforcement at time t
- f_0 = yield strength of non-corroded reinforcement (450 MPa)
- Q_{corr} = corrosion percent (%) of reinforcement in terms of area loss, that can be represented as:

$$Q_{corr}(t) = \frac{(A_0 - A(t))}{A_0} \cdot 100 \quad (5.5)$$

- A_0 is the initial net cross-sectional area of reinforcement
- $A(t)$ is the residual cross-sectional area of reinforcement due to pitting corrosion

Therefore, the graph described in Figure 5.6 shows the decreasing trend of the yield strength of corroded reinforcement with time.

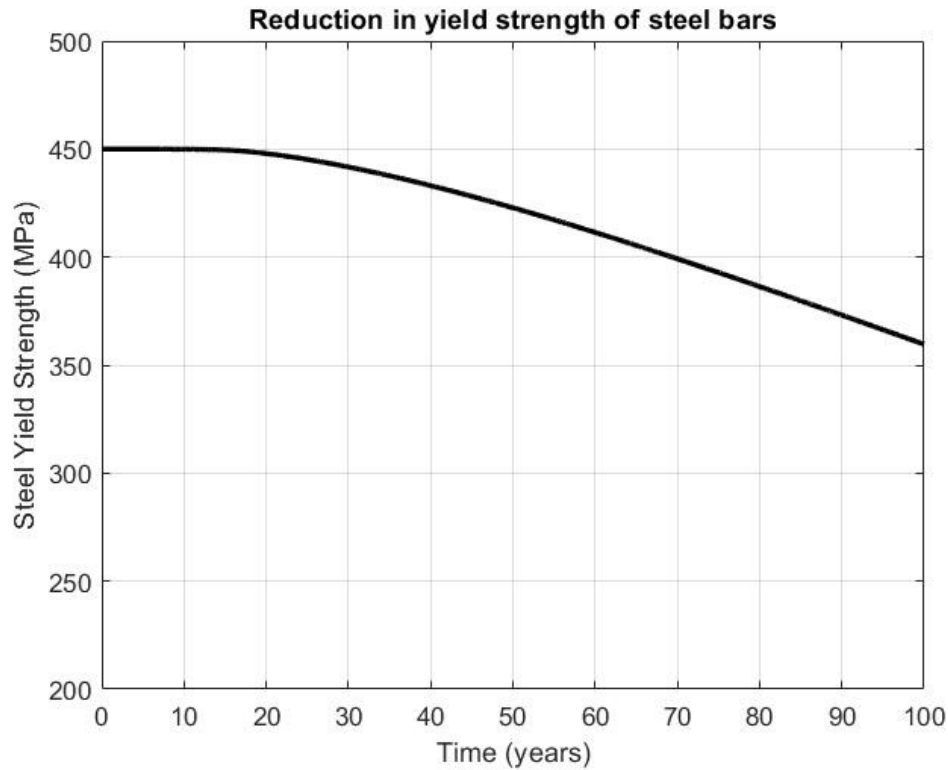


Figure 5.6: Reduction in yield strength of steel bars

The loss percentage regarding the yield strength of steel bars is 20%. It is clear that the reduction of the residual capacity of corroded reinforcement is caused by the local attack

penetration on the reinforcement surface and stress concentration in the pitting surface. As a result, the yield strength of reinforcement also decreases with corrosion along 100 years, as shown in Figure 5.6. Hence, the residual capacity of corroded reinforcement decreases significantly [6].

Chapter 6

Interaction domains and ductility performance

This chapter discusses how the findings obtained in the previous chapter determine the structural capacity of the bridge. Additionally, the reduction of the ductility performance is considered and computed, as an important requirement of the structure.

The main aim of this chapter is to check the effect of seismic action and corrosion on the bridge case study along 100 years. Thus, analysis is based on the use of interaction and Bresler's domains.

6.1 Ductility performance

The ductility of a material is a physical property that indicates its ability to deform under load by exhibiting plastic deformations before reaching failure. The materials that most benefit from this property are metals, including steel [41].

Ductility tends to decrease with material ageing and use. Corrosion leads to a reduction in steel ductility as well, which can effectively be represented by ultimate strain. A significant analysis and discussion on the study was presented by Zhang et al. [42] that investigated the reinforcement ultimate strain at different degrees of corrosion. Additionally, the researchers observed that the time-variant function for steel ultimate strain can be expressed by:

$$\varepsilon_u(t) = (1.0 - 0.0137Q_{corr})\varepsilon_{u0} \quad (6.1)$$

Where:

- $\varepsilon_u(t)$ = ultimate strain of corroded reinforcement at time t due to pitting corrosion

- ε_{u0} = ultimate strain of non-corroded reinforcement equal to 0.0675 for the B450C steel
- Q_{corr} = corrosion percent (%) in terms of area loss

Thereby, the relationship presented in Eq. (6.1) has been implemented into *Matlab* in order to obtain the graph shown in Figure 6.1.



Figure 6.1: Reduction in ultimate strain of steel bars

Furthermore, Table 6.1 refers to the values of $\varepsilon_u(t)$, which change every 20 years.

As can be seen from the graph in Figure 6.1, there is a clear decreasing trend, i.e. the reduction of $\varepsilon_u(t)$ which changes with time, is 54.96% in terms of percentage. This means

Table 6.1: Values of steel ultimate strain changing every 20 years

t [years]	$\varepsilon_u(t)$ [-]
0	0.0675
20	0.0667
40	0.0605
60	0.0516
80	0.0413
100	0.0304

that more than half of the initial ultimate strain is lost during the service life of the bridge. In fact, the ultimate strain of corroded reinforcement decreases up to 0.0304.

Interestingly, this relationship is strongly related to the reduction in the ductility of steel reinforcement, that represents a significant requirement to withstand seismic action. The values found in Table 6.1 are used below to check the ductility performance of the pier along the bridge service life.

6.2 Interaction domain

The interaction domain is a safety zone represented by the geometric locus of M-N pairs that define the strength limits of the cross-section of a structural member under combined compression and bending [43]. The domain consists of the totality of the couples (N_{rdu}, M_{rdu}) that constitute situations of failure for the section. Indeed, these couples of points delimit the safe zone of the section (points inside the domain) compared to points where the section could not be verified (points outside the domain).

Therefore, the safety domain is made by points, by taking into account that the compressive zone is negative and the tensile one is positive. On the x-axis the axial force is present, while bending moment is represented on the y-axis.

The aim of this study is to create all the interaction domains in order to investigate if the reinforced section under consideration can withstand the applied actions (in this case N, M_x, M_y). The analysis was carried out using an *Excel spreadsheet*, which calculated all the points of the safety domain once the cross-section geometry and the amount of steel reinforcement were known.

Moreover, the residual ultimate strain and yield strength of steel bars have been considered such as input data regarding steel parameters, accordingly with Figure 6.1 and 5.5, respectively. The relationships have been obtained by means of Equation (6.1) and (5.3),

reported below:

$$\varepsilon_u(t) = (1.0 - 0.0137Q_{corr})\varepsilon_{u0}$$

$$f(t) = (1.0 - 0.005Q_{corr}) f_0$$

The two sections analysed here are reported in Figure 6.2. They are the same as those examined in Chapter 4 by computing the amount of steel area.

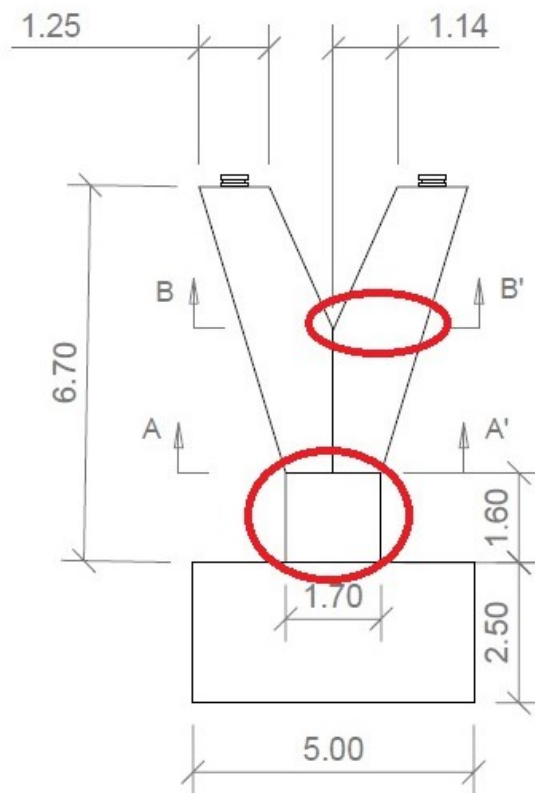


Figure 6.2: Pier sections analysed

Additionally, the two cross-sections are placed at the base of the pier and in the middle where the Y-shaped structure begins. Obviously, the reinforcement is different for each of the two sections, as can be seen in Figure 6.3.

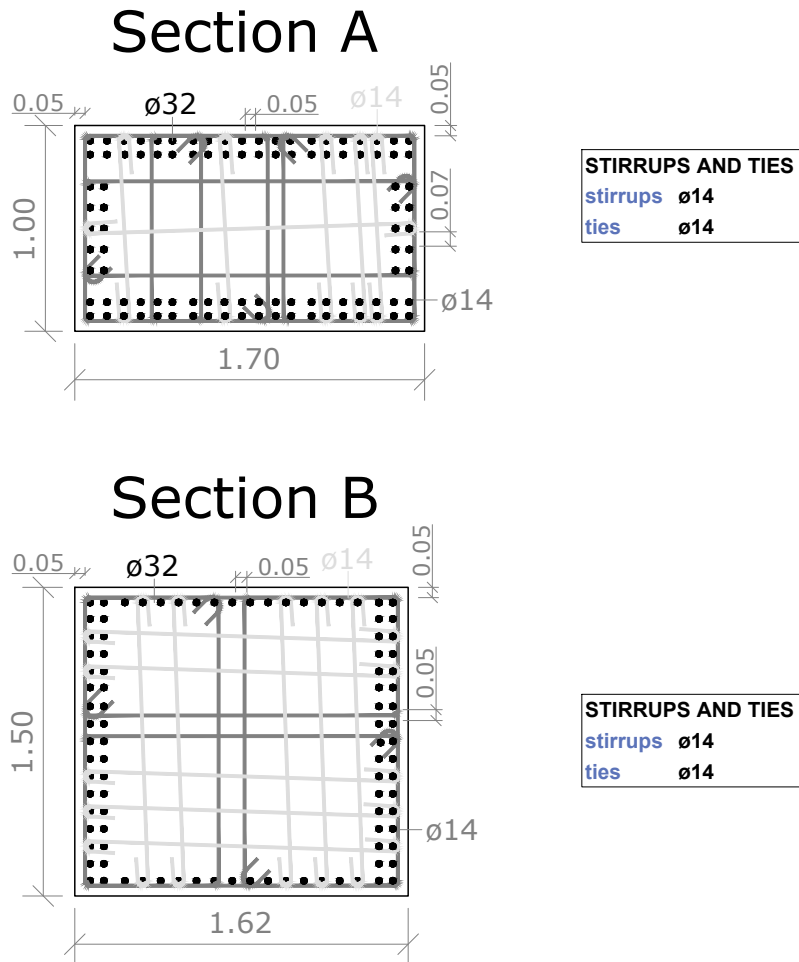


Figure 6.3: Total reinforcement of Section A and B

Once the amount of steel reinforcement is known, the interaction domain can be found. Successively, the couple position regarding the applied actions (N, M_x) or (N, M_y) is checked in order to see if the point is inside the safety domain.

The applied actions related to Section A (at the base) are:

- $N = -18380 \text{ kN}$ (compression)
- $M_x = 3710 \text{ kN} \cdot \text{m}$

- $M_y = 9415 \text{ kN} \cdot \text{m}$

On the other hand, in Section B (in the middle) there are:

- $N = -8322 \text{ kN}$ (compression)
- $M_x = 16494 \text{ kN} \cdot \text{m}$
- $M_y = 2833 \text{ kN} \cdot \text{m}$

In addition, all the interaction domains depend on time, because the area of steel reinforcement decreases with time. This means that the safety zone reduces with time and thus, the interaction domain shrinks increasingly.

In accordance with the present results, reported in Figure 6.4-11, previous studies [44] have demonstrated that the appearance of interaction domains is similar to that obtained in this dissertation. Indeed, the time-variant interaction domains show the reduction of the safety surface due to the corrosion percentage increase.

Basically, all steel parameters which determine the interaction domains surface that changes with time are summarized as follows:

- residual ultimate strain, $\varepsilon_u(t)$, expressed by Eq. (6.1)
- residual yield strength, $f(t)$, expressed by Eq. (5.3)
- residual reinforcement area due to general corrosion, $A(t)$, expressed by Eq. (3.16)
- residual reinforcement area due to pitting corrosion, $A(t)$, expressed by Eq. (3.4)

Table 6.2 numerically summarizes how the area changes every 20 years in the case of general and pitting corrosion.

Table 6.2: Experimental data of residual steel area changing with time

t [years]	A(t) general [mm^2]	A(t) pitting [mm^2]
0	804	804
20	773	797
40	715	744
60	668	665
80	627	577
100	591	481

Consequently, Figure 6.4-11 show all the interaction domains (coloured continuous lines) that change with time related to 0 (black), 20 (yellow), 40 (purple), 60 (green), 80 (red), 100 (blue) years of the service life of the bridge case study. In contrast, the orange point represents the coordinates of the design point.

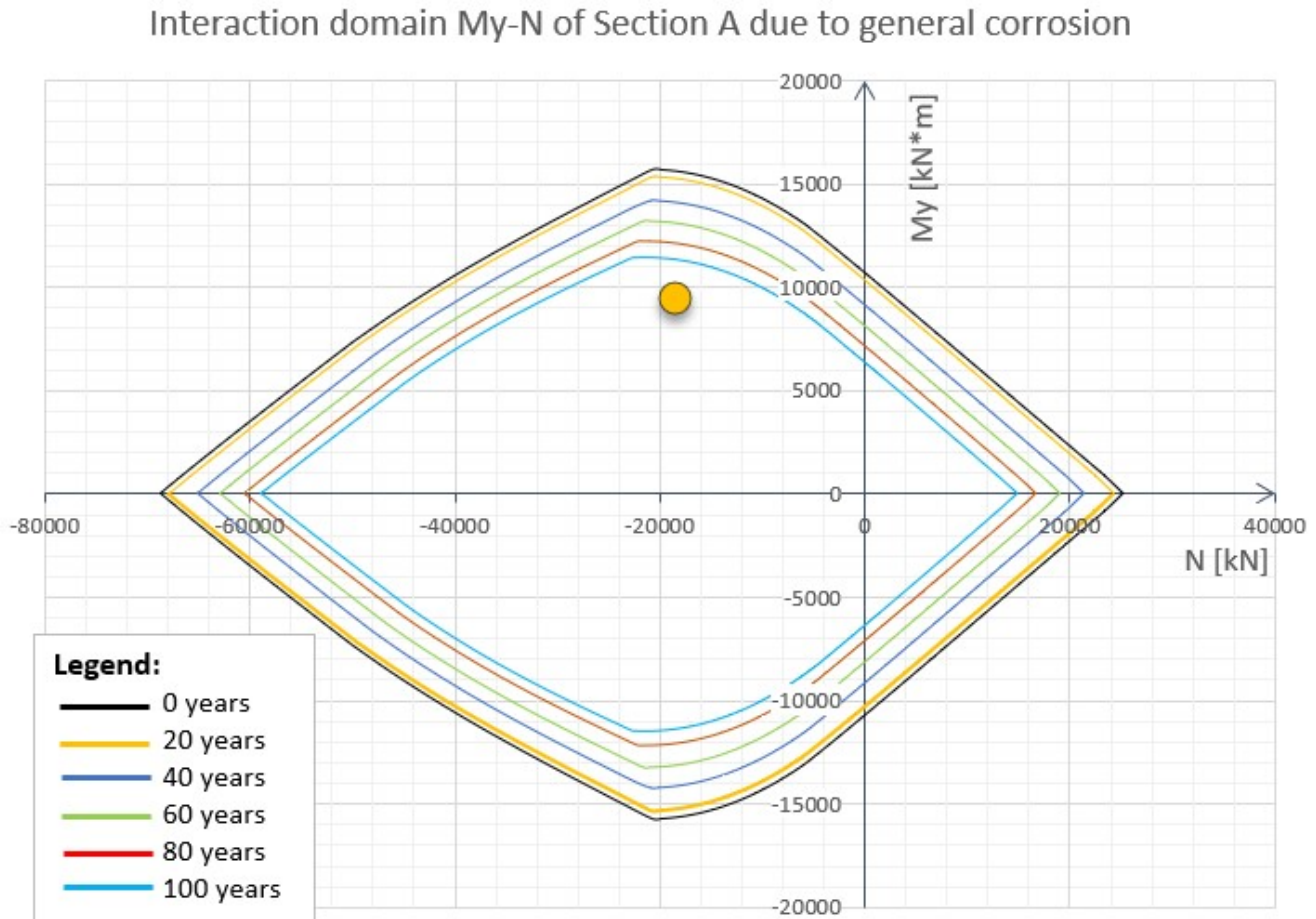


Figure 6.4: Interaction domain of Section A due to general corrosion

In Figure 6.4 the point is checked positively.

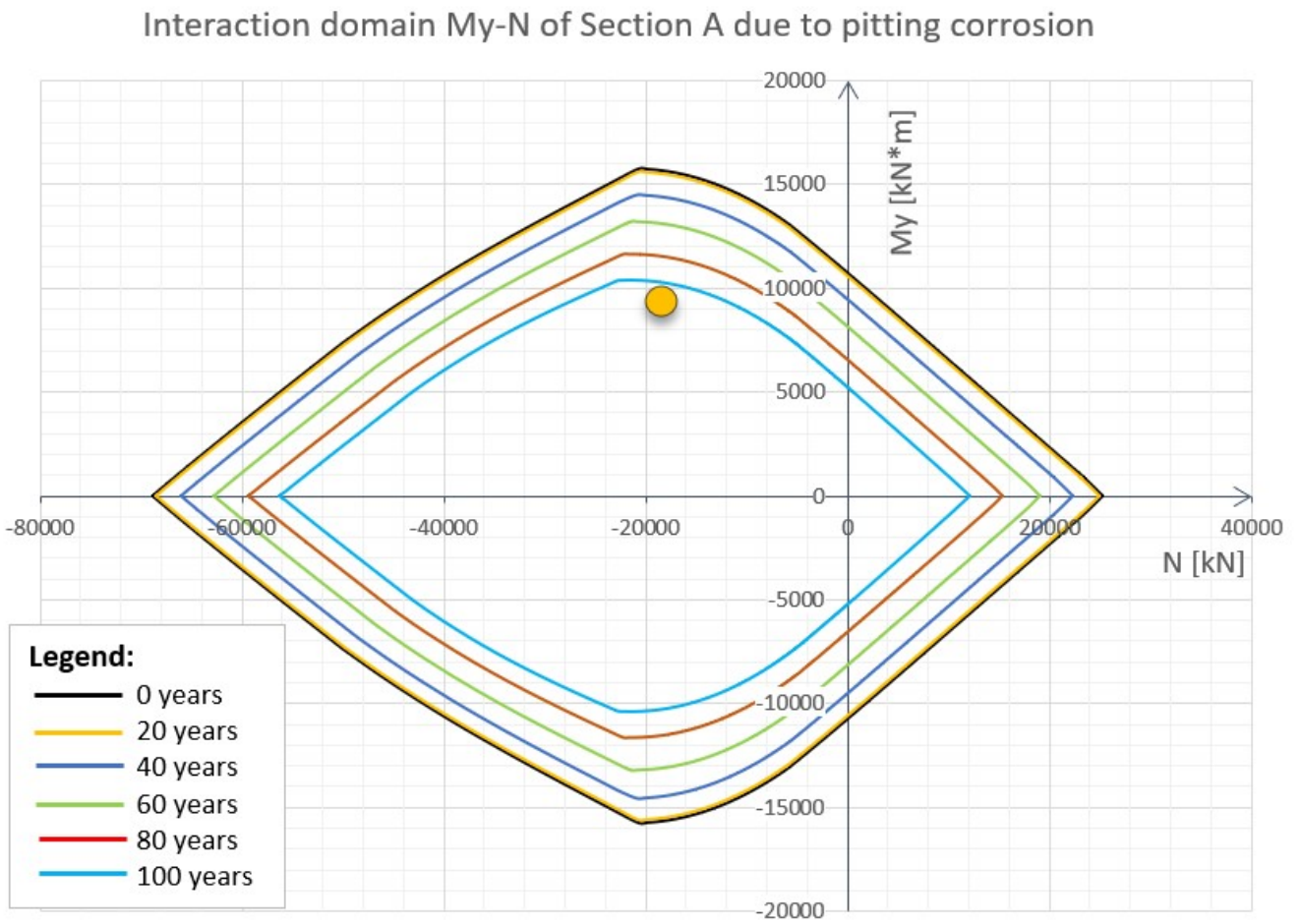


Figure 6.5: Interaction domain of Section A due to pitting corrosion

In Figure 6.5 the point is checked successfully.

Interaction domain Mx-N of Section A due to general corrosion

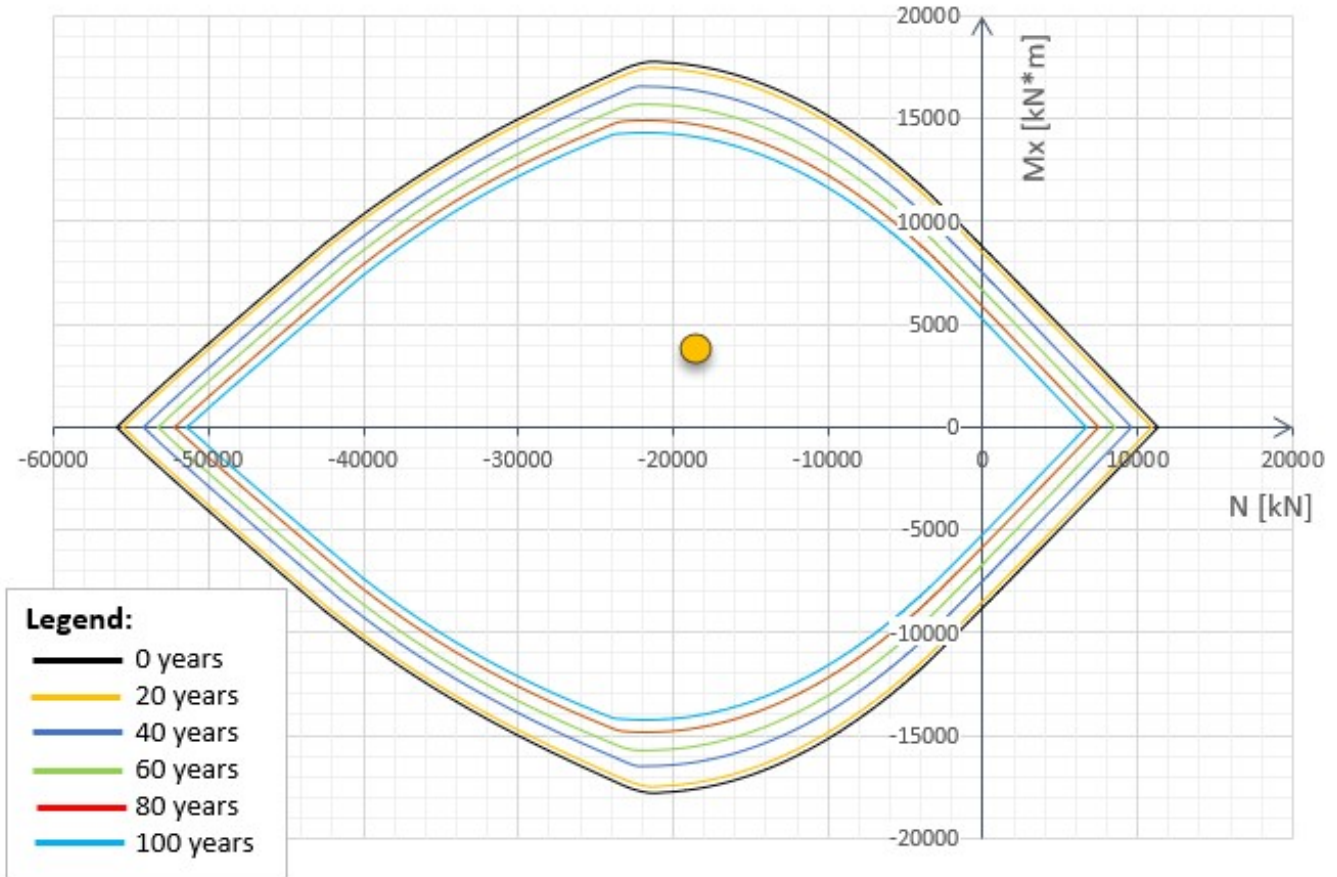


Figure 6.6: Interaction domain of Section A due to general corrosion

Figure 6.6 shows that the orange point is inside the safety domain.

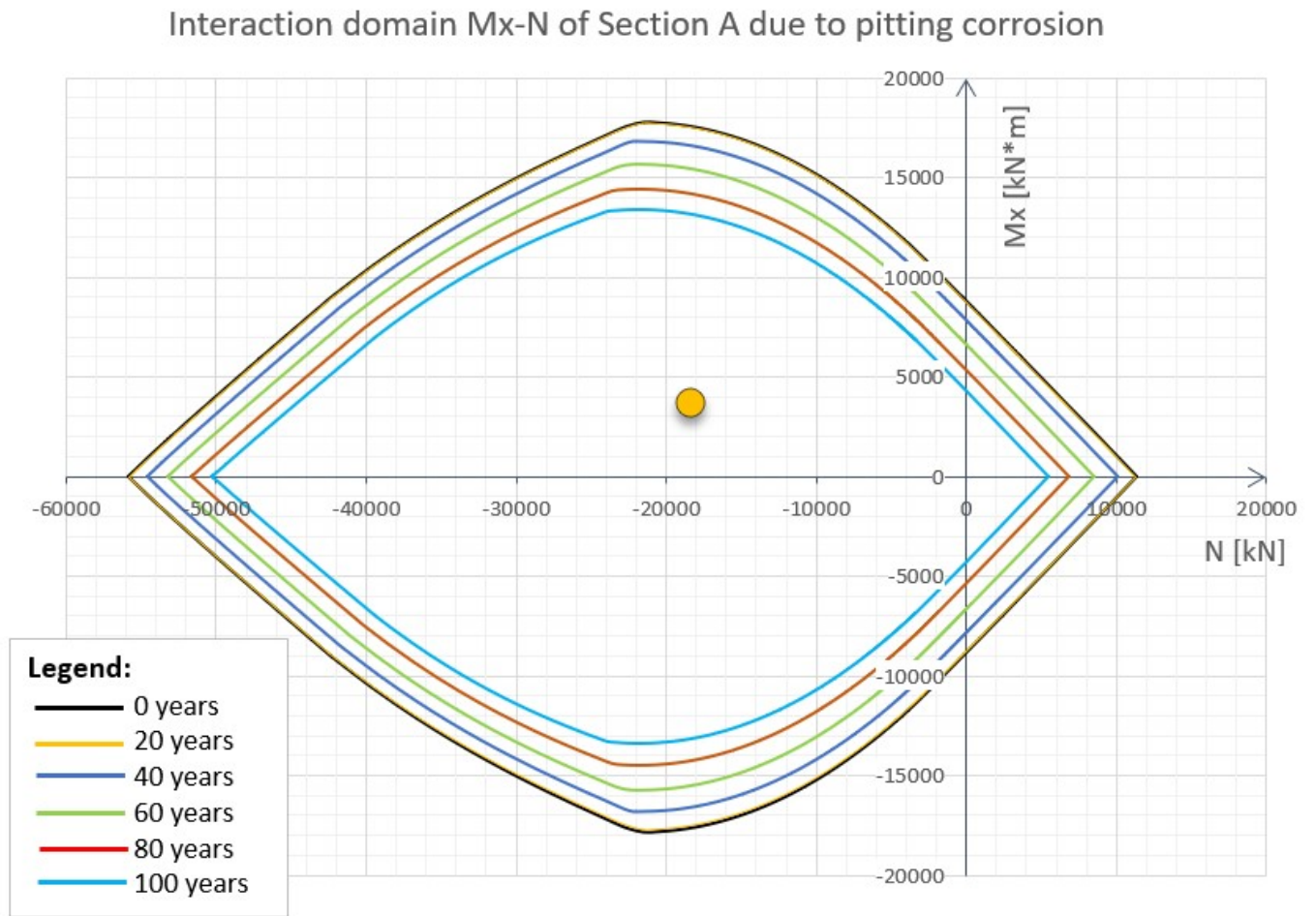


Figure 6.7: Interaction domain of Section A due to pitting corrosion

In Figure 6.7 the point is checked successfully.

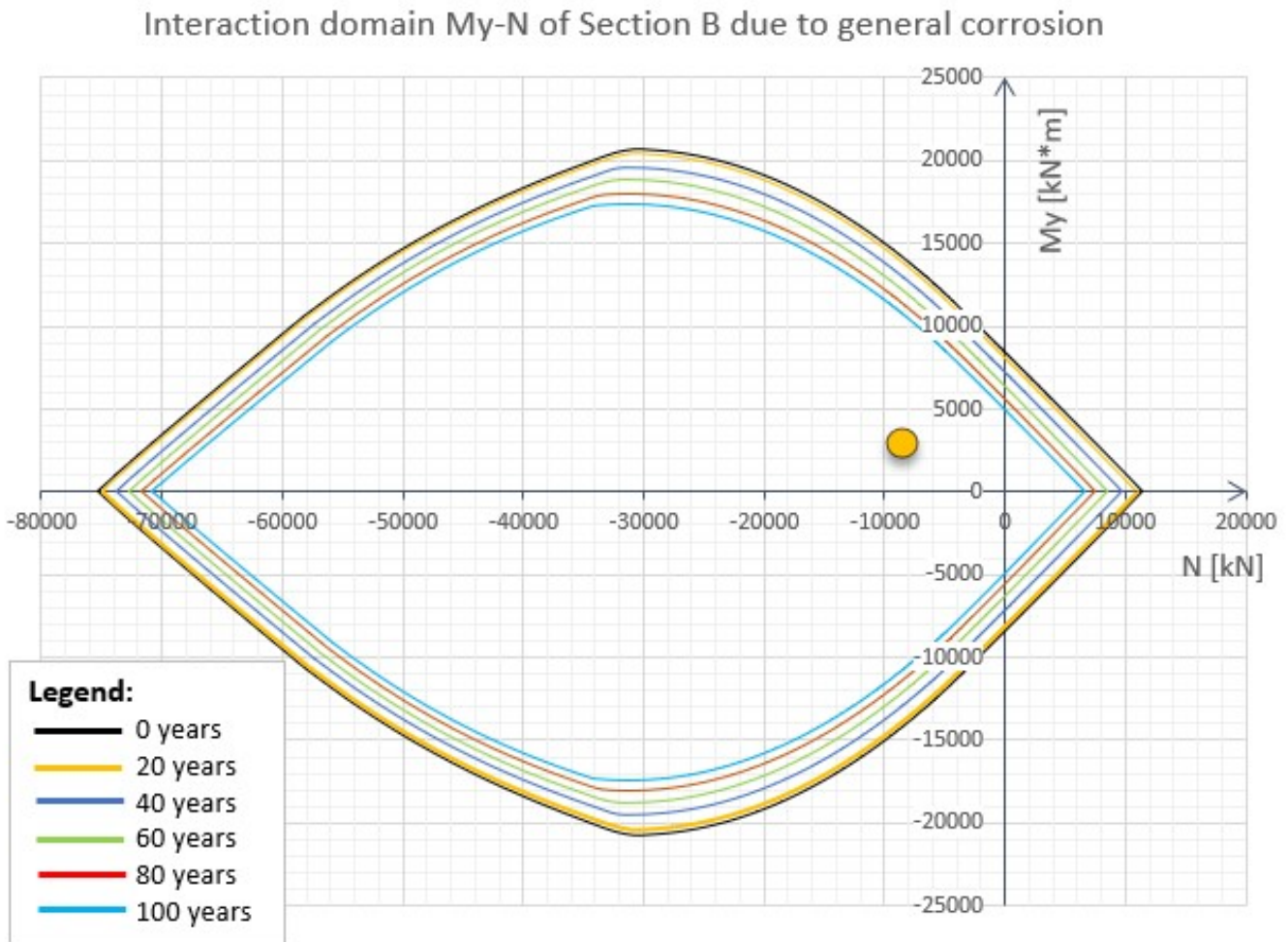


Figure 6.8: Interaction domain of Section B due to general corrosion

Figure 6.8 illustrates the interaction domain regarding Section B. This check satisfies all the requirements as well.

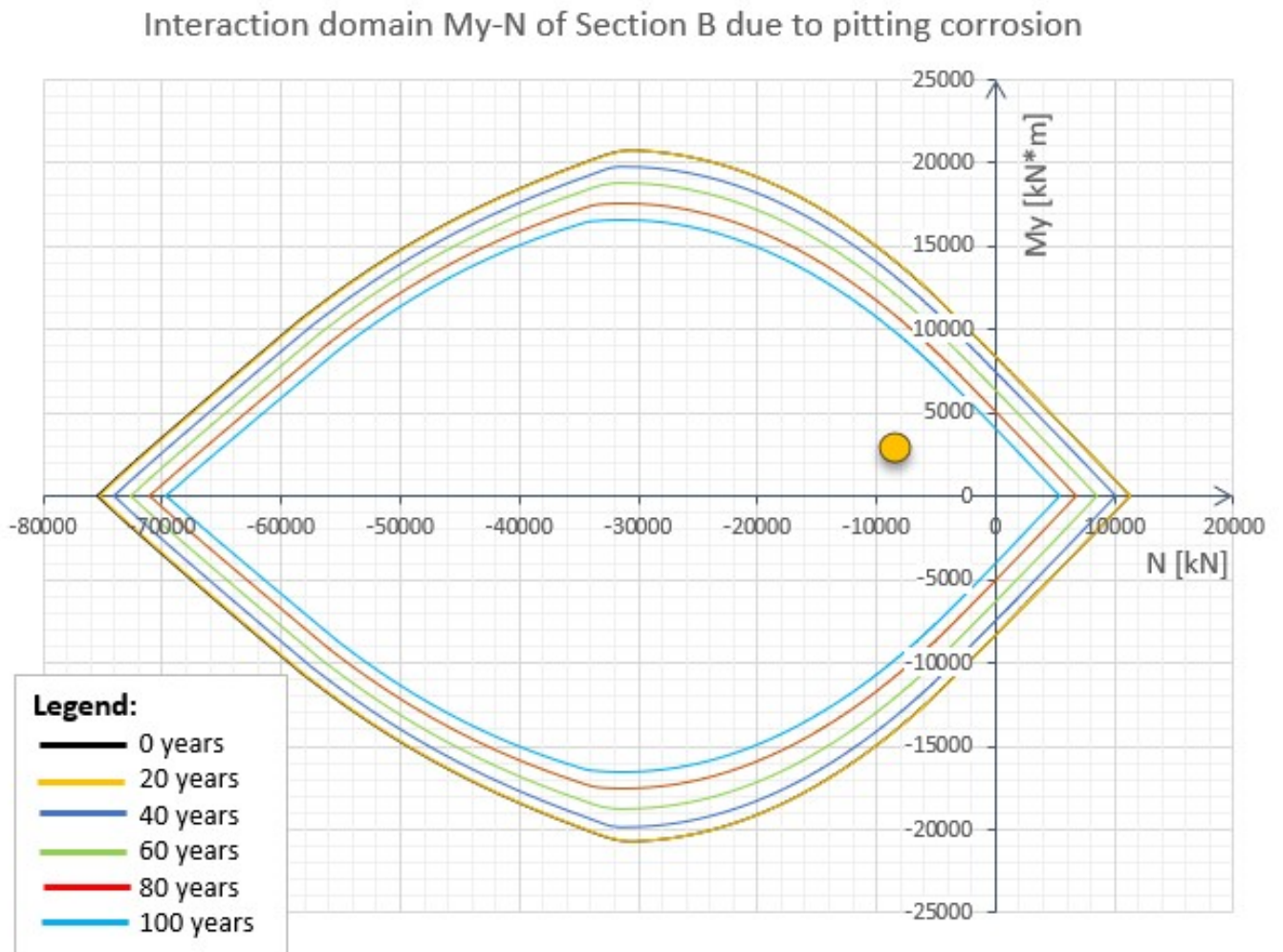


Figure 6.9: Interaction domain of Section B due to pitting corrosion

As shown in Figure 6.9, the point is checked positively.

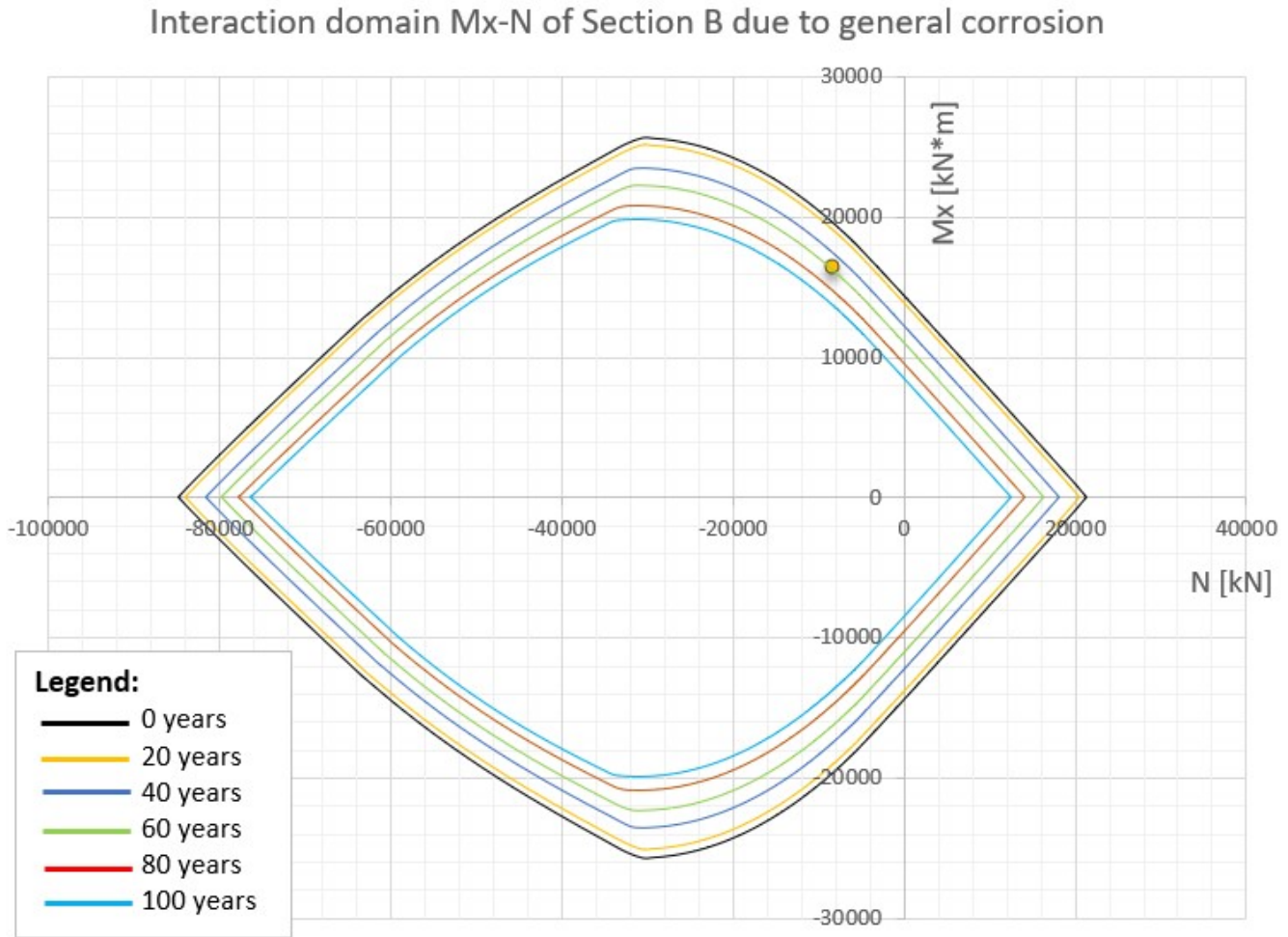


Figure 6.10: Interaction domain of Section B due to general corrosion

In this case Figure 6.10 shows a negative checking outcome.

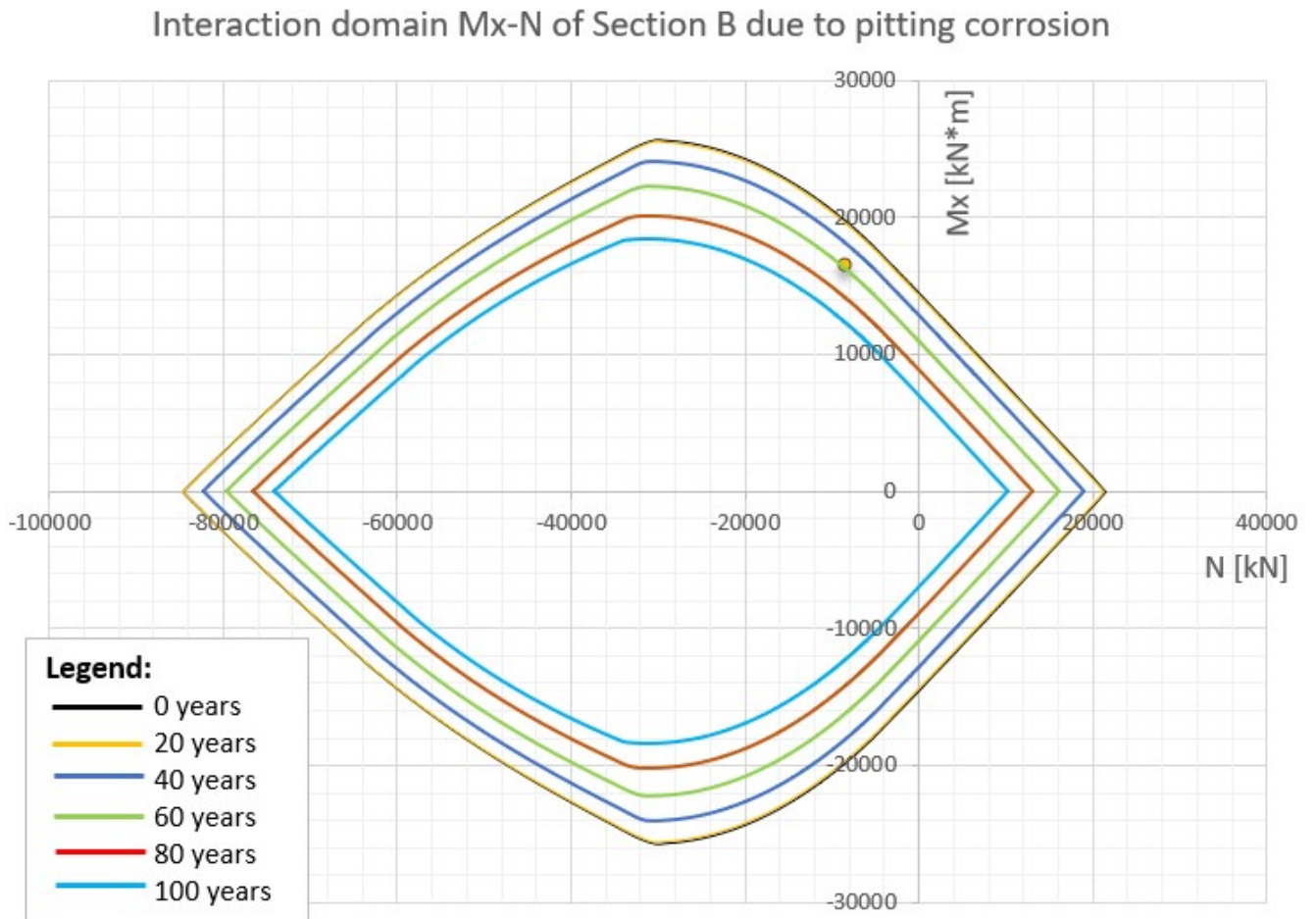


Figure 6.11: Interaction domain of Section B due to pitting corrosion

The pitting situation in Figure 6.11 illustrates a negative outcome such as in the case of general corrosion.

According to Figure 6.10 and 6.11, which show the situation regarding the applied couple $M_x - N$ in **Section B** due to both cases of general and pitting corrosion, a collapse is envisaged over time. This significant result, that has been tested here, aims to contribute to the improvement of bridge engineering. In fact, it shows that under these conditions the case study of **the bridge is expected to collapse after 50 years**, i.e. a period

corresponding to half of the total bridge service life (100 years).

Furthermore, there is also an important similarity between the two cases of corrosion. As can be seen from Figure 6.10 and 6.11, this depends on the fact that up to 60 years the reinforcement area loss is almost the same amount. In contrast, after this period the two models have different behaviours, because general corrosion is less harmful than pitting and it affects the whole longitudinal steel bar uniformly. Indeed, pitting regards a worse situation after 60 years and the area loss is greater.

Thus, the structure is more unsafe and seismic hazard is higher after 50 years of bridge service life. This is due to the fact that pitting corrosion affects steel reinforcement in a concentrated way leading to localized losses in reinforcing bar areas [4]. In this case, corrosion is localized in small areas of reinforcement but steel area loss quantity is bigger. As discussed in Chapter 3, pitting corrosion is assumed to take a hemispherical form that expands with time.

Moreover, pitting is more difficult to be noticed during an inspection because produces little rust staining on the concrete surface [4]. For this reason, an in-depth analysis of the degradation of this type of system is fundamental, together with the identification of the most appropriate time for restoration, in order to investigate the best solution.

This means that under normal conditions the bridge could easily withstand seismic action. On the other hand, when pitting corrosion occurs, the service life of the structure is less than the period planned at the beginning.

In addition, it is evident that failure occurs more quickly, because corrosion is aggravated if the structure is placed in a marine environment. For this reason, in this bridge case study the deterioration model regarding the distance from the sea has been taken into account. Indeed, RC columns exposed to the chloride environment inevitably suffer from the effect of chloride-induced corrosion. Consequently, this kind of corrosion can determine cracking or spalling of concrete cover and steel reinforcement volume expansion [13, 14].

The bridge failure occurs after about 50 years in Section B, because the bending moment is higher compared to Section A, due to the eccentricity of the Y-shaped pier arms that hold up the bridge deck. In fact, this also depends on the axial force, which is ($N = 8322 \text{ kN}$) more or less half of that at the base of the pier ($N = 18380 \text{ kN}$).

In addition, seismic action is accidental and it may not be predicted in a short time permitting bridge closing and evacuation of people. Thereby, the structure must be safe and reinforced to withstand this kind of events.

6.3 Combination of general and pitting corrosion analysis

Interaction domains, related to the combination of general and pitting case, are presented here in Figure 6.12-15 in order to check further the couple of the design point.

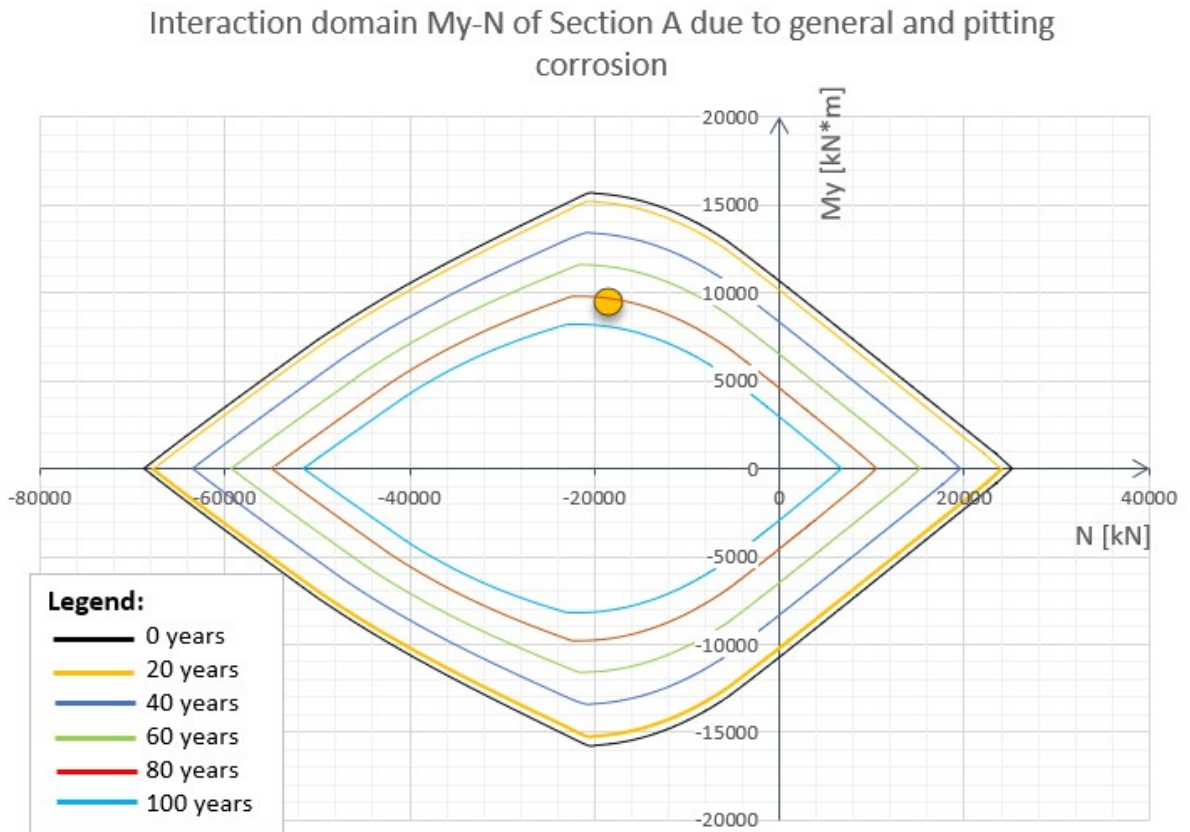


Figure 6.12: Interaction domain of Section A due to general and pitting corrosion

In this case Figure 6.12 shows a negative checking outcome.

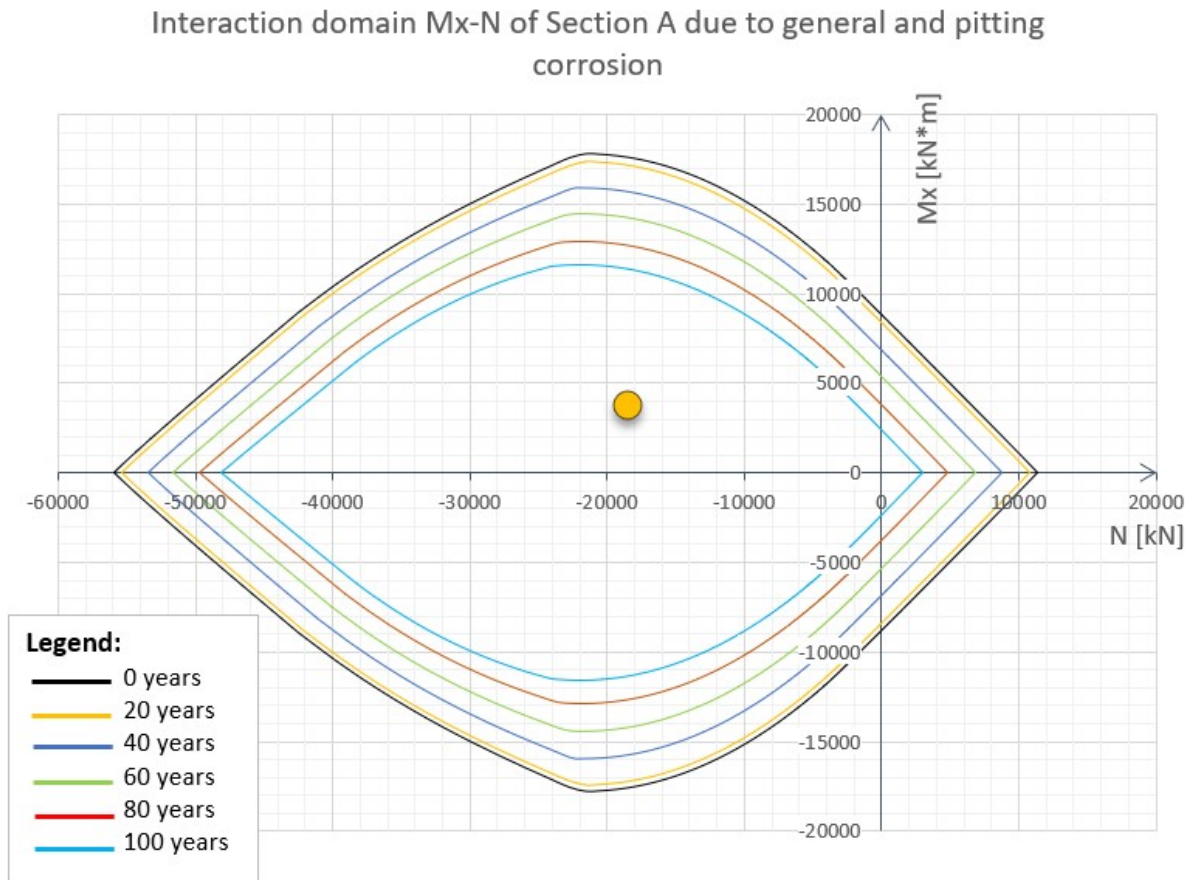


Figure 6.13: Interaction domain of Section A due to general and pitting corrosion

As shown in Figure 6.13, the point is checked positively.

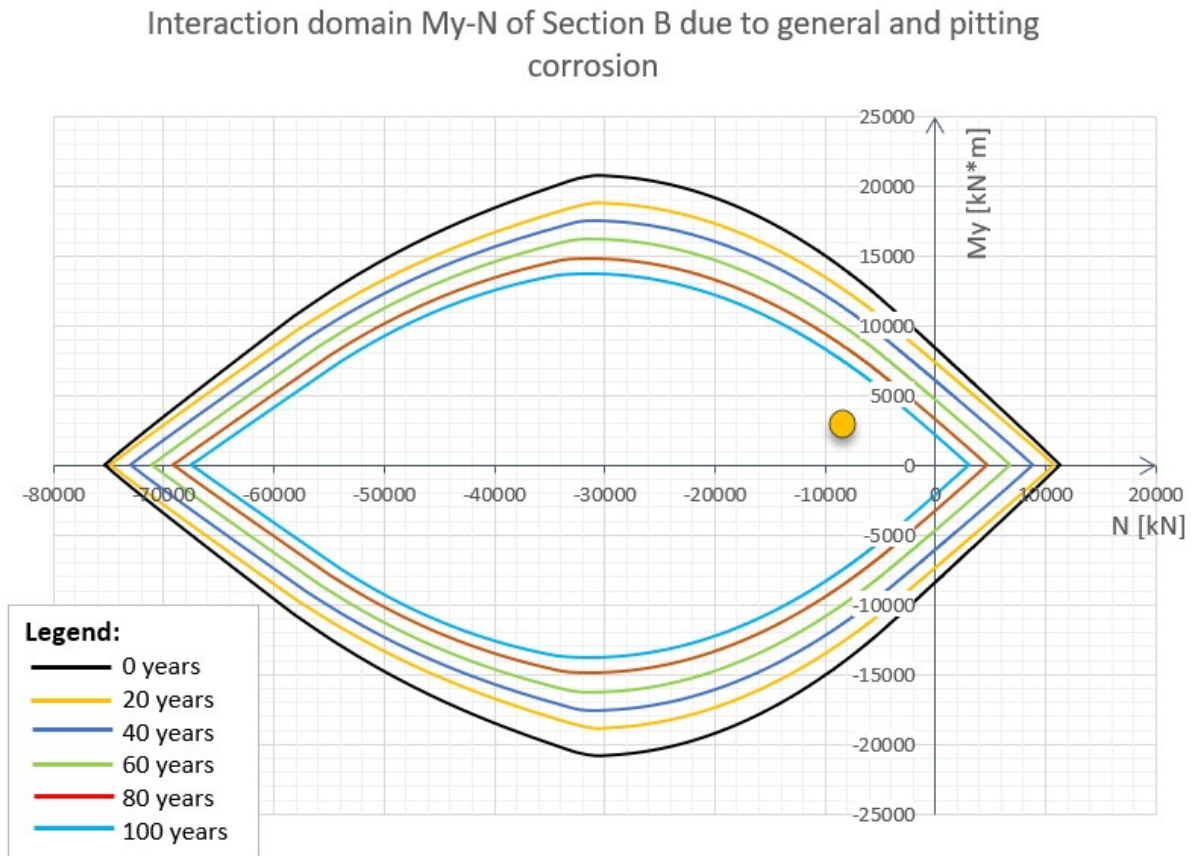


Figure 6.14: Interaction domain of Section B due to general and pitting corrosion

In Figure 6.14 the point is checked successfully.

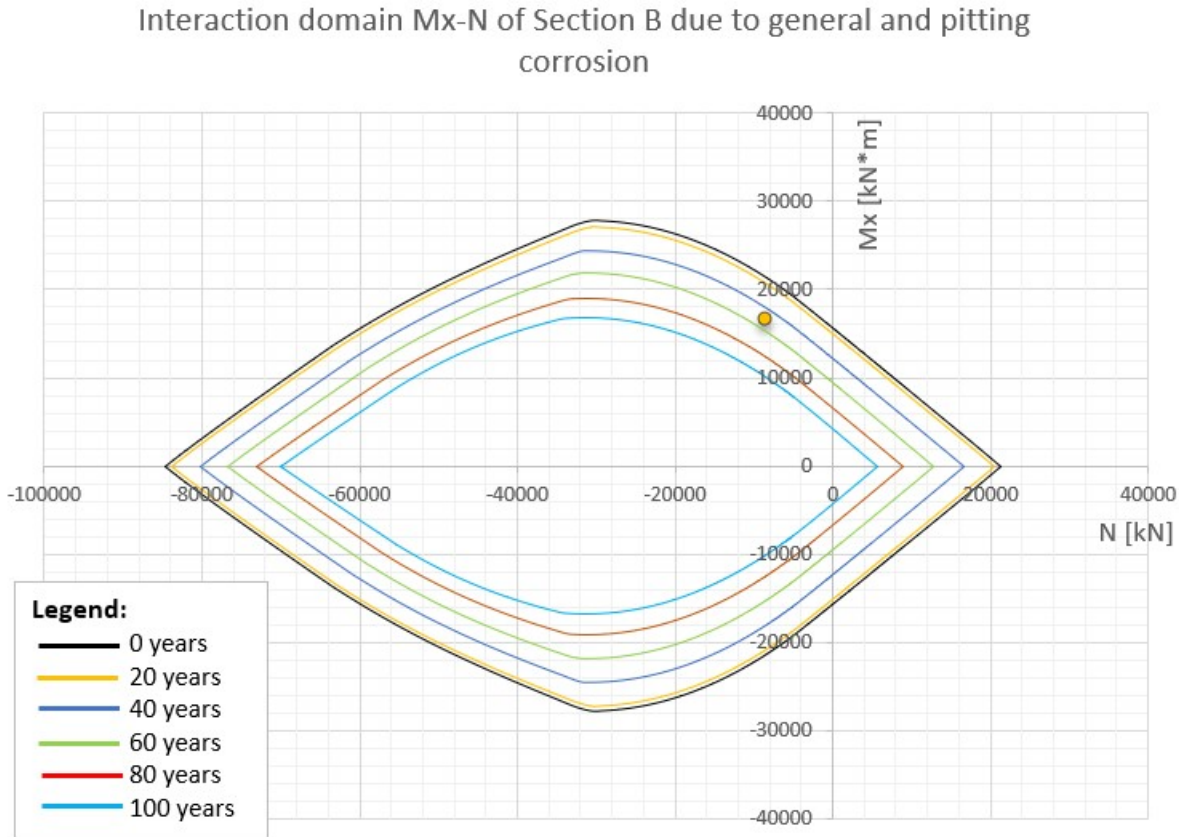


Figure 6.15: Interaction domain of Section B due to general and pitting corrosion

In this case Figure 6.15 shows a negative checking outcome.

As can be seen in Figure 6.12-15, the analysis of the combination of two corrosion effects confirms the findings reported above in Figure 6.4-11. In addition, here it has been found that under these conditions **Section A can fail after 80 years** due to general and pitting corrosion, as shown in Figure 6.12. This cross-section is placed at the base, that is the most significant zone of the bridge. Thus, the structure service life is less than the period established in the bridge design. This means that the bridge failure occurs prematurely due to general and pitting corrosion.

On the other hand, in Section B these results are consistent with data obtained in the case of general and pitting corrosion analyzed separately. Indeed, **the bridge is expected to**

collapse after 50 years, i.e. a period corresponding to half of the total bridge service life (100 years).

However, this study regarding the combination of two effects is considered more conservative, because the reinforcement area loss is uniform and hemispherical in the case of general and pitting corrosion, respectively. This accounts for an overlapping area loss which is not numerically computed here. This assumption is explained in Figure 6.16 which describes a steel bar subjected to both corrosion attacks.

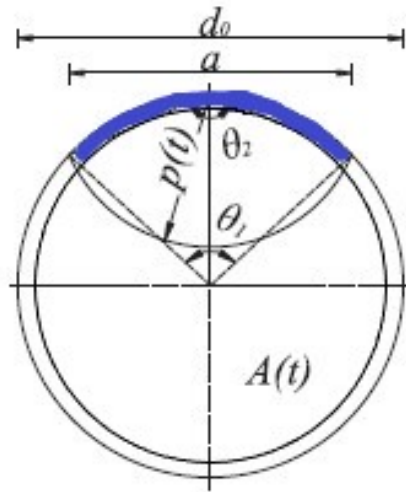


Figure 6.16: Overlapping area loss due to general and pitting corrosion

6.4 Bresler's domain

In order to complete the analysis of the pier, the biaxial bending condition assessment is required. This situation accounts for the simultaneous presence of three characteristics of load: N , M_x and M_y . The biaxial bending analysis is fundamental as a consequence of the

location of the bridge in seismic zone, thus the horizontal and vertical forces due to the earthquake can act simultaneously.

The strength of an RC pier is considered by means of Bresler's domain. That is, a safety domain such as the interaction domain, but with a different surface and constant value of axial force N , as shown in Figure 6.17 [45].

Specifically, it consists of an ellipse in which the semi-axes coincide with the resisting

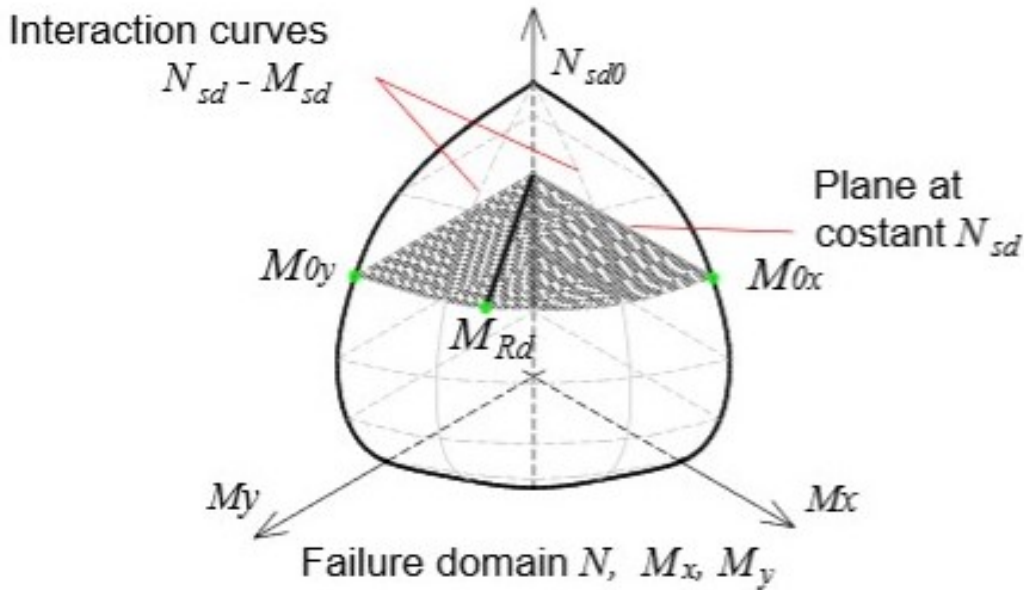


Figure 6.17: Interaction domain in the biaxial bending condition

bending moments in both directions ($M_{rdy} - M_{rdx}$). Each point of the resisting bending moment, M_{rd} , in Bresler's domain corresponds to the couple regarding the applied actions (N, M_x) or (N, M_y). M_{rd} has been obtained by the point in the interaction domain outline. Thus, Bresler's domains are given here only for the most relevant situations, e.g. the initial and final condition of the bridge case study. Blue and red lines refer to pitting and general corrosion, respectively, investigated at 100 years of service life. In contrast, the black line represents the initial state condition and the orange point indicates the coordinates of the design point.

Bresler's domain of Section A due to general corrosion, $t = 0-100$ years

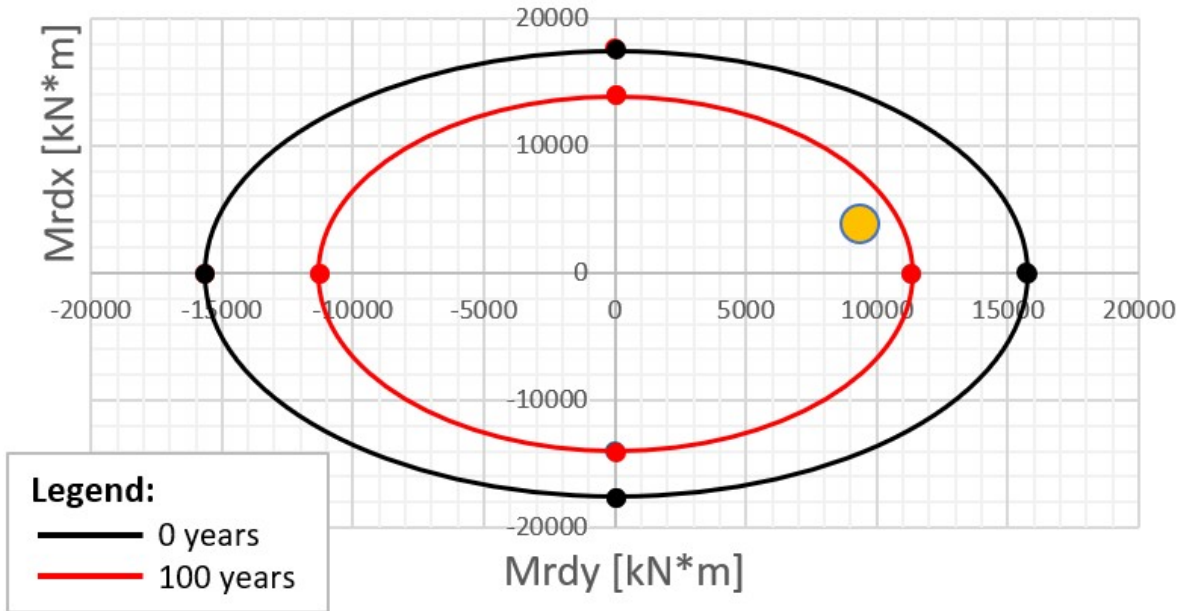


Figure 6.18: Bresler's domain of Section A due to general corrosion

Figure 6.18 shows that the orange point is inside the safety domain.

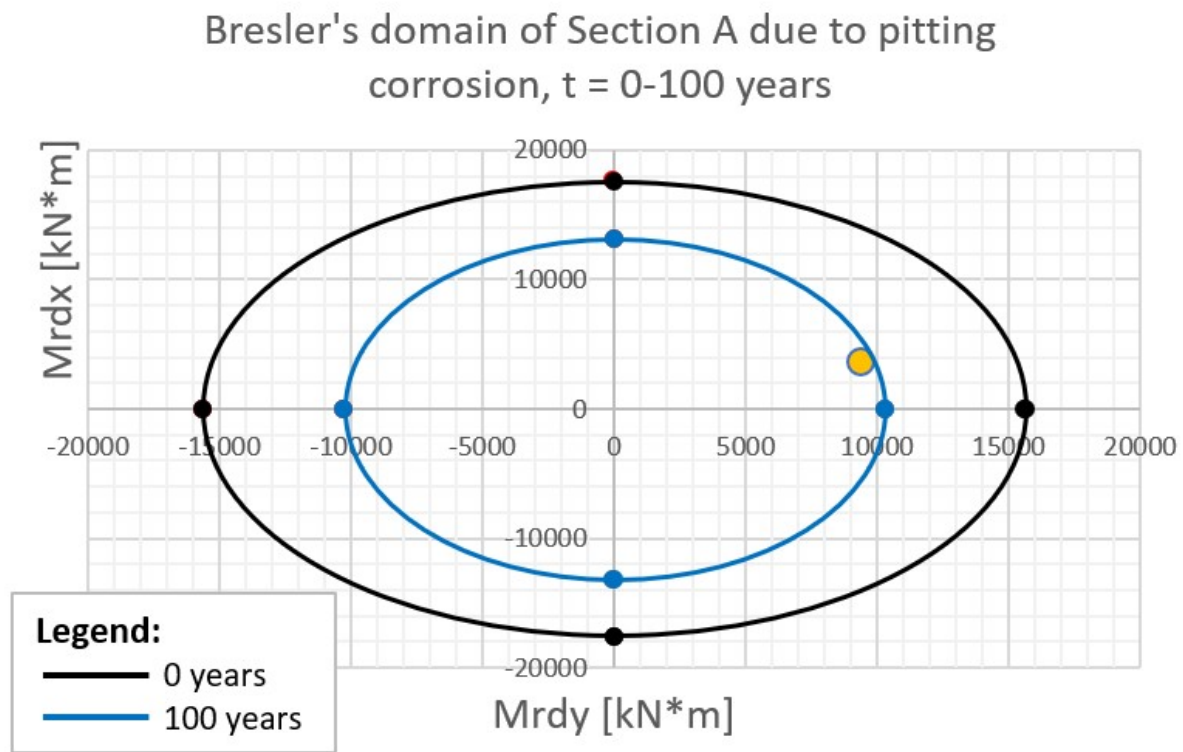


Figure 6.19: Bresler's domain of Section A due to pitting corrosion

As shown in Figure 6.19, the point is checked positively.

Bresler's domain of Section B due to general corrosion, $t = 0-100$ years

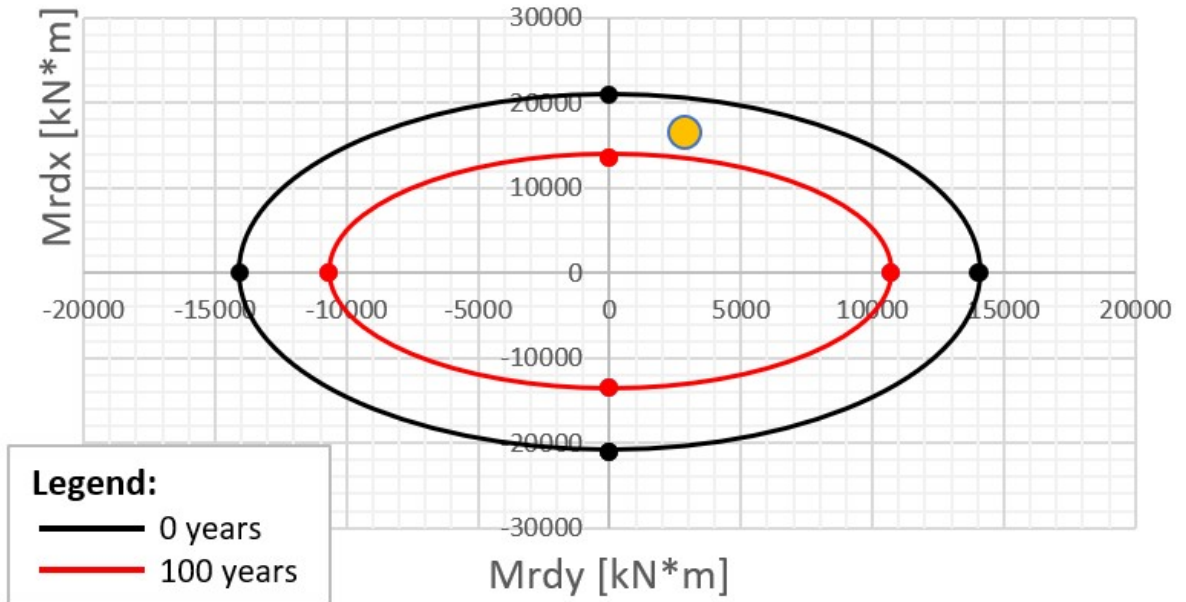


Figure 6.20: Bresler's domain of Section B due to general corrosion

In this case Figure 6.20 shows a negative checking outcome.

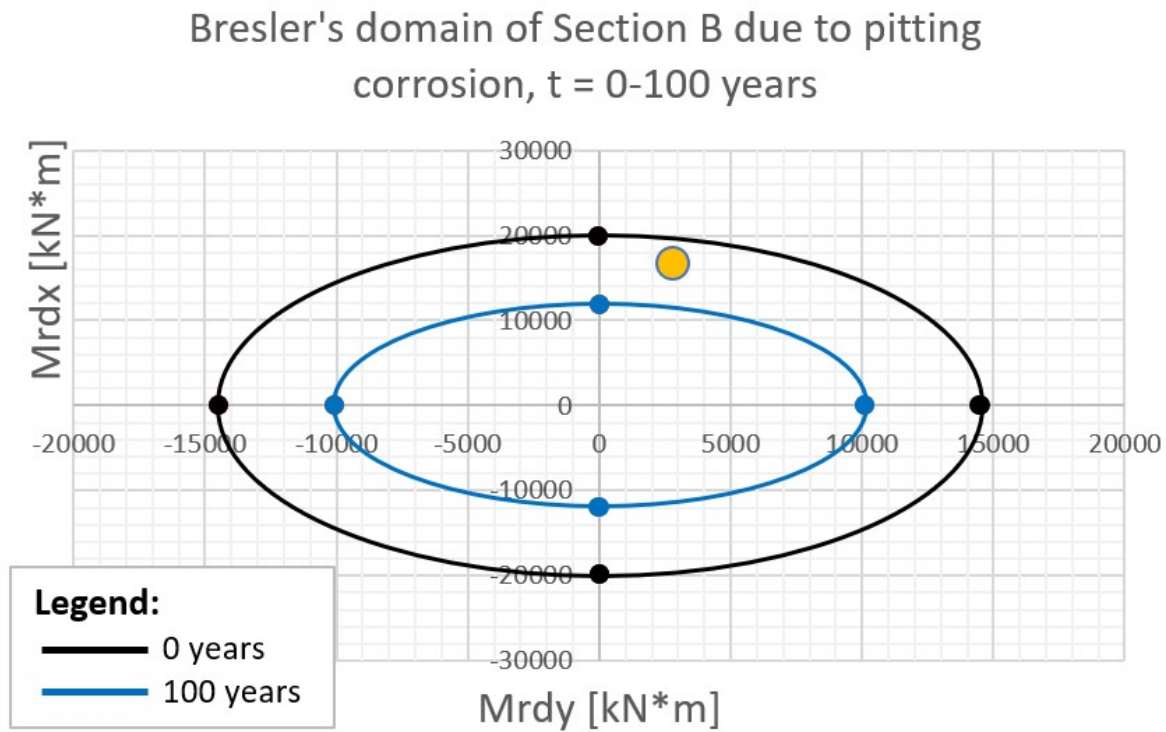


Figure 6.21: Bresler's domain of Section B due to pitting corrosion

Figure 6.21 illustrates a negative outcome such as in the case of general corrosion.

Bresler's domain of Section A due to general and pitting corrosion, $t = 0-100$ years

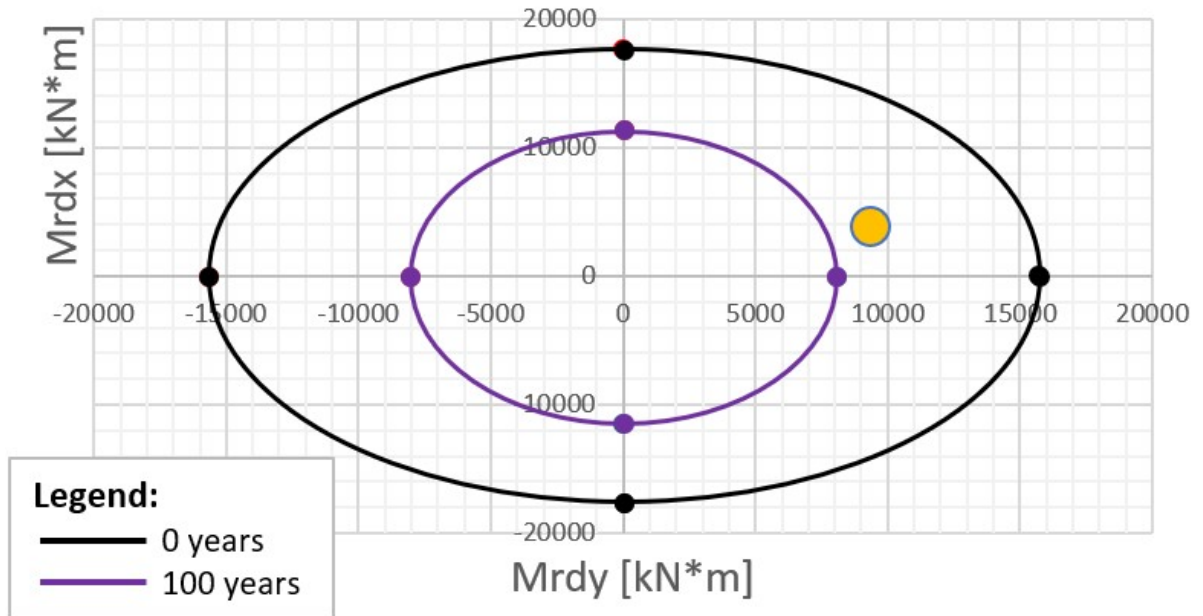


Figure 6.22: Bresler's domain of Section A due to general and pitting corrosion

Figure 6.22 illustrates a negative outcome, because the orange point is outside the safety domain. This depends on the combination of two corrosion forms which determine the bridge failure in Section A, as well, before reaching the established period of service life.

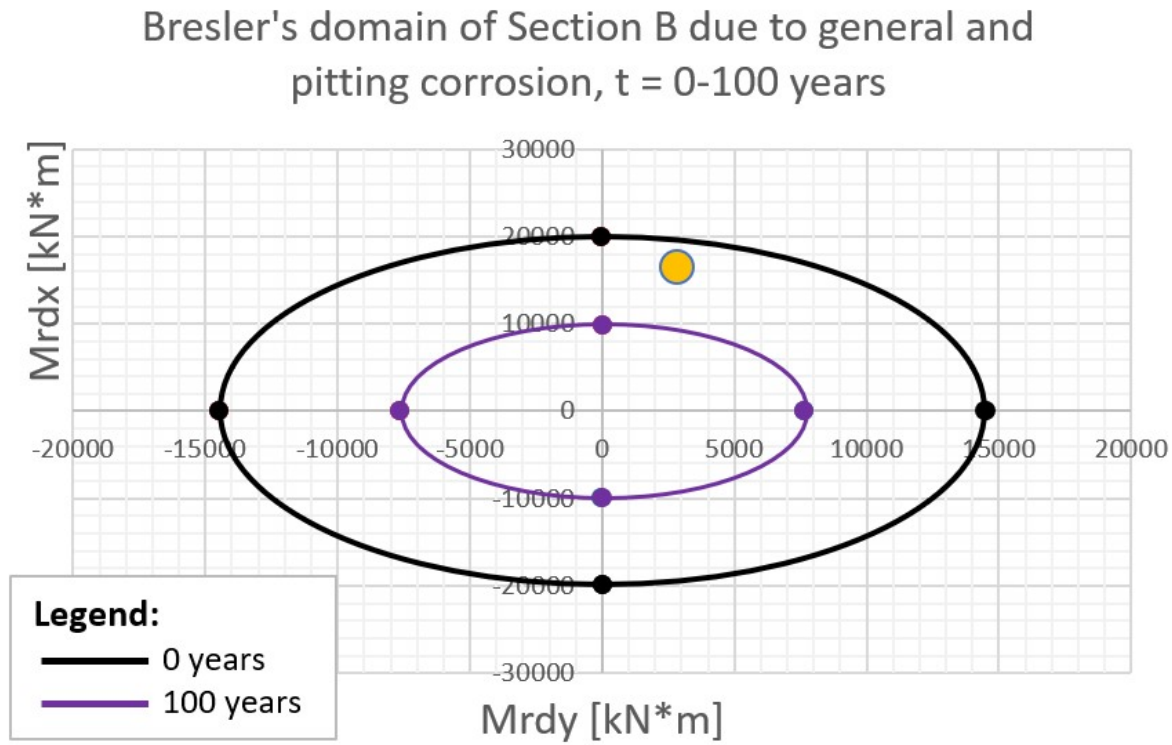


Figure 6.23: Bresler's domain of Section B due to general and pitting corrosion

Figure 6.23 illustrates a negative outcome such as in the case of interaction domains.

As can be seen from Figure 6.18-23, these results are clearly in agreement with those obtained by the interaction domains. These relationships may partly be explained by the fact that the resisting bending moment has been found by means of the interaction domain. Therefore, this is further evidence of the degradation and collapse of the structure before reaching its intended service life time limit.

6.5 Limitations of the presented approach

The presented study is focused on the ductility and area loss of steel reinforcement with time. The findings from this study suggest that corrosion can have a strong effect on duc-

ility performance of the structure. Moreover, corrosion can affect bonding as well, and reduce ductility performance increasingly due to bonding failure.

Bridge design details are also based on bond strength and confinement capacity of the reinforcing bars. However, in a corroded structure bond strength and confinement capacity can decrease due to the transverse reinforcement area loss. Although all ductility requirements were respected through the design details, as discussed in Chapter 4 [37], bond strength ductility requirements are beyond the scope of the present investigation and were not considered in the study. Future research could usefully investigate bonding failure effects in bridge corrosion processes.

Another issue could be explored by future research is the variation of internal forces throughout the service life of a bridge due to corrosion. After some level of corrosion, concrete spalling produces a smaller cross-section, which translates into reduced inertia and stiffness. As this stiffness reduction may not be homogeneous in the whole structure, a redistribution of internal forces due to external forces can appear. This means that these internal forces can change with time. The other consequence of concrete spalling can also produce a reduction in response capacity due to the loss of concrete in the structural element. Response capacity is a fundamental requirement to support compressive strength.

However, all these aspects could be investigated and analyzed in further studies to assess bridges maintenance.

Chapter 7

Retrofitting

As discussed in Chapter 6, the structure must be demolished after about 50 years, because the service life of the bridge ends. An example is shown in Figure 7.1, where a flexural failure above the columns base of the Hanshin expressway is reported. This failure occurred due to premature termination of longitudinal reinforcement and inadequate confinement during the 1995 Kobe earthquake event [46]. By contrast, a retrofitting strategy may be applied in situations in which the structure can survive from a structural and economic point of view. Retrofitting is the modification of existing equipment or structures with additional or new components or members [46].

Seismic retrofitting is a result of new technology development. This strategy is useful to make old bridges resistant to earthquakes, and it also helps in cost reduction. Constructing a new bridge is always a time and resource consuming practice. After a detailed seismic performance evaluation, as in the case of the present investigation, retrofitting can be performed on old or weak bridges using methods such as friction damper systems, carbon fiber plastic reinforcements, and external prestressing, as well as improving soil properties to keep a check on ground motion. Seismic retrofitting is a relatively new technique. Consequently, Civil Engineering societies and associations across the world are promoting it because this strategy can save money, time, and resources, without compromising reliability and safety [46].

Thus, following the decision to implement retrofitting, the second step regards the level to which the bridge should be retrofitted. This depends on a cost-benefit analysis. This type of analysis is rather inaccurate, where the presence of errors is high due to the assessment of retrofit-level earthquake [46]. The probability of exceedance of the ultimate limit state should be the same for both retrofitted and new bridge.



Figure 7.1: Flexural failure above the columns base of the Hanshin expressway during 1995 Kobe earthquake

7.1 Overview of seismic retrofit approaches

Generally, the main seismic retrofit approaches, described in Figure 7.2, include: seismic isolation, longitudinal and transverse restrainers, seat extenders, column strengthening, and bent cap strengthening. These methods of retrofit can be applied individually or in combination, in order to reduce the bridge overall vulnerability to seismic action [47].

The benefits of seismic isolation bearings are to move the natural frequency of the structure out of the region of dominant earthquake energy, to increase damping in the structure, and finally, to decrease the dynamic reactions between the bridge superstructure and substructure [48]. In addition, the most common seismic isolators are elastomeric bearings, such as those used in the design of the bridge case study, and slider bearing isolation systems.

Longitudinal bars and cable restrainers (Figure 7.3) are good illustrations of seismic retrofitting. The function of restrainers is to prevent intense longitudinal movement of bridge spans. Restrainer cables are usually made of 19 mm diameter steel cables with lengths between 1.52 m and 3.05 m.

Another useful example of retrofit approaches consists of seat extenders, which are applied

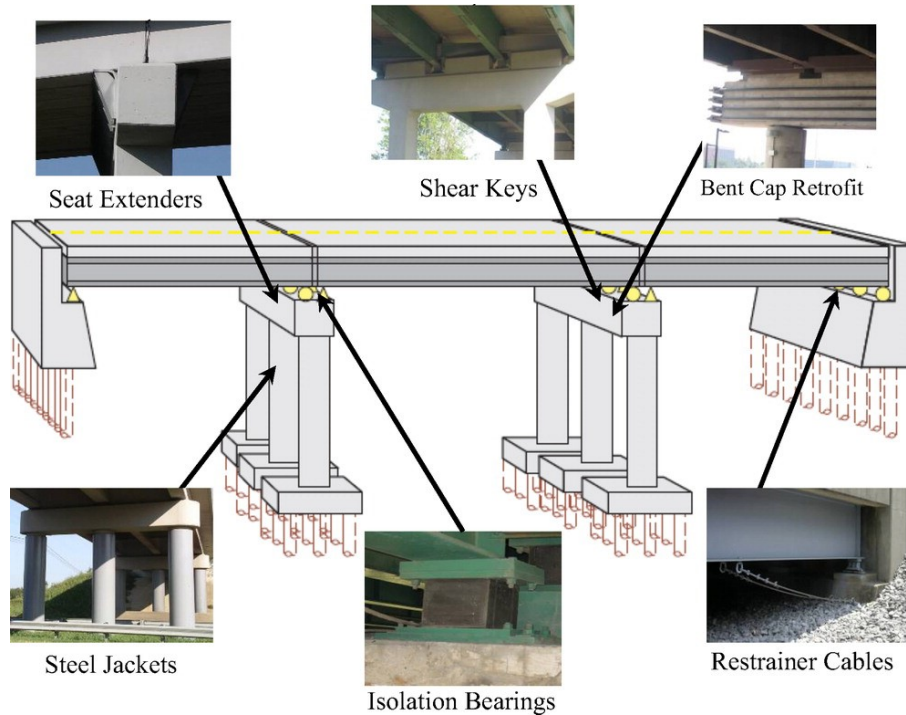


Figure 7.2: Representation of seismic retrofit approaches in a bridge [47]

to abutments by means of concrete corbels or structural steel brackets. These elements aim to increase the seat length of the span and decrease the possibility to unseating of a bridge span.

The main purpose of transverse retrofitting is to prevent intense transverse movement of the bridge deck during earthquakes in the event of bearing failure. The most common application consists of shear keys, i.e. reinforced concrete blocks attached to the bent beams with dowels. Shear keys are useful instruments used to transmit lateral forces from the superstructure to the substructure. This means that the demand in the substructure components increases due to the addition of lateral force. This issue can be solved designing shear keys in order to fail at a given force level by avoiding the excessive force transmitted to the substructure. Experimental studies have shown that shear keys are suitable retrofit applications for multi-span continuous steel girder bridges [49].

A further seismic retrofit approach is based on bent cap retrofits. Bent caps are used to transmit loads from the bearings of a bridge to the columns. The mechanism consists in the increase of flexural and shear strength in bent caps, in order to have a plastic hinge

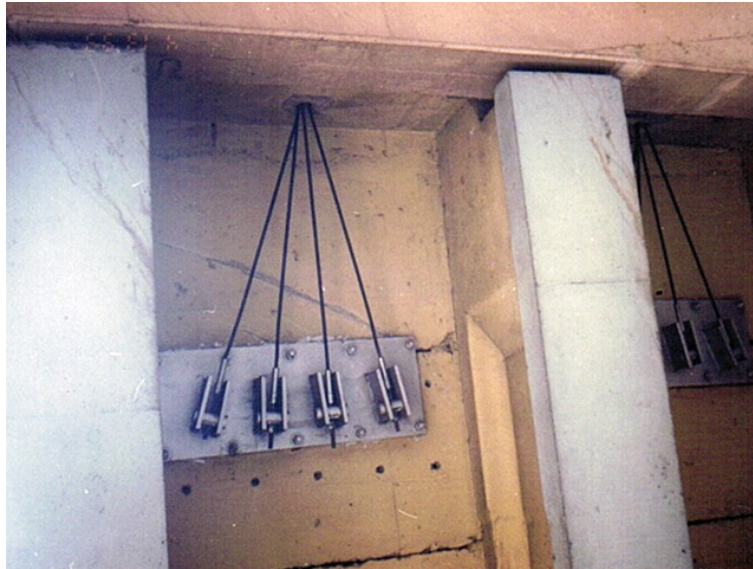


Figure 7.3: Representation of cable restrainers

which occurs first in columns instead of bent caps. This can be possible by means of posttensioned rods, external shear reinforcement, or through the addition of a concrete or steel bolster. A common way to increase shear strength is to apply shear reinforcement externally on the bent cap. Steel plates are located along the top and bottom side of the bent beam. The plates are connected with metal rods in order to improve the shear performance of the bent cap in the bridge [47].

7.2 Retrofit of concrete columns

Columns are among the most demanding structural elements of a bridge. Low ductility capacities and inadequate transverse reinforcement can lead to a failure. In order to prevent failure, retrofitting strategies are necessary to improve the confinement for concrete columns increasing ductility and lap splice performance [47].

A well-known example of columns retrofitting regards steel jacketing, used to increase flexural ductility and shear strength of columns. Figure 7.4 describes the details of a typical full column steel jacket. It can be applied in full or partial column height, as shown in Figure 7.5. The minimum recommended shell thickness of a steel jacket is 9.5 mm and the maximum thickness should not exceed 25 mm [50]. The steel jacketing procedure was originally applied on circular columns. It consists of two half shells of steel plate, placed around the column area to be retrofitted in order to provide a small annular gap around the column. Successively, this gap is grouted with a pure cement grout, after flushing

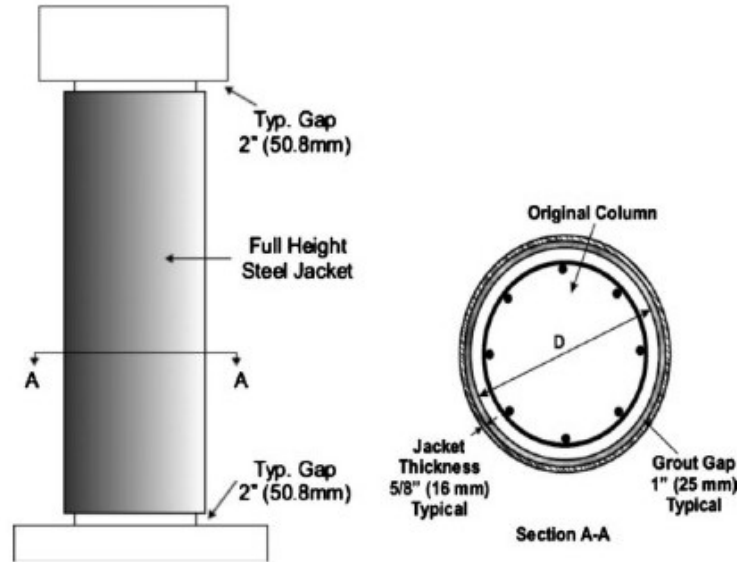


Figure 7.4: Details of a typical full column steel jacket [47]

with water [46]. This provides an appropriate efficiency in passive confinement, which it mainly depends on the hoop strength and stiffness of the steel jacket. The effectiveness of the steel jacketing technique has been exemplified in a study by Priestley et al. [46]. Here, an increase in column stiffness by approximately 20-40% was obtained for the case of full height jackets. The recommended approach regarding rectangular columns is shown in Figure 7.6, i.e. the use of an elliptical jacket that provides an effect similar to that for circular columns. The difference regards the space between the jacket and column, filled with normal unmodified concrete rather than grout. In contrast, rectangular steel jackets on rectangular columns are not recommended. Concrete overlays can be used in combination with a steel jacket and an external reinforcement around the column. Figure 7.7 illustrates this condition.



Figure 7.5: (a) Full column steel jacketing used in Tennessee, (b) partial height steel jacketing in Missouri focusing in plastic hinge regions of the columns [47]

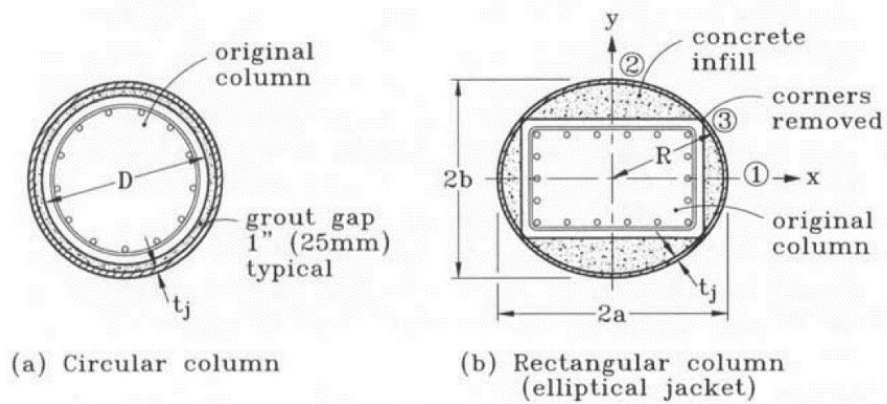


Figure 7.6: Confinement of columns by steel jacketing [46]



Figure 7.7: Concrete overlays along with an external reinforcement around the column [47]

Another remarkable application regarding column retrofitting concerns jackets of composite materials such as fiberglass, carbon fiber, and Kevlar, generally bonded together and to the column with epoxy. Carbon fiber has a greater strength and stiffness compared to the other materials.

7.3 Cost analysis overview

A retrofitting strategy may be applied in situations in which the structure can survive from a structural and economic point of view. An estimation of the retrofitting strategy cost is required by public authorities to evaluate if retrofitting is better than demolishing the bridge [51]. This can be seen in the case reported by Pellegrino et al. [52], in which a procedure for bridge maintenance management is discussed. The method regards a visual inspection, carried out for the structural and non-structural components of bridges, in order to estimate the *Total Sufficiency Rating* (TSR) parameter, a global qualitative indicator of the “state of health” of each bridge. This parameter computation involves the *Condition Value* (CV) of each element in the bridge. The CV represents a condition depending on a couple of defects of the element for which it is estimated. A CV value can be defined from 1 to 5 for each component of a bridge; if no evaluation can be expressed, CV is null. Each CV value corresponds to a monetary cost expressed in € per metre linear.

Therefore, the total maintenance costs are defined as the sum of each bridge element

cost and an average value regarding 1 m^2 of bridge deck can be computed as follows:

$$Unit\ maintenance\ cost = \frac{Total\ maintenance\ cost}{Deck\ area} \quad (7.1)$$

Moreover, the TSR of the whole structure is calculated by means of Equation (7.2).

$$TSR = \frac{100 \cdot TSR_{real} + TSR_{min} \cdot CoF}{100 + CoF} \quad (7.2)$$

TSR_{real} is a parameter obtained by Equation (7.3), TSR_{min} is estimated assuming CV=5 (representing the worst situation) for all components not assessed, and Confidence Factor (CoF) is derived by Equation (7.4), in which t is the number of elements examined, n is the total number of elements in the bridge structure, and W_i the weight of structural and non-structural components.

$$TSR_{real} = 10 \cdot (RT \cdot TI \cdot NBI \cdot AF) \frac{\sum_{i=1}^t CF_i \cdot W_i}{\sum_{i=1}^t W_i} \quad (7.3)$$

$$CoF = 100 \frac{\sum_{i=1}^t W_i}{\sum_{i=1}^n W_i} \quad (7.4)$$

The parameters presented in Equation (7.3) are defined as follows: RT is the road type factor, TI the traffic index factor (daily traffic volume), NBI the network bridge importance factor (effect of bridge closure on user costs), and AF the age factor (ageing). In this way, TSR value can be estimated in order to find the state of maintenance of the structure.

Finally, it is evident that building a new bridge usually requires more time and money than rehabilitating and retrofitting an existing bridge for its recycling. Thus, this method can be useful to prevent the cost maintenance of the bridge in order to preserve and improve the structure.

Conclusions

The aim of the present research was to examine the effects of corrosion and seismic action on an RC pier of a highway overpass. The bridge is located in Sicily, that is a highly seismic zone in a marine environment. Previous research performed by Cui et al. was followed, changing the deterioration input parameters according to the bridge site. Thus, general and pitting corrosion analysis was applied to steel reinforcing bars obtaining the residual cross-sectional area of reinforcement. A combination of general and pitting corrosion effects was considered as well. This study has found that this combination generally represents the most demanding case. In fact, interaction and Bresler's domains show that a collapse is envisaged over time. It is shown that under these conditions the bridge is expected to collapse after about 50 years, i.e. a period corresponding to half of the total bridge service life (100 years).

Due to the unpredictability of the seismic event and the resulting impossibility to completely avoid hazard at the site, this study proposes a methodology that may be useful to predict the degradation of the seismic capacity of a common infrastructure such as a highway overpass. This methodology takes into account corrosion and performance losses when designing a bridge in order to prevent abrupt collapse and ensure reasonable durability. A bridge that does not suffer from corrosion can easily withstand seismic action. On the other hand, when pitting corrosion occurs, the service life of the structure is shorter than the period planned at the beginning. If the structure is placed in a marine environment, failure occurs more quickly because corrosion is aggravated. The deterioration model applied in this bridge case study takes into account the distance from the sea. Thus, this thesis aims to contribute to the improvement of bridge engineering.

A retrofitting strategy can be applied when the structure can survive from a structural and economic point of view. This strategy can be useful to make old bridges resistant to earthquakes if applied at the most appropriate time for restoration (50 years), and it also helps in cost reduction. It is evident that building a new bridge usually requires more time and money than rehabilitating and retrofitting an existing bridge for its recycling. This involves the possibility of controlling the seismic risk and therefore of being able to close or plan the infrastructure maintenance in time.

An uncontrolled factor in the study is that corrosion can affect bonding, thus increasingly reducing ductility performance. Bridge design details are also based on bond strength and confinement capacity of the reinforcing bars. However, in a corroded structure bond strength and confinement capacity can decrease due to the transverse reinforcement area loss. Although all ductility requirements were respected through the design details, as discussed in Chapter 4, bond strength ductility requirements are beyond the scope of the present investigation and were not considered in the study. Future research could usefully investigate bonding failure effects in bridge corrosion processes.

Another issue could be explored by future research is the variation of internal forces throughout the service life of a bridge due to corrosion. After some level of corrosion, concrete spalling produces a smaller cross-section, which translates into reduced inertia and stiffness. As this stiffness reduction may not be homogeneous in the whole structure, a redistribution of internal forces due to external forces can appear. This means that these internal forces can change with time. The other consequence of concrete spalling can also produce a reduction in response capacity due to the loss of concrete in the structural element. Response capacity is a fundamental requirement to support compressive strength. The present thesis makes an important contribution to corrosion prevention and a better understanding of variation of internal forces merits attention in order to further develop bridge engineering.

Appendix A

Matlab script

Matlab script regarding the corrosion model applied to the bridge case study in the thesis is reported as follows.

```
1 clear all
2 close all
3 clc

5 %input parameters paper
6 X_1=1;
7 k_e=1;
8 k_t=0.85;
9 k_c=1.5;
10 D_0=220.9;
11 t_0=0.0767; %years, equal to 28 days
12 n=0.25;
13 d_c=50; %mm
14 d_0=32; %mm
15 f_cu=40; %MPa
16 f_0=450; %MPa
17 A_cs=1.084; %atmospheric zone, 1 km distance from coastline
18 w_c=0.4; %w/c=0.4, water/cement ratio
19 C_0=A_cs*w_c;
20 C_cr=0.8; %constantly humid
21 R=7.1;
22 delta_t=0.03;
23
```

APPENDIX A. MATLAB SCRIPT

```

%definition of corrosion initiation time
25 t_corr= X_1*(((d_c^2)/(4*k_e*k_t*k_c*D_0*(t_0)^n))*(erfinv(1-(
    C_cr/C_0))))^(-2))^(1/(1-n)); %corrosion initiation time in
    years

27 i_corr=(37.8*(1-w_c)^(-1.64))/d_c; %corrosion current density

29 % determination of initial cracking time t_cr
    p_cr= 0.012*d_c/d_0+0.00084*f_cu+0.018;
31 t_cr=((p_cr*d_c)/(0.52494*(1-w_c)^(-1.64)))^1.40845+t_corr; %
    cracking time in years

33 %determination of severe cracking time t_wcr in years
    t_wcr=t_cr+6.4;

35
%different expressions of lambda function related to the time
37 fun_lambda_1 = @(x) 0.0116.*i_corr.*0.85.*(x-t_corr).^(-0.29);
    fun_lambda_3 = @(x) (4.5-26.*fun_lambda_1(x)).*fun_lambda_1(x);
39 fun_lambda_2 = @(x) (x-t_cr).*((fun_lambda_3(t_wcr)-fun_lambda_1(
    t_cr))./(t_wcr-t_cr))+fun_lambda_1(t_cr);

41 %definition of lambda function
    time = (t_corr+delta_t):delta_t:100;

43
for i=1:length(time);
45     t = time(i);
        if (t>t_cr) & (t<=t_wcr)
47         fun_lambda = fun_lambda_2;
        elseif (t>t_corr) & (t<=t_cr)
49         fun_lambda = fun_lambda_1 ;
        elseif (t>t_wcr)
51         fun_lambda = fun_lambda_3;
        end
53     lambda(i) = fun_lambda(t);
end

55
    lambda(lambda==0) = nan;

57
%plot lambda function
59 figure
    x1=time;

```

```

61 plot(x1,lambda,'color',[0 0.5 0],'linewidth',2.5)
   grid on
63 ylim([0 0.06]);
   xlim([0 100]);
65 title('Corrosion_rate_curve_in_atmospheric_zone');
   xlabel('Time_(years)');
67 ylabel('Corrosion_Rate_(mm/a)');

69
   %% general corrosion model
71
   time_1 = (t_corr+delta_t):delta_t:t_cr;
73
   for i=1:1:length(time_1)
75       t = time_1(i);
           fun_lambda = fun_lambda_1;
77       d_t_1(i) = integral(fun_lambda,t_corr,t); %residual
           reinforcement diameter part 1

79 end
       d_t_1_end = d_t_1(end);
81
   time_2 = (t_cr+delta_t):delta_t:t_wcr;
83
   for i=1:1:length(time_2);
85       t = time_2(i);
           fun_lambda = fun_lambda_2;
87
           d_t_2(i) = integral(fun_lambda,t_cr,t); %residual
           reinforcement diameter part 2
89 end
       d_t_2 = d_t_1_end + d_t_2;
91 d_t_2_end = d_t_2(end);

93 time_3 = (t_wcr+delta_t):delta_t:100;

95 for i=1:1:length(time_3);
97       t = time_3(i);
           fun_lambda = fun_lambda_3;

99       d_t_3(i) = integral(fun_lambda,t_wcr,t); %residual

```

reinforcement diameter part 3

```
101 end
      d_t_3 = d_t_2_end+d_t_3;
103
      d_t = d_0-2*[d_t_1 , d_t_2 , d_t_3];
105 d_t = horzcat(zeros(ceil(t_corr/delta_t),1)',d_t);
      A_gen = pi/4 .* (d_t).^2; %residual cross-sectional area of
          reinforcement
107
      A_gen(A_gen==0) = pi/4*d_0^2;
109 x2 = linspace(0,100,length(A_gen));

111 %plot figure
      figure
113 plot(x2,A_gen,'r','linewidth',2.5) %plot residual cross-sectional
          area due to gen. corr.
      ylim([350 850]);
115 grid on
      title({'Reduction_in_cross-sectional_area_of_steel_bars'; 'along_'
          'service_life_due_to_{\color{red}general_corrosion}'});
117 xlabel('Time_(years)');
      ylabel('Steel_Cross-section_Area_(mm^2)');
119

121 %% pitting corrosion model

123 time_1 = (t_corr+delta_t):delta_t:t_cr;

125 for i=1:1:length(time_1)
      t = time_1(i);
127      fun_lambda = fun_lambda_1;
      p_t_1(i) = R*integral(fun_lambda,t_corr,t); %pitting depth
          calculation part 1
129
end
131 p_t_1_end = p_t_1(end);

133 time_2 = (t_cr+delta_t):delta_t:t_wcr;

135 for i=1:1:length(time_2);
```

```

137     t = time_2(i);
        fun_lambda = fun_lambda_2;

139     p_t_2(i) = R*integral(fun_lambda , t_cr , t);  %pitting depth
        calculation part 2

141 end
    p_t_2 = p_t_1_end + p_t_2;
143 p_t_2_end = p_t_2(end);

145 time_3 = (t_wcr+delta_t):delta_t:100;

147 for i=1:1:length(time_3);
    t = time_3(i);
149     fun_lambda = fun_lambda_3;

151     p_t_3(i) = R*integral(fun_lambda , t_wcr , t);  %pitting depth
        calculation part 3

153 end
    p_t_3 = p_t_2_end+p_t_3;

155
    p_t = [p_t_1 , p_t_2 , p_t_3];
157
    %definition of parameters of area
159 a= 2.*p_t.*sqrt(1-(p_t./d_0).^2);
    theta_1= 2.*asin(a/d_0);
161 theta_2= 2.*asin(a./(2.*p_t));
    theta_2(isnan(theta_2))=0;
163 A_1= 0.5*(theta_1.*(d_0/2)^2-a.*abs(d_0./2-(p_t.^2)./d_0));
    A_2= 0.5*(theta_2.*(p_t).^2-a.*((p_t.^2)./d_0));
165
    %calculation of residual area due to pitting
167 A_pit_1= (pi/4*d_0^2)-A_1-A_2;
    A_pit = horzcat(zeros(ceil(t_corr/delta_t),1) , A_pit_1);
169 A_pit(A_pit==0) = pi/4*d_0^2;
    x3 = linspace(0,100 ,length(A_pit));
171
    %plot figure
173 figure
    plot(x3,A_pit , 'b' , 'linewidth' , 2) %plot residual cross-sectional

```

```
    area due to pit. corr.
175 xlim([0 100]);
    ylim([350 850]);
177 grid on
    title({'Reduction_in_cross-sectional_area_of_steel_bars'; 'along_
        service_life_due_to_{\color{blue}pitting_corrosion}'});
179 xlabel('Time_(years)');
    ylabel('Steel_Cross-section_Area_(mm^2)');
181

183 %plot comparison cross-sectional area due to gen. corr. and pit.
        corr.
    figure
185 plot(x3,A_pit,'b','linewidth',2)
    xlim([1 100]);
187 ylim([350 850]);
    hold on
189 plot(x2,A_gen,'r','linewidth',2)
    grid on
191 title('Comparison_between_{\color{blue}pitting}_and_{\color{red}
        general}_corrosion');
    xlabel('Time_(years)');
193 ylabel('Steel_Cross-section_Area_(mm^2)');

195
    %% yield steel strength loss model
197
    A_0= pi/4*d_0^2;
199 Q_corr= ((A_0-A_pit)/A_0)*100; %percentage of area loss
    f_t= (1-0.005*Q_corr)*f_0;
201 x4= linspace(0,100,length(f_t));

203 figure
    plot(x4,f_t,'k','linewidth',2) %plot yield strength loss curve
205 ylim([200 500]);
    grid on
207 title('Reduction_in_yield_strength_of_steel_bars');
    xlabel('Time_(years)');
209 ylabel('Steel_Yield_Strength_(MPa)');

211
```

```

%% ultimate steel strain loss model
213 epsilon_0= 0.0675;
215 epsilon_t= (1-0.0137*Q_corr)*epsilon_0;
x5= linspace(0,100,length(epsilon_t));
217
figure
219 plot(x5,epsilon_t,'k','linewidth',2) %plot ultimate steel strain
      loss curve
      ylim([0 0.08]);
221 grid on
      title('Reduction_in_ultimate_strain_of_steel_bars');
223 xlabel('Time_(years)');
      ylabel('Steel_Ultimate_Strain(-)');
225
%% combination of general and pitting corrosion
229 x6=[0,10,20,30,40,50,60,70,80,90,100];
      A_gen_pit=[804,798,766,712,654,593,530,465,400,334,268];
231
figure
233 plot(x6,A_gen_pit,'Color',[.5 0 .5],'linewidth',2) %plot
      combination of general and pitting corrosion
      ylim([150 850]);
235 grid on
      title({ 'Reduction_in_cross-sectional_area_of_steel_bars'; 'along_
      service_life_due_to_the_combination_of' ;
237           '\color{red}general' and '\color{blue}pitting' }_corrosion ');
xlabel('Time_(years)');
239 ylabel('Steel_Cross-section_Area_(mm^2)');

```

Ringraziamenti

Desidero ringraziare tutti coloro che mi hanno sostenuto nella stesura della tesi realizzata a conclusione del ciclo di studi del Corso di Laurea Magistrale in Ingegneria civile al Politecnico di Torino. In primis ci terrei ad esprimere un particolare riconoscimento al Politecnico ed all'Universitat Politècnica de Catalunya (UPC), grandi ambienti di ricerca e formazione, dove ho sviluppato il mio studio e dove mi sono sentito particolarmente ben accolto e seguito.

Un primo sentito ringraziamento va al mio relatore, il Prof. Marco Domaneschi, che mi ha saggiamente aiutato e brillantemente seguito durante tutto il lavoro di ricerca sperimentale e di stesura del testo. A lui sono grato per avermi sempre dato la massima disponibilità, motivandomi nei momenti critici e facendomi appassionare al mondo della Ricerca scientifica. Un altro ringraziamento particolare va anche al mio correlatore, il Prof. Joan Ramon Casas per il suggerimento dell'argomento trattato, per avermi trasmesso il fascino dei ponti e tutta la loro complessa tecnica e funzionalità, ma soprattutto per avermi supportato nelle fasi iniziali della tesi.

Desidero ringraziare anche alcuni professori che mi hanno supportato durante il percorso di analisi e stesura del mio elaborato, ovvero il Prof. Antonio Marí, il Prof. Jesús Bairán, la Prof.ssa Marta Serrano e la Prof.ssa Silvia Falletta.

Inoltre, vorrei ringraziare particolarmente la mia famiglia che, con il loro dolce ed in-

stancabile sostegno, sia morale che economico, conferitomi in ogni singolo momento di elaborazione della tesi, ma soprattutto in quelli di maggior criticità, mi ha permesso di arrivare fin qui, contribuendo alla mia formazione personale.

In seguito ringrazio il mio caro miglior amico Giorgio per l'incoraggiamento e la motivazione datami giorno dopo giorno, per i consigli giusti e preziosi necessari per ottenere un ottimo lavoro.

Tutti i miei amici e colleghi hanno avuto un peso determinante nel conseguimento di questo risultato, punto di arrivo e contemporaneamente di partenza della mia vita. Grazie per aver condiviso con me in questi anni le esperienze più importanti.

Infine, un ringraziamento doveroso va a mio nonno Antonino, a cui dedico questa tesi e che rendo orgoglioso per aver raggiunto questo notevole risultato da lui tanto atteso.

Antonino De Gaetano

Bibliography

- [1] C. Doglioni, M. Ligi, D. Scrocca, S. Bigi, G. Bortoluzzi, E. Carminati, M. Cuffaro, F. D’oriano, V. Forleo, F. Muccini, *et al.*, “The tectonic puzzle of the messina area (southern italy): Insights from new seismic reflection data,” *Scientific reports*, vol. 2, p. 970, 2012.
- [2] M. Barbano, R. Azzaro, and D. Grasso, “Earthquake damage scenarios and seismic hazard of messina, north-eastern sicily (italy) as inferred from historical data,” *Journal of earthquake engineering*, vol. 9, no. 06, pp. 805–830, 2005.
- [3] M. Blomfors, K. Zandi, K. Lundgren, and D. Coronelli, “Engineering bond model for corroded reinforcement,” *Engineering Structures*, vol. 156, pp. 394–410, 2018.
- [4] D. V. Val, “Deterioration of strength of rc beams due to corrosion and its influence on beam reliability,” *Journal of Structural Engineering*, vol. 133, no. 9, pp. 1297–1306, 2007.
- [5] A. A. Almusallam, “Effect of degree of corrosion on the properties of reinforcing steel bars,” *Construction and Building Materials*, vol. 15, no. 8, pp. 361–368, 2001.
- [6] Y. Du, L. Clark, and A. Chan, “Residual capacity of corroded reinforcing bars,” *Magazine of Concrete Research*, vol. 57, no. 3, pp. 135–147, 2005.

BIBLIOGRAPHY

- [7] J. Cairns, Y. Du, and D. Law, “Structural performance of corrosion-damaged concrete beams,” *Magazine of Concrete Research*, vol. 60, no. 5, pp. 359–370, 2008.
- [8] D. V. Val and R. E. Melchers, “Reliability of deteriorating rc slab bridges,” *Journal of structural engineering*, vol. 123, no. 12, pp. 1638–1644, 1997.
- [9] D. Coronelli and P. Gambarova, “Structural assessment of corroded reinforced concrete beams: modeling guidelines,” *Journal of structural engineering*, vol. 130, no. 8, pp. 1214–1224, 2004.
- [10] C. K. Chiu, F. J. Tu, and F. P. Hsiao, “Lifetime seismic performance assessment for chloride-corroded reinforced concrete buildings,” *Structure and Infrastructure Engineering*, vol. 11, no. 3, pp. 345–362, 2015.
- [11] T. Takahashi, M. Sakai, H. Seki, and M. Matsushima, “Calculation of lcc and selection system of repairing method for reinforced concrete members exposed to sea environments,” *Concrete Research and Technology (JCI)*, vol. 16, no. 3, pp. 21–29, 2005.
- [12] H. Kim, S. Tae, H. Lee, S. Lee, and T. Noguchi, “Evaluation of mechanical performance of corroded reinforcement considering the surface shape,” *ISIJ international*, vol. 49, no. 9, pp. 1392–1400, 2009.
- [13] M. S. Darmawan and M. G. Stewart, “Spatial time-dependent reliability analysis of corroding pretensioned prestressed concrete bridge girders,” *Structural Safety*, vol. 29, no. 1, pp. 16–31, 2007.
- [14] D. V. Val and M. G. Stewart, “Life-cycle cost analysis of reinforced concrete structures in marine environments,” *Structural safety*, vol. 25, no. 4, pp. 343–362, 2003.

- [15] C. Cao, M. M. Cheung, and B. Y. Chan, “Modelling of interaction between corrosion-induced concrete cover crack and steel corrosion rate,” *Corrosion Science*, vol. 69, pp. 97–109, 2013.
- [16] A. Poursaee and C. M. Hansson, “The influence of longitudinal cracks on the corrosion protection afforded reinforcing steel in high performance concrete,” *Cement and Concrete Research*, vol. 38, no. 8-9, pp. 1098–1105, 2008.
- [17] J. Ghosh and J. E. Padgett, “Aging considerations in the development of time-dependent seismic fragility curves,” *Journal of Structural Engineering*, vol. 136, no. 12, pp. 1497–1511, 2010.
- [18] D.-E. Choe, P. Gardoni, D. Rosowsky, and T. Haukaas, “Probabilistic capacity models and seismic fragility estimates for rc columns subject to corrosion,” *Reliability Engineering & System Safety*, vol. 93, no. 3, pp. 383–393, 2008.
- [19] D.-E. Choe, P. Gardoni, D. Rosowsky, and T. Haukaas, “Seismic fragility estimates for reinforced concrete bridges subject to corrosion,” *Structural Safety*, vol. 31, no. 4, pp. 275–283, 2009.
- [20] P. N. Faye, Y. Ye, and B. Diao, “Bond effects between concrete and steel bar using different diameter bars and different initial crack width,” *Advances in Civil Engineering*, vol. 2017, 2017.
- [21] M. Code, “Fib model code for concrete structures 2010,” *Document Competence Center Siegmund Kästl eK, Germany*, 2010.
- [22] K. Zandi Hanjari, D. Coronelli, and K. Lundgren, “Bond capacity of severely corroded bars with corroded stirrups,” *Magazine of concrete Research*, vol. 63, no. 12, pp. 953–968, 2011.

BIBLIOGRAPHY

- [23] F. Biondini, E. Camnasio, and A. Palermo, “Lifetime seismic performance of concrete bridges exposed to corrosion,” *Structure and Infrastructure Engineering*, vol. 10, no. 7, pp. 880–900, 2014.
- [24] F. Cui, H. Zhang, M. Ghosn, and Y. Xu, “Seismic fragility analysis of deteriorating rc bridge substructures subject to marine chloride-induced corrosion,” *Engineering Structures*, vol. 155, pp. 61–72, 2018.
- [25] K. Tuutti, *Corrosion of steel in concrete*. Cement-och betonginst., 1982.
- [26] P. Thoft-Christensen, “Corrosion and cracking of reinforced concrete,” in *Life-Cycle Performance of Deteriorating Structures: Assessment, Design and Management*, pp. 26–36, 2004.
- [27] DuraCrete, “Statistical quantification of the variables in the limit state functions,” *The European Union-Brite EuRam III-Contract BRPR-CT95-0132-Project BE95-1347/R9*, 2000.
- [28] M. G. Stewart and A. Al-Harthy, “Pitting corrosion and structural reliability of corroding rc structures: Experimental data and probabilistic analysis,” *Reliability engineering & system safety*, vol. 93, no. 3, pp. 373–382, 2008.
- [29] C. I. of Construction Standardization, “Code for durability assessment of concrete structures,” *Beijing (China)*, 2007.
- [30] T. Vidal, A. Castel, and R. Francois, “Corrosion process and structural performance of a 17 year old reinforced concrete beam stored in chloride environment,” *Cement and Concrete Research*, vol. 37, no. 11, pp. 1551–1561, 2007.

- [31] T. Liu and R. Weyers, “Modeling the dynamic corrosion process in chloride contaminated concrete structures,” *Cement and Concrete Research*, vol. 28, no. 3, pp. 365–379, 1998.
- [32] C. Li, “Life-cycle modeling of corrosion-affected concrete structures: propagation,” *Journal of Structural Engineering*, vol. 129, no. 6, pp. 753–761, 2003.
- [33] Y. Yuan, J. Jiang, and T. Peng, “Corrosion process of steel bar in concrete in full lifetime,” *ACI Materials Journal*, vol. 107, no. 6, p. 562, 2010.
- [34] K. A. T. Vu and M. G. Stewart, “Structural reliability of concrete bridges including improved chloride-induced corrosion models,” *Structural safety*, vol. 22, no. 4, pp. 313–333, 2000.
- [35] Y. Pang, X. Wu, G. Shen, and W. Yuan, “Seismic fragility analysis of cable-stayed bridges considering different sources of uncertainties,” *Journal of Bridge Engineering*, vol. 19, no. 4, p. 04013015, 2013.
- [36] M. Barbato, Q. Gu, and J. Conte, “Probabilistic push-over analysis of structural and soil-structure systems,” *Journal of structural engineering*, vol. 136, no. 11, pp. 1330–1341, 2010.
- [37] N. T. per le Costruzioni, “Norme tecniche per le costruzioni,” *Decree of the Minister of the Infrastructures*, vol. 14, 2018.
- [38] CEN, “Eurocode 8: Design of structures for earthquake resistance, part 2: Bridges,” 2005.
- [39] A. Marioni, “The european standard en 1337 on structural bearings,” in *6th World Congress on Joints, Bearings and Seismic Devices Systems for Concrete Structures*, ACI, 2006.

BIBLIOGRAPHY

- [40] A. Poursaeed, “2.8 macrocell and microcell corrosion,” 2016.
- [41] S. E. Hughes, “Chapter 4 - materials and their weldability,” in *A Quick Guide to Welding and Weld Inspection* (S. E. Hughes, ed.), Woodhead Publishing Series in Welding and Other Joining Technologies, pp. 36 – 48, Woodhead Publishing, 2009.
- [42] P. Zhang, M. Lu, and X. Li, “The mechanical behaviour of corroded bar,” *Journal of Industrial Buildings*, vol. 25, no. 257, pp. 41–44, 1995.
- [43] P. ROCHA and K. SILVA, “Construction of the interaction curve of concrete-encased composite columns based on the deformation domains of reinforced concrete sections,” *Revista IBRACON de Estruturas e Materiais*, vol. 8, pp. 447–466, 08 2015.
- [44] M. Tapan and R. S. Aboutaha, “Strength evaluation of deteriorated rc bridge columns,” *Journal of Bridge Engineering*, vol. 13, no. 3, pp. 226–236, 2008.
- [45] J. H. Kim and H. S. Lee, “Reliability assessment of reinforced concrete rectangular columns subjected to biaxial bending using the load contour method,” *Engineering Structures*, vol. 150, pp. 636–645, 2017.
- [46] M. N. Priestley, F. Seible, and G. M. Calvi, *Seismic design and retrofit of bridges*. John Wiley & Sons, 1996.
- [47] T. Wright, R. DesRoches, and J. E. Padgett, “Bridge seismic retrofitting practices in the central and southeastern united states,” *Journal of Bridge Engineering*, vol. 16, no. 1, pp. 82–92, 2010.
- [48] R. L. Mayes, I. G. Buckle, T. E. Kelly, and L. R. Jones, “Aashto seismic isolation design requirements for highway bridges,” *Journal of Structural Engineering*, vol. 118, no. 1, pp. 284–304, 1992.

- [49] J. E. Padgett and R. DesRoches, “Three-dimensional nonlinear seismic performance evaluation of retrofit measures for typical steel girder bridges,” *Engineering Structures*, vol. 30, no. 7, pp. 1869–1878, 2008.
- [50] F. H. A. (FHWA), “Seismic retrofitting manual for highway structures: Part 1?bridges,” 2006.
- [51] M. A. Zanini, F. Faleschini, and C. Pellegrino, “Cost analysis for maintenance and seismic retrofit of existing bridges,” *Structure and Infrastructure Engineering*, vol. 12, no. 11, pp. 1411–1427, 2016.
- [52] C. Pellegrino, A. Pipinato, and C. Modena, “A simplified management procedure for bridge network maintenance,” *Structure and Infrastructure Engineering*, vol. 7, no. 5, pp. 341–351, 2011.

